



Norwegian University of
Science and Technology

Improved Constraint on Salt Geometry in the Southern Nordkapp Basin

Modeling salt geometry using potential field
data integrated with traditional reflection
seismic and well data.

Kristin Heitmann Malin

Petroleum Geoscience and Engineering

Submission date: June 2017

Supervisor: Marco Brönnert, IGP

Norwegian University of Science and Technology
Department of Geoscience and Petroleum

Acknowledgement

First and foremost I would like to thank my supervisor Marco Brønner, Lagleder at NGU and Associate Professor the Norwegian University of Science and Technology, for guidance and comments during this work. For inspiring discussions and helpful inputs.

I would also like to thank Statoil for providing the data, and NGU for making an office and the necessary licenses available for the duration of this work.

Last, I would like to thank my family, for all their support and encouragements.

Kristin Heitmann Malin

Trondheim, 10.06.2017

Abstract

The Nordkapp Basin is a characteristic graben feature in the Western Barents Sea affected by multiple episodes of passive and active diapirism. The salt structures make the Nordkapp Basin an interesting area for studying salt tectonics in the southwestern Barents Sea. Defining the geometry and extent of the salt structures in the Nordkapp Basin from seismic imaging has been challenging. By integrating full tensor gravity data and high resolution aeromagnetic data with reflection seismic and well data, constraint on the salt geometry is increased. A model for the salt geometry of the many salt structures located inside the study area in the southern Nordkapp Basin has been created. An iterative approach to structural inversion was utilized to model three aspects of the salt geometry: diapirs, cap rock and mother salt. An initial model derived from seismic interpretation, filled with densities derived from density well logs and magnetic susceptibilities from core studies was first derived as a framework for the inversion process. Several stratigraphic inversions were applied to derive a model for the geometry and extent of the salt. The iterative approach was utilized to stepwise improve the model and minimize the misfit between the calculated model response and the gravity and magnetic data. The integration of gravity-, magnetic-, seismic- and well data have resulted in increased robustness for the final geological model. The salt model for the study area is presented, and some aspects of the model and implications from the final salt geometry are discussed.

Sammendrag

Nordkapp bassenget er en karakteristisk grabben struktur i det sørvestlige Barentshavet, som har blitt påvirket av flere episoder av aktiv og passiv salttektonikk. Flere saltstrukturer gjør Nordkappbassenget til et egnet område for å studere salttektonikk i det sørvestlige Barentshavet. Tolkning av seismiske data fra Nordkappbassenget har vært utfordrende, spesielt når det kommer til å definere geometri og utstrekning av saltstrukturer i bassenget. Ved å integrere full tensor gravimetrisk data og høy oppløsnings aeromagnetiske data med refleksjonsseismikk og brønndata, oppnås bedre kontroll på volum og utstrekning av saltet. En modell for saltstrukturene innenfor studieområdet i det sørlige Nordkappbassenget har blitt laget. En iterativ tilnærming til strukturell inversjon har blitt brukt for å modellere tre aspekter ved saltets geometri: diapir, takbergart av anhydritt og mor salt. En modell generert fra tolket seismikk og brønndata ble laget som et rammeverk for inverteringsprosessen. Inversjon ble utført på flere flater i modellen gjentatte ganger for å utvikle en modell av geometri og utstrekning for saltet. Den iterative metoden ble brukt for å steg for steg utvikle den geologiske modellen og forbedre modellens tilpasning til dataene i studien. Integrering av gravimetriske, magnetiske, seismiske og brønndata har resultert i forbedret robusthet for den endelige modellen. Salt modellen for studieområdet er presentert og diskutert.

Table of Content

ACKNOWLEDGEMENT	I
ABSTRACT.....	III
SAMMENDRAG.....	V
TABLE OF CONTENT	VII
LIST OF FIGURES	IX
1 INTRODUCTION.....	1
2 BACKGROUND THEORY	5
2.1 SALT.....	5
2.1.1 <i>Salt Tectonics</i>	6
2.1.2 <i>Diapirism</i>	7
2.1.3 <i>Active and Passive Salt Structures</i>	9
2.1.4 <i>Other Salt Features</i>	11
2.2 POTENTIAL FIELD DATA	12
2.2.1 <i>The Magnetic Method</i>	12
2.2.2 <i>The Gravity Method</i>	17
2.2.3 <i>Full Tensor Gradiometry</i>	20
2.3 INTEGRATING GEOPHYSICAL DATA	23
3 GEOLOGICAL SETTING	25
3.1 THE SOUTHWESTERN BARENTS SEA	28
3.1.1 <i>Structural Aspects of the Southwestern Barents Sea</i>	28
3.1.2 <i>Geological History of the Southwestern Barents Sea</i>	29
3.2 GEOLOGICAL SETTING OF THE NORDKAPP BASIN	34
3.3 SALT DEVELOPMENT IN THE SOUTHERN NORDKAPP BASIN	37
4 THE INITIAL MODEL	41
4.1 DATA	43
4.2 WELL CORRELATION.....	44
4.3 SEISMIC INTERPRETATION.....	44
4.4 DEPTH CONVERSION	47
4.5 DENSITY WELL LOG ANALYSES	48
4.6 MAGNETIC SUSCEPTIBILITIES	52
5 INVERSION MODELING APPROACH	53
5.1 SOFTWARE AND ALGORITHM	55
5.2 STRUCTURAL MODEL.....	55

6 MODELING	59
6.1 REMOVING REGIONAL TRENDS.....	61
6.2 SENSITIVITY ANALYSIS.....	66
6.3 MODELING BASEMENT.....	69
6.3.1 Utilizing Tz Data.....	69
6.3.2 Utilizing Magnetic Data.....	71
6.4 ADAPTING MODEL DENSITIES.....	73
6.5 SALT DIAPIR INVERSION.....	74
6.5.1 Utilizing Tzz Data.....	74
6.6 INVERTING FOR CAP ROCK.....	75
6.7 INVERTING FOR MOTHER SALT.....	78
6.8 CORRELATE MAGNETIC DATA WITH DIAPIR.....	78
7 DISCUSSION	81
8 CONCLUSION	93
REFERENCES	95
APPENDIX A: WELL LOGS AND DENSITY GRADIENTS	103
APPENDIX B: DENSITY TRENDS	111
APPENDIX C: CHECK SHOT FROM WELL 7228/7-1	115

List of Figures

Figure 1. Area map showing the study area in the southern Nordkapp Basin.....	3
Figure 2. Classification of salt structures.....	7
Figure 3. Development of salt diapirs.....	9
Figure 4. Illustration of the growth of a diapir during.....	11
Figure 5. Map over the Barents Sea.....	27
Figure 6. Chronostratigraphy with major events for the Nordkapp Basin.	36
Figure 7. Evolution of the salt structures in the Nordkapp Basin	40
Figure 8. Illustration of how the initial model is created.	41
Figure 9. Figure showing the location of wells, study area, and the lateral extent of the diapirs in the study.	42
Figure 10. Map showing the location of the seismic data utilized in the study.....	44
Figure 11. Seismic section. Cross section B	47
Figure 12. Density well log from well 7228/7-1.....	50
Figure 13. Density gradient derived for the Kolmule formation.....	51
Figure 14. Flow diagram illustrating the iterative approach.	54
Figure 15. The observed gravity field.	60
Figure 16. The error grid for the observed field and initial model.	60
Figure 17. Low pass filtered Tz data	63
Figure 18. Observed Tz data, filtered using a 70 km wavelength high-pass filter.	64
Figure 19. Trend removed from observed Tzz data using a trend filter.	64
Figure 20. Trend removed from observed TMI data using a 90 km wavelength high-pass filter.	65
Figure 21. TMI data used for the modeling.....	65
Figure 22. Sensitivity assessment for cap rock, diapir and mother salt for the model response of Tz and Tzz.....	67
Figure 23. Sensitivity assessment for the densities of the model.....	68
Figure 24. Sensitivity assessment for the TMI model response..	68
Figure 25. Selected cut of values for the low pass filtering.....	70
Figure 26. New basement surface	71
Figure 27. Cap rock thickness.....	77
Figure 28. Depth to top of diapirs. From sea surface level.....	80
Figure 29. Difference between interpreted and inverted top diapir surface	80

Figure 30. Magnetic field data used for modeling.....	85
Figure 31. Magnetic field model response.....	85
Figure 32. Gravity field data used for modeling.	86
Figure 33. Gravity field model response.....	86
Figure 34. Vertical gravity gradient data used for modeling.	87
Figure 35. Vertical gravity gradient model response.	87
Figure 36. 3D salt model.	88
Figure 37. The base of the salt diapirs in planar view and trends in their distribution. ..	89
Figure 38. Cross Section A.	90
Figure 39. Cross Section B.	91

1 Introduction

The Barents Sea is an epicontinental sea located approximately 70- to 80° north and cover roughly 1.3 million km² (Doré, 1995). The eastern border is defined by the Russian island Novaya Zemlya and the western border by the edge of the Norwegian-Greenland Sea shelf. It extends from the Norwegian coast and Kola Peninsula in the south, to Svalbard and Franz Josef Land in the north. The Nordkapp Basin is located in the southwestern Barents Sea. The southern sub-basin of the Nordkapp Basin, the southern Nordkapp Basin, is the study area for this paper (see figure 1). It is a fault related intra-continental rift basin containing approximately 30 complex salt structures (Bugge et al., 2002; Gabrielsen et al., 1990; Koyi et al., 1993; Rønnevik and Jacobsen, 1984).

In the southern Nordkapp Basin, the initiation and evolution of the salt structures have been debated (Gabrielsen et al., 1990b; Koyi et al., 1993, 1995; Nilsen et al., 1995). To be able to interpret the evolution of the salt diapirs, the definition of the salt geometry is important. This is an area where seismic imaging suffers due to large acoustic impedance contrast between the salt and surrounding sediments, in addition to difficult seismic imaging in the whole Barents Sea area due to strong free-surface and interbed multiples as a result of several episodes of regional uplift (Bugge et al., 2002; Gabrielsen et al., 1990)). In the southern Nordkapp Basin, in total three exploration wells have been drilled: wells 7227/11-1, 7227/10-1 and 7228/7-1. Well 7228/7-1 resulted in a small discovery, while the other two wells are defined as dry wells (NPD, 2016; Ramberg et al., 2008; Stadtler et al., 2014). Due to difficulties in seismic imaging of the basin the area has been abandoned for petroleum exploration.

The objective of this project has been to study the salt distribution and geometry of a restricted area located in the southern Nordkapp Basin (figure 1), and constrain the solution space of the salt geometry by integrating multiple sources of geophysical data: reflection seismic and potential field data, in addition to information from well logs and core analysis. The data consists of full tensor gravity data and high resolution aeromagnetic data used in combination with 2D and 3D reflection seismic. An iterative approach to structural inversion has been used to derive a geological model supported

by all the involved data to achieve better control on salt geometry. This paper demonstrates the iterative structural inversion approach, presents the resulting model, and discusses some of the implications of the final model in relation to analogue models and different evolution models postulated for the salt in the southern Nordkapp Basin (Koyi et al. 1993, 1995; Nilsen et al. 1995).

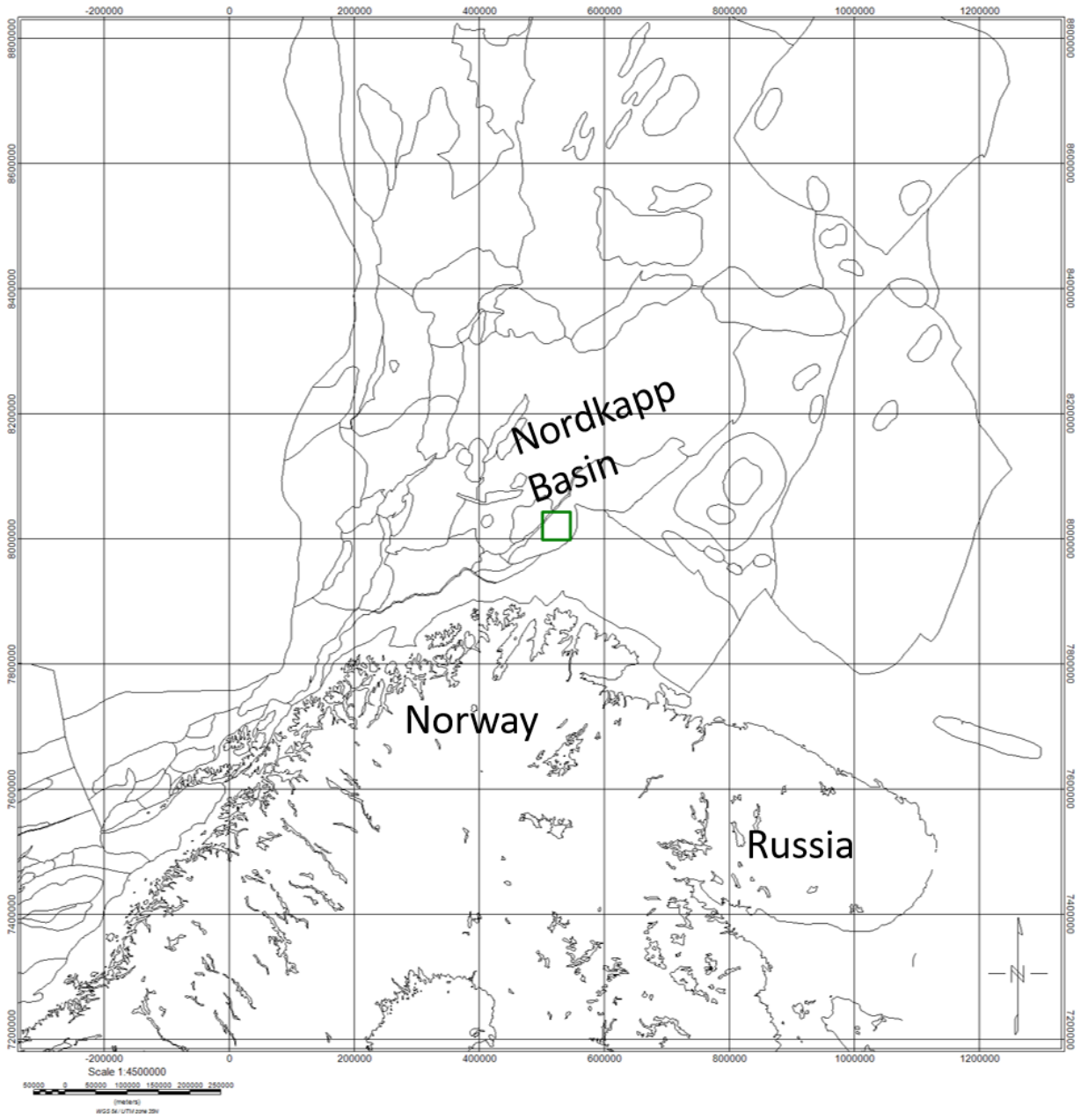


Figure 1. Area map showing a green rectangle indicating the study area in the southern Nordkapp Basin.

2 Background Theory

This section is provided to give necessary background information to better understand the physical and interpretative aspects of the data and modeling procedure utilized in this thesis. Much of the following has been taken from the specialization project by Malin (fall, 2016) and has been modified where appropriate.

2.1 Salt

Halite, known as rock salt, is the most common component in evaporitic rock as it is easily precipitated during evaporation of brine. For this paper, salt is used in a broader sense, not just referring to halite but as defined by Hudec and Jackson (2007), the term “salt” is expanded to cover all rock bodies composed primarily of halite (NaCl). Salt is of significant economic importance in hydrocarbon exploration, due to the large number of reservoirs found in relation to salt structures. The presence, development and origin of salt structures all influence the hydrocarbon potential of an area. Salt formations are important both direct, when salt act as a barrier forming the cap and seal of a reservoir, but also indirect, because the presence and movement of salt affect hydrocarbon migration (Stewart and Clark, 1999).

Pure halite has a density of 2.16 g/cm^3 , while sediments during early sedimentation have a density of around 2.0 g/cm^3 or lower. While other sediments increase in density during burial in response to compaction and diagenesis, evaporites containing large parts of halite compact little and will maintain almost their original density. The density of other sediments will increase to pass that of the salt, and eventually lead to a significant density contrast (Hamdi-Nasr et al., 2009).

Salt has a significantly lower shear strength compared to sedimentary rocks. Under pressure of the overlaying compacted sedimentary rocks, the salt can act as a viscous fluid and flow in response to pressure differences. Salt movement and migration will result in deformation of the surrounding rocks, including faulting and folding. (Rowan et al., 2003).

The presence of salt influences sedimentation, trap potential and thermal evolution of a basin (Alsop et al., 2012). The salt can move to create upwards bulging of the sea floor or even piercing the seafloor, creating rim synclines, synclines on the sides of the bulging salt, which will influence the depositional pattern in the basin. Salt is impermeable, and can form both top and side seals. In addition, salt has high thermal conductivity, which influences the temperature distribution (Alsop et al., 2012). These effects show how salt provinces involve particularly complex geology and subsequent complicates geological and geophysical interpretation in these areas.

2.1.1 Salt Tectonics

Salt tectonics describes the processes that occur when significant volumes of evaporitic rocks are mobilized and intruded into other sedimentary rocks. Salt tectonics includes all structures, effects and processes associated with mobilized salt bodies.

Salt flows in response to pressure differences from a high-pressure zone to a lower pressure zone. This usually means moving upwards in the stratigraphic sequence. Pressure differences in the subsurface result from differential loading (Alsop et al., 2012). Differential loading can form from non-homogenous sedimentation or compaction and diagenesis, but also in response to displacement loading during regional extension or to contraction as a boundary of one rock body is displaced relative to another (Hudec and Jackson, 2007). The last form, thermal differential loading is differential loading due to convection within the salt. But this has not been proven for any salt structures (Hudec and Jackson, 2007).

Before salt can flow upwards in a sedimentary sequence, it needs to pierce through the overburden. Consequentially the strength of the overburden is a significant restricting factor to the formation of domes and other salt structures (Vendeville, 2002). In addition to the overburden, friction along the boundaries of the salt may be an important restricting factor for the salt flow, predominantly for thin salt layers (Hudec and Jackson, 2007). Fracturing and faulting will weaken the mechanical strength of the overburden and favor

upwards flow of the salt (Vendeville and Jackson, 1992). There are two main mechanics to initiate salt flow, as defined by Mohriak et al. (1995):

Adiastropic processes; Basement detached or gravity induced processes that are caused by buoyancy effects resulting from basement inclination and differential loading. The result is thin skinned tectonics that can initiate salt movement.

Diastrophic processes; Basement involved or thick-skinned tectonic processes caused by faults affecting the basement, salt and overburden. The result is that salt starts flowing and initiate a mobilization of the overburden.

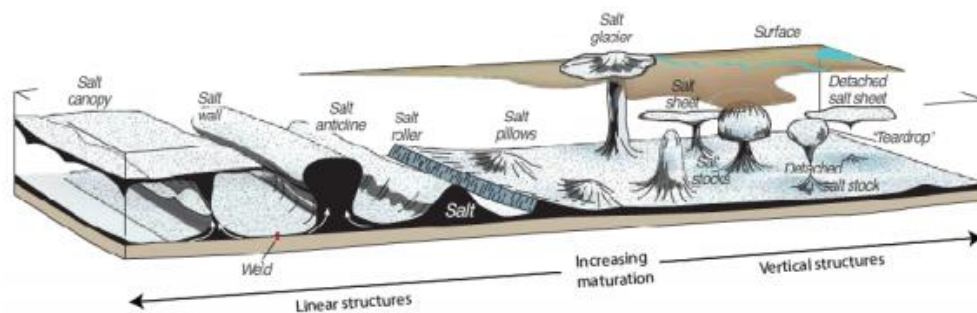


Figure 2. Classification of salt structures. Figure modified from Fossen (2010).

2.1.2 Diapirism

Diapirism is the development of salt diapirs (Vendeville and Jackson, 1992; Hudec and Jackson, 2007). Salt diapirs are an expression of mobilized and upward flowing salt and are the most common near surface feature of salt tectonics (Fossen, 2010). A salt diapir can be characterized as any salt body structurally discordant (Jackson, 1995). Figure 2 illustrates some different salt structures as characterized by Fossen (2010).

Understanding salt diapirs has been a challenge for geologists and geophysicists since the 1800s (Jackson, 1995). The historical development of salt interpretation can be roughly divided into three periods: The pioneering era, the fluid era and the brittle era (Jackson, 1995). The pioneering era covers the period from the beginning of discoveries and descriptions of domes, glaciers and various other salt bodies and the often erroneous interpretations of their origin and evolution. During the fluid era, the main understanding

evolved that salt because of its low density and shear strength act as a fluid in the subsurface. As of this, salt would flow and salt structures develop in response to buoyancy forces. The interpretation was that salt domes would result from a type of Rayleigh-Taylor instability at the interface between salt layers and other sedimentary rocks and form in response to the density contrast between salt and the surrounding strata. The brittle era arises from the discovery that salt is not able to flow simply from buoyancy forces alone. The concept of the brittle overburden holding that salt in place becomes dominant. The problem with the fluid interpretation model is that it assumes that both the salt and the overburden act as fluids as is the case for Rayleigh-Taylor instability, when the strength of the overburden is actually significant. The strength of the overburden rock is too large for salt to start flowing without any other influence. Weakening of the overburden through thinning and fracturing is therefore a crucial point for the development of salt diapirs and other salt migration (Vendeville and Nielsen, 1995).

Shape and size of salt structures are largely variant, and are affected by regional dip, rate of progradation and sedimentation, primary salt thickness and properties of the overburden. (Jenyon, 1986).

A model for the development of diapirs was suggested by Trusheim (1960). The model consisted of three stages; the pillow stage, the diapir stage and post diapir stage. This model relies only on buoyancy forces as the driving force; hence it requires no change in the length of a section in cross section. This model was later modified by Vendeville (2002) to accommodate the effects of the brittle overburden and making it more in line with the current interpretation of salt tectonics (fig. 3). The model for development of salt diapirs can be applied for many salt provinces. However, the three-step model was challenged due to several diapirs where no evidence of a pillow stage can be found (Nielsen et al., 1995).

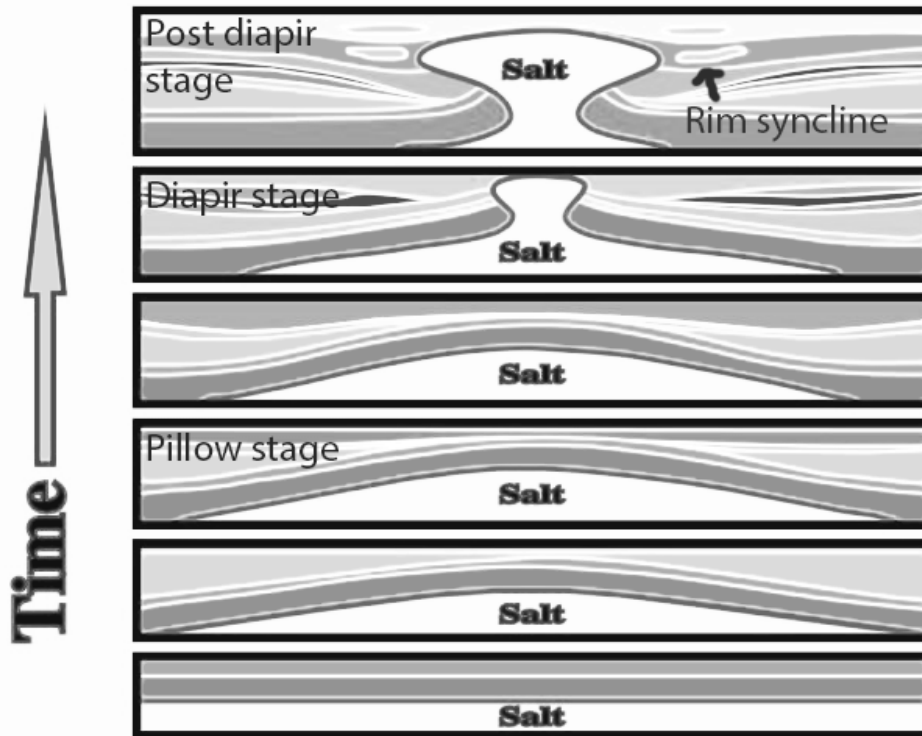


Figure 3. Development of salt diapirs as postulated by Trusheim (1960).

2.1.3 Active and Passive Salt Structures

Active salt structures occur where a salt body is provoked by applied stress to the salt body to actively pierce the overburden. Both, thrust tectonics and extensional tectonics can result in diapirism from horizontally deposited evaporitic layers (fig. 4). Active tectonics reduces the strength- and gives thinning of the overburden. It is therefore an important factor often associated with the initiation of salt diapirs (Hudec and Jackson, 2007).

Passive growth of salt structures can be defined as syn-depositional growth of a salt body near the surface (Jackson, 1995). The weak salt layer will deform in response to stress to the salt body, and move upwards while new sediments are deposited (Hudec and Jackson, 2007; Nilsen et al., 1995). The diapir growth might be driven by surrounding sediments sinking into the source layer or the salt might be inflated by surrounding stress from tectonic activity, local or regional, differential loading or gravity gliding (Nielsen et

al., 1995). If there is sufficient horizontal shortening, the salt will continue to move upwards after depletion of the mother salt. The salt diapir will then be thinning in the horizontal direction to compensate the vertical growth. The passive growth of diapirs continues until the initial salt layer, mother salt, is depleted, the feeder is cut off or tectonic activity ceases.

If the salt is not growing upwards the diapir will be buried and become inactive (Hudec and Jackson, 2007). When studying salt structures, evidence can be found of several periods of burial, active- and passive diapirism. The evolution of the salt dome is periodic and the different periods are indicated by the wedge shape of surrounding strata in relation to the structure and imaged in the geometry of the salt itself (Koyi et al, 1998; Nilsen et al., 1995; Rowan et al., 2003; Vendeville, 2002).

The shape of a diapir is dependent on external stress, sediment deposition rate and growth rate of the salt itself. Depending on the amount of sediment deposition in relation to the rate of growth of the salt structure the salt will grow vertically in a stock or flow sub-horizontally creating overhangs (Koyi et al., 1993). These overhangs are of particular interest as they can form large hydrocarbon traps, as observed in the Gulf of Mexico and offshore Brazil (Chowdhury, 2010; Mohriak, 1995).

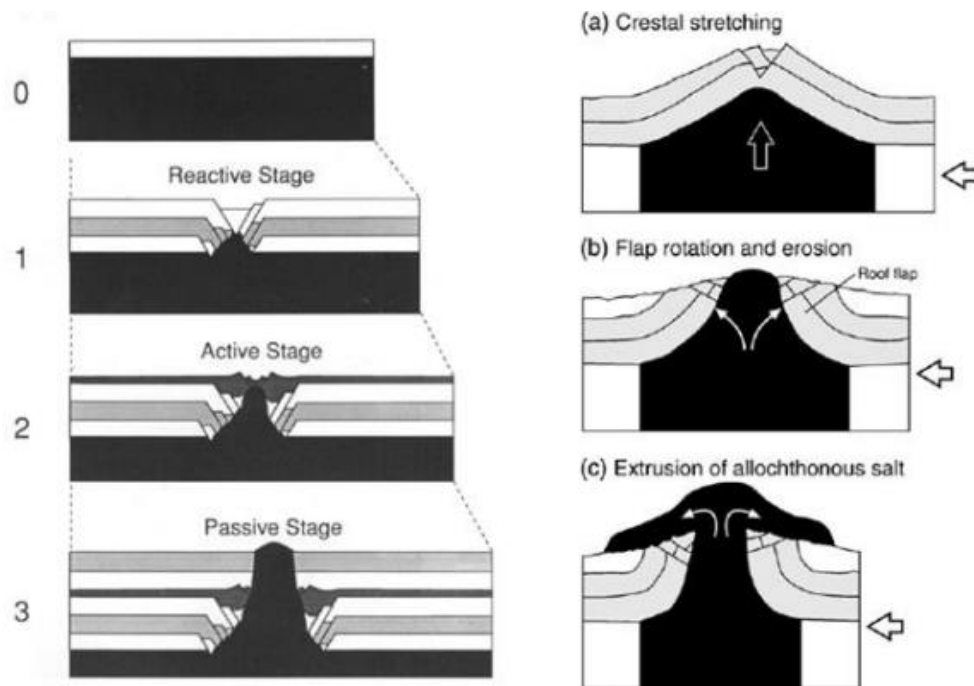


Figure 4. On the left: Illustration of the growth of a diapir during thin-skinned extension. The figure shows the initial (0), reactive (1), active (2) and passive stage (3). On the right: growth of an existing diapir during shortening. The roof is faulted and thinned (a), the diapir rise actively and the salt pierce the overburden (b) and the salt extrudes on the surface forming a salt glacier (c). Figure from Hudec and Jackson (2007)

2.1.4 Other Salt Features

When the salt can no longer evolve as a passive diapir, the salt can still migrate to low-pressure areas developing in folds and faults or forming allochthonous salt. Buckling of the overburden can result in anticlines which can be filled by salt cores. Migration of salt away from the original salt layer form allochthonous salt, meaning the salt body is cut off from the mother salt and now acts as an allochthonous body (Hudec and Jackson, 2006).

Salt welds arise where depletion of the salt layer makes it so thin, that the over and underlying strata weld together. Welds might be horizontal, sub-horizontal or vertical. Vertical welds occur when the stem of a diapir is cut off. Salt welds are of considerable importance when considering hydrocarbon migration (Stewart and Clark, 1999).

2.2 Potential Field Data

Potential fields include gravity and magnetic fields in addition to electromagnetic fields. Geophysical methods utilizing the Earth's potential fields are referred to as potential field methods. As described by Hinze et al. (2013): gravity and magnetic methods are referred to as potential field methods because the measurements involve a function of the potential of the observed force, either terrestrial gravity or magnetic field, at the observation site. Because the data can be readily acquired from, ships, aircraft and satellites, large amount of potential field data exists covering the entire surface of the Earth. Although much of this data lacks in spatial and positioning resolution, large amounts of data of varying quality is publicly accessible at minimal cost (Hinze et al., 2013).

Gravity and magnetic methods are passive methods, meaning they measure variations in the Earth's naturally occurring fields. The gravity and magnetic methods are also invasive, making the methods suited for delicate areas. The theory behind the methods is relatively simple, and they are some of the oldest geophysical methods (Nabighian, 2005a, 2005b). The gravity and the magnetic data are represented in anomalies, which is the observed field at each observation point reduced by a predicted field based on a known model (Hinze et al., 2013).

2.2.1 The Magnetic Method

The magnetic method can be applied to a wide variety of subsurface exploration problems involving horizontal variations in magnetic properties from near the base of the Earth's crust to within the uppermost meter of soil. These variations cause anomalies in the Earth's normal magnetic field, which can be mapped using special instruments, called magnetometers.

The Earth magnetic field

As described by Campbell (2003), the geomagnetic field, or the total magnetic field experienced on the surface of the Earth is a combination of several magnetic components within and outside the Earth, and vary both spatially and temporally. The main field is the Earth's internal magnetic field generated by a dynamo effect from electromagnetic currents in the outer core. This field accounts for about 98% of the geomagnetic field.

Most of the residual field is contributed to interaction of solar plasma with the core field. The last small remaining component of the field is due to static effects from heterogeneities in magnetization of subsurface materials. It is this effect that is of interest in magnetic exploration studies (Hinze et al., 2013).

The magnetic force between two poles is proportional to the strength of the poles. Magnetic field strength is also inversely proportional to the square of the distance between the poles. Because magnetic fields are dipolar, the force between two poles might be both attractive and repulsive, as opposite pole attract while same poles repel. The strength of the force between two poles can be expressed by Coulomb's law, given by

$$F = \mu_0 \frac{q_1 \times q_2}{4\pi r^2} \quad (1)$$

Where μ_0 is the magnetic constant and $\mu_0 = 4\pi \times 10^{-7} \text{ N/A}^2$.

The unit for magnetic fields is tesla, T. The unit nano tesla, nT is commonly used.

Crustal rocks have a potential to be magnetized. Magnetic polarization of Earth materials is the result of the magnetic susceptibility and the remnant magnetization. Remnant magnetization is the leftover magnetization obtained by the material when solidified below Curie temperature, and magnetic susceptibility is a materials ability to be influenced by an external magnetic field (Nabighian et al., 2005b). The Earth's geomagnetic field induces a magnetization on all earth materials, and the strength of the resulting field is dependent on the mineralogy of the material.

The Earth's magnetic field is approximately aligned with the rotational axis of the Earth, and changes in long term secular variations as a result of changes in electrically charged currents in the outer core (Hinze et al., 2013). These long term variations have resulted in "wandering", or shifting position of the magnetic poles, as well as inversions of the geomagnetic field. Inversions of the geomagnetic field can be traced at the mid-oceanic ridges, by observing the changing orientation of remnant magnetization (Courillot and Besse, 1987).

Magnetic fields can be described as dipolar, meaning they have a positive and a negative pole. For the Earth's main magnetic field this is referred to as a north- and South Pole. The Earth's geomagnetic South Pole is located close to the geographical North Pole. It is important to separate between the North magnetic pole, the point on the northern hemisphere where magnetic field points straight down, the North geomagnetic pole, the point where the axis of the southern end of an imagined best-fit dipole aligned with the Earth's magnetic field crosses the surface of the earth, and the geographical North pole (Hinze et al., 2013; WDC of Geomagnetism, 2016). The North magnetic pole, the North geomagnetic pole and the geographic North Pole is related as illustrated in figure 4.

Magnetic measurements at an observation point will detect the total magnetization of the materials in the subsurface. Due to the dipolarity of the geomagnetic field, a body of the same size, composition, and depth will have different signatures at different magnetic latitudes as the magnetic inclination, the angle at which the magnetic force field is oriented with the Earth's surface, changes with latitude (Nettleton, 1971).

The magnetic method for geophysical prospecting

The magnetic method is the oldest, and one of the most widely used methods for geophysical surveying. Magnetic fields were first exploited for geophysical prospecting in the seventeenth century, where compasses were utilized to locate iron ore deposits. The method has later become an efficient tool for regional studies with the development of aeromagnetic surveys (Nabighian et al., 2005b). The magnetic method measures the Earth's magnetic field and map lateral variations in the field. Anomalies in the field are measured and linked to subsurface properties. One major benefit of magnetic data is that the magnetization of a rock is only dependent of its mineral content, and independent of depth until metamorphosis occurs; an ability that can help overcome the problem of the nil zone experienced with gravity data (Stadtler et al., 2014). The magnetic data is also shown to be sensitive to basement variations, which can help to overcome the problem of separating between source signatures of the basement and basin for gravity modeling (Libak et al., 2012).

Measurements

Magnetic methods utilize measurements of the magnetic field to distinguish areas of anomalous magnetization in the subsurface. Examples include volcanic intrusions and extrusions, which exhibit a very strong magnetic field, or hydrocarbons or salt deposits showing a weakened magnetic field compared to surrounding geology (Olesen et al., 2010). Magnetometers are used to measure the magnetic field with high precision. Magnetic measurements for exploration are acquired on the ground, in the air, in space, in water and down boreholes. The measurements are widely applicable and can cover a large range of scales (Nabighian et al., 2005b). All of the measurements, except those taken in boreholes measure lateral variations in the magnetic field resulting from variations in the magnetization of the crust. Borehole measurements measure vertical variations.

The most common magnetometers are the Fluxgate-, Proton precession-, Alkali vapor- and superconducting quantum interference device, or SQUID magnetometer. The Fluxgate magnetometer is small in size, rough in design, tolerates high temperature and can be operated at relatively high measurement rates (Nabighian et al., 2005b). However, it must be oriented when used because it is a component instrument. The Proton precession magnetometer is rugged, simple, has essentially no intrinsic heading error and does not require to be mounted on an oriented platform. It does require large quantity of sensor liquid and a large coil to produce reasonable signal strength (Nabighian et al., 2005b). This means it can be heavy, bulky and require much power. Sample rate is also limited if reasonable sensitivity is required. The Alkali vapor magnetometer is the most popular. This is because of its excellent sensitivity ($<0.01\text{nT}$) and high sample rates (Nabighian et al., 2005b). It is lightweight and compact; however, it can be fragile and has an intrinsic heading error. The SQUID magnetometer has very high sensitivity (Nabighian et al., 2005b). However, its popularity is not too great because it requires cryogenic supplies, which reduces its mobility.

Reductions and corrections

The geomagnetic field is highly influenced by secular variations originated from fluid currents in the outer core, in addition to spatial variations resulting from solar winds (Nettleton, 1962). As described by Hinze et al. (2013) the measured magnetic component

is the vertical sum of all sources of magnetization. Therefore, the measured field is compared to a model field based on known planetary and geological effects. This is to obtain a field representing the desired subsurface anomalies only. To isolate the anomalies from geological heterogeneities in the crust three main processes are implemented: eliminate temporal variations from ionospheric electric currents, reduction to a datum to remove the effect of the planetary geomagnetic field and to correct for temporal and spatial effects in the external magnetic field (Nabighian et al., 2005b).

The international geomagnetic reference field, IGRF, is as described by Macmillan and Maus (2005) a standard mathematical description of the Earth's magnetic field used widely in studies of the Earth's deep interior, its crust, ionosphere and magnetosphere. Subtracting the IGRF reduces the observed data to anomalies related to the crustal field magnetization by removing the predicted geomagnetic field deriving from the outer core. The IGRF include the effect from flattening of the Earths shape and elevation above sea level as well as it extrapolates the secular variations in the core field. The IGRF is revised regularly to keep up with the temporal changes of the geomagnetic main field. The IGRF constitutes a definitive core field model, a core field model, and a linear annual predictive secular variation model (Thébolt et al., 2015). The definite core field is referred to as the definitive geomagnetic reference field, DGRF. It is called definite because any further improvement to the determined model is not likely. The second model, referred to as an IGRF-model, is non-definitive and is replaced regularly by a revision of the IGRF. The final component is referred to as the secular variation, and is included to predict the time variation of the large-scale geomagnetic field for the future until the next IGRF is presented (every 5 years). (Thébolt et al., 2015).

Comparing the obtained data to measurements from a local base station can help suppress or correct uncorrelated spatial and temporal effects of the external field, like micro pulsations and magnetic storms (Hinze et al., 2013). Diurnal variations due to external disturbances will also be observed by a base station and can be corrected accordingly. This operation is performed if there is a base station close to the survey, and the survey area is relatively small. If there is no base station close by, the correction is only applied if a clear correlation is observed between the collected data and data measurements taken at the base station.

Due to the nature of magnetic data more focus is put on depth determination and structural analysis in magnetic data interpretation compared to gravity data (Hinze et al., 2013). Both forward and inverse modeling schemes are applied, but the incorporation of other subsurface constraint, geological- or geophysical data are essential for an efficient interpretation and robust final model (Nabighian et al., 2005b).

2.2.2 The Gravity Method

The gravity method is based on measuring changes in the terrestrial gravity field. The Earth's gravity field is a monopole field directed towards the center of the Earth. The field is dependent on the size, mass and movement of the planet (Hinze et al., 2013).

The Earth gravity field

The gravitational field experienced on the surface of the Earth is caused by gravitation, the phenomena where two bodies of mass exhibit an attractive force towards each other. This attraction is given by Newton's law as

$$F = G \frac{m_1 * m_2}{r^2} \quad (2)$$

Where G is the gravitational constant and $G = 6.67408(31) \times 10^{-11} \text{ m}^3 \cdot \text{kg}^{-1} \cdot \text{s}^{-2}$.

The gravitational force is proportional to the masses of the two bodies and inversely proportional to the square of the distance between the bodies. The unit for gravity is the gal. 1 gal is equal to 100 m/s^2 . For the case of gravitational studies, the unit milliGal, mGal is commonly used.

A perfect sphere of uniform density or with a density only varying radially from the center, would produce a uniform gravitational field directed straight towards the center of the sphere. However, the Earth is not a perfect sphere, it is slightly flattened at the poles while it is bulging at the equator, and the density is not uniform. Thus, there are slight deviations in both the magnitude and direction of gravity across the Earth's surface (Garland, 2016). The measured net gravity force at a point is called "effective gravity" or "observed gravity".

Effective gravity includes all factors that affect the net force. These factors vary and include the centrifugal force and the gravitational pull of the Moon and Sun, so called tidal effects, in addition to the elevation determining the strength of the gravitational pull. Effective gravity on the Earth's surface varies by around 0.5%, from sea level at the poles, to the highest mountains close to the Equator (Hinze et al., 2013).

The Gravity Method for Geophysical Prospecting

Geophysical exploration using the gravity method is based on measuring small lateral variations in the terrestrial gravitational field. The principle is to measure, process, analyze and interpret perturbations in the measured gravity force to distinguish geological structures of anomalous density in the subsurface. Typical geological features with high density contrasts are salt bodies, magmatic intrusions or the distribution of basement highs and sedimentary basins (Nabighian, 2005a). The gravity method is particularly useful in the mapping of salt structures, due to the generally large density contrast between salt and surrounding sedimentary rocks (Olesen et al., 2010). Limitations of gravity data used in salt provinces are related to the "nil zone" described by Bain et al. (1993). Within the nil zone salt and surrounding sedimentary rocks have the same density. Salt above and below the nil zone will result in opposite anomalies, positive and negative, and can hence act destructively. Another challenge is internal density changes in the salt caused by different mineral composition, which can cause problems in data interpretation (Colombo et al., 2014). For instance, anhydrite has a significantly higher density compared to halite, and the distribution of anhydrite/halite will affect the observed anomaly data. A third limitation of gravity data in salt provinces is the inability to distinguish between different deep structure anomalies, such as salt or basement uplift (Stadtler et al., 2014).

Measurements

From Newton's law of gravitational attraction, the measured gravitational force at an observation point is directly linked to the mass below this point. The gravitational method uses this relation to make interpretations about the subsurface geology from the measured gravitational field (Hinze et al., 2013). The gravity field at an observation point is measured using gravimeters. These measurements can be absolute or relative. Gravity surveys can be conducted on land by foot or in a vehicle, in the air by plane or helicopter,

by satellites in orbit, underwater or down boreholes (Nabighian, 2005a). Gravimeters only measure the vertical component of the gravity field. Gravity gradiometers measure all vector components of the gravity field, and provide the full tensor of the gravity field. This allows information from up to 5 independent components, compared to standard gravity surveys where only the vertical component is measured (Murphy, 2012).

Reductions and corrections

The observed gravitational field at each acquisition point is the sum of all gravitational forces acting in that point. Consequently, it is necessary to isolate the signal caused by the geological target, from other factors influencing the total field (Hamdi-Nasr et al., 2009). The fundamental is to obtain the gravity anomaly, which is as defined by Hinze et al. (2013) “the difference between the observed and the theoretical or predicted vertical acceleration of gravity” (p. 143).

A conceptual model of gravity where one assumes the Earth is laterally homogenous in density, and include all known unwanted effects is removed from the data. This process is often referred to as *correction* or in older books and publications also *reduction* (Hinze et al., 2013).

As described by Hinze et al. (2013) gravity surveys are influenced by a wide variety of effects: latitude variations, height effect (free-air effect), masse effect (Bouguer effect), terrain effects, geological- and isostatic effects, curvature of the Earth and the Eötvös effect (Hinze et al., 2013). For moving platform surveys, changing centripetal force and Coriolis acceleration must also be corrected (Nabighian et al., 2005a).

What effects to remove from the data is dependent on the objective of the study. Common gravity anomaly data include free-air anomaly maps, data corrected for the elevation at which the data was acquired, or Bouguer anomaly maps, where the mass between the reference level and the measurements has been accounted for. Free-air anomaly maps are commonly used for marine surveys where the effect of the bathymetry is negligible as the water density is well known, while Bouguer anomaly maps are most frequently used

for continental and near-shore marine surveys as it enhances density contrast compared to Free-air anomalies which will represent mainly the topography (Hinze et al. 2013).

When the signal of the geological target is isolated from the cumulative effect of all sources acting at the observation point, the resulting anomaly is a function of the mass, sizes, shape and depth of the source. However, it is not possible to isolate the effect of only one source, and the interpretation of gravimetric data is not unique and subject to ambiguity (Dell'Aversana, 2014). The final anomaly map has to be interpreted based on a-priori information regarding the source, or by approximation techniques and inversion (Hinze et al., 2013).

2.2.3 Full Tensor Gradiometry

Full tensor gradiometry, FTG gravity is a high precision moving platform gravity gradiometry that measures the full gravity field in all directions. It is a powerful geophysical technique that in many areas provides superior measurement of the Earth's gravitational field compared to conventional gravity. FTG gravity measures the derivatives of all three components in all three directions of the gravitational field. Hence, the variations of the two horizontal and the vertical component of the gravity field is measured in all three directions. The result is that FTG gravity has two major advantages over conventional scalar gravimetry; increased sensitivity to the distance of a mass anomaly and increased S/N-ratio as much of the effects from the moving platform during acquisition is suppressed (O'Brien et. al, 2015). Thus, gravity gradiometry offers significant increased resolution and accuracy over conventional gravimetry. However, FTG gravimeters are much more expensive than regular gravimeters, and so the acquisition of FTG data is more costly compared to a regular gravity survey.

Both increased resolution and accuracy are an inherent result of the physical nature of the gradient data compared to the standalone one dimensional scalar data provided by conventional gravimetry.

Physics

The gravitational field can be described in full by

$$\Phi(r) = \iiint \frac{G\rho(r')}{|r-r'|} d^3r' \quad (3)$$

Where $\Phi(r)$ is the potential function and r is the measurement position and $\rho(r')$ is the density at position r' . The vertical component of the gravity field is given by

$$g_z = -\frac{\delta\Phi(r)}{\delta z} \quad (4)$$

This would give the horizontal derivative in the y-direction to be

$$G_{zy} = -\frac{\delta}{\delta y} \frac{\delta\Phi(r)}{\delta z} \quad (5)$$

Here G_{zy} is one of the nine tensor components.

Because $G_{yx}=G_{xy}$ and $G_{zy}=G_{yz}$ and $G_{zx}=G_{xz}$ and the tensor is symmetric about its diagonal and its trace, the sum of the diagonal components is zero in source free regions per Laplace's equation. Hence, there are only five independent components to the full tensor.

The most common measurements used in interpreting FTG gravity data are:

$$\begin{array}{ccc} G_{xx} & G_{xy} & G_{xz} \\ & G_{zz} & G_{yz} \\ & & G_{zz} \end{array}$$

All of these components contain valuable information about the underlying geology and each enlightens different aspects of this geology (O'Brien et al., 2005).

Measurement and acquisition

FTG gravity is a technology deployed on both marine and airborne platforms and is applied worldwide for both hydrocarbon and mineral exploration prospecting. The concept of the instrument is described by Murphy (2010), and Murphy and Brewster (2007)

present a more detailed discussion on extracting geological information from FTG data. The nature of tensor data is used to identify sub-surface complexity in terms of shape, size and orientation of anomalous density bodies.

As described by Murphy and Dickinson (2010), FTG gravity is a multi-accelerometer gravity measuring instrument which measures changes in the gravity field in five independent directions. The directions in which the changes in gravity are measured correlates to components of the gravity tensor field as described above. Measuring five of the in total nine tensor components offers information regarding orientation, size and shape of target structures. Amplitude of wavelengths and anomalies help identifying thickness, density and depth of the geological target (Murphy and Brewster, 2007).

FTG gravity is presented in the standard unit Eotvos, E. Data have been shown to achieve G_{zz} detectability threshold of 2 to 3 E over 200-300 meters (Murphy et. al, 2007).

The combination of the tensor data allows a detailed assessment of sub-surface geology. The vertical tensor component G_{zz} , help map the density relation of a body mass to its geological setting and source depth. The horizontal tensor components, G_{xx} , G_{yy} , G_{xy} , G_{xz} , and G_{yz} , are used to identify and map geological contacts like lithological contacts or edge of an anomalous density body. The strength of tensor data lies in combining the information obtained from different tensor component into one model of the subsurface geology.

2.3 Integrating Geophysical Data

Modern exploration involves utilization of geological and geophysical techniques to identify and define a pre-conceived geological model which locates targeted resources. The models are then refined by adding insightful information and used to establish the perceptivity of a region (Murphy and Dickinson, 2010). Integrated geophysical models are models designed from multiple geophysical data and which is consistent with all data included in the study. The result is a more robust final model and considerable risk reduction of an exploration target.

The foundation for integrated geophysical models comes from rock physics; all geophysical data represents the same subsurface. Thus, integrating multiple dataset into the same model will give an improved and more reliable insight in the physical parameters of the subsurface target. An integrated geophysical model aims to maximize the benefits of all data included in the model, while minimizing the liabilities of each dataset (Dell'Aversana, 2014).

Different geophysical data have different métiers and liabilities. This thesis will focus on the use of FTG gravity integrated with magnetic data, 2D and 3D reflection seismic and well-log data to create a model over several large salt structures. Reflection seismic works well in defining structural setting of an exploration target. Gravity and magnetic methods are efficient in defining anomalies in density and magnetic susceptibility and can contribute with additional information where seismic data lack illumination (Stadtler et al., 2014).

Common reflection seismic is mainly intended for use in stratified rock, and is ideal for depth characterization and to outline area stratigraphy. However, the data has limited applicability in the areas of thrust belts, subsalt or sub basalt imaging (Colombo et al., 2014). Particularly sub-salt areas are challenging when it comes to producing seismic images of sufficient quality. Salt causes strong acoustic impedance affects, and result in problems with defining salt flanks and subsalt reflectors.

Magnetic data commonly have good sensitivity to depth-to-basement and shallow targets. Gravity data provides information on lateral density contrasts, and show good sensitivity to sedimentary basins and salt distribution. The database provided by magnetic and gravimetric data makes it possible to get constraints on both shallow and deeper structures, previously not well defined from reflection seismic alone (Stadtler et al., 2014).

In a sedimentary basin like the Nordkapp Basin, magnetic data can give good reconstruction of the depth to basement and shallower targets, while gravity data can provide information on salt distribution. The integration of magnetic and gravity data with well-log data and reflection seismic will produce a final model more extensive and robust compared to a model created from any single dataset (Stadtler et al., 2014). In this thesis, structural inversion using FTG gravity and high resolution aeromagnetic data were applied to an initial stratigraphic interpretation from reflection seismic and well-log data. Seismic signal is blurred in a sub-salt setting and the integration with gravity and magnetic data contribute to an improved and better constrained model on the extent and geometry of the many salt structures located inside the study area (southern Nordkapp Basin, see figure 1).

3 Geological Setting

The Barents Sea is a large area of continental shelf located between the eastern border of the Norwegian-Greenland Sea, the North Norwegian and Russian coasts, and the Novaya Zemlya, Franz Josef Land and Svalbard (Gabrielsen et al., 1990). The geology of the Barents Sea is complex, and the result of multiple tectonic phases, shifting climate and changing depositional conditions (Smelror et al., 2009; Worsley et al., 2008). Three tectonic phases have been identified as the most important in the development of the Barents Sea geological framework: the Timanian-, Caledonian- and Uralian Orogeny, in addition to proto-Atlantic rifting in the west and the break-up and opening of the North Atlantic (Gernigon et al., 2014; Smelror et al., 2009). The Timanian orogen developed as a fold and thrust belt along the southeastern Barents Sea (Gee, 2006; Smelror et al., 2009). The Caledonian Orogeny is characterized by the generation of the Laurasian continent, and the closing of the Iapetus Ocean (Gee, 2006). The Uralian orogen, a collision between the Laurasian continent and western Siberia formed the present eastern margin of the Barents Sea. Following the Uralian orogen, the supercontinent Pangaea was established (Dore, 1995; Gee, 2006). Basin highs and platform areas formed in late Paleozoic and Mesozoic in response to continental break-up and the opening of the Norwegian-Greenland Sea (Gabrielsen et al., 1990a; Smelror et al., 2009).

The present day geological structures are shown in figure 5. The figure also shows gravity and magnetic anomaly maps covering the area, and illustrates how the structural features are visible also on the anomaly maps.

The Barents Sea consists of two main geological provinces; the western- and eastern region. The border between the two regions is represented by a huge monocline structure (Smelror et al., 2009). The eastern region includes two large basins; the North- and South Barents Basin. The area geology is closely linked to the geology of the Uralides platform, Timian-Pechora and Novaya Zemlya areas (Doré, 1995). The western province constitutes an interaction of several basins, structural highs and platforms originating from a complex tectonic history (Faleide et al., 1984; Ramberg et al., 2008; Worsley, 2008).

The Nordkapp Basin is located in the eastern region of the southwestern Barents Sea, an area which has been stable since Late Paleozoic time (Gabrielsen et al., 1990a).

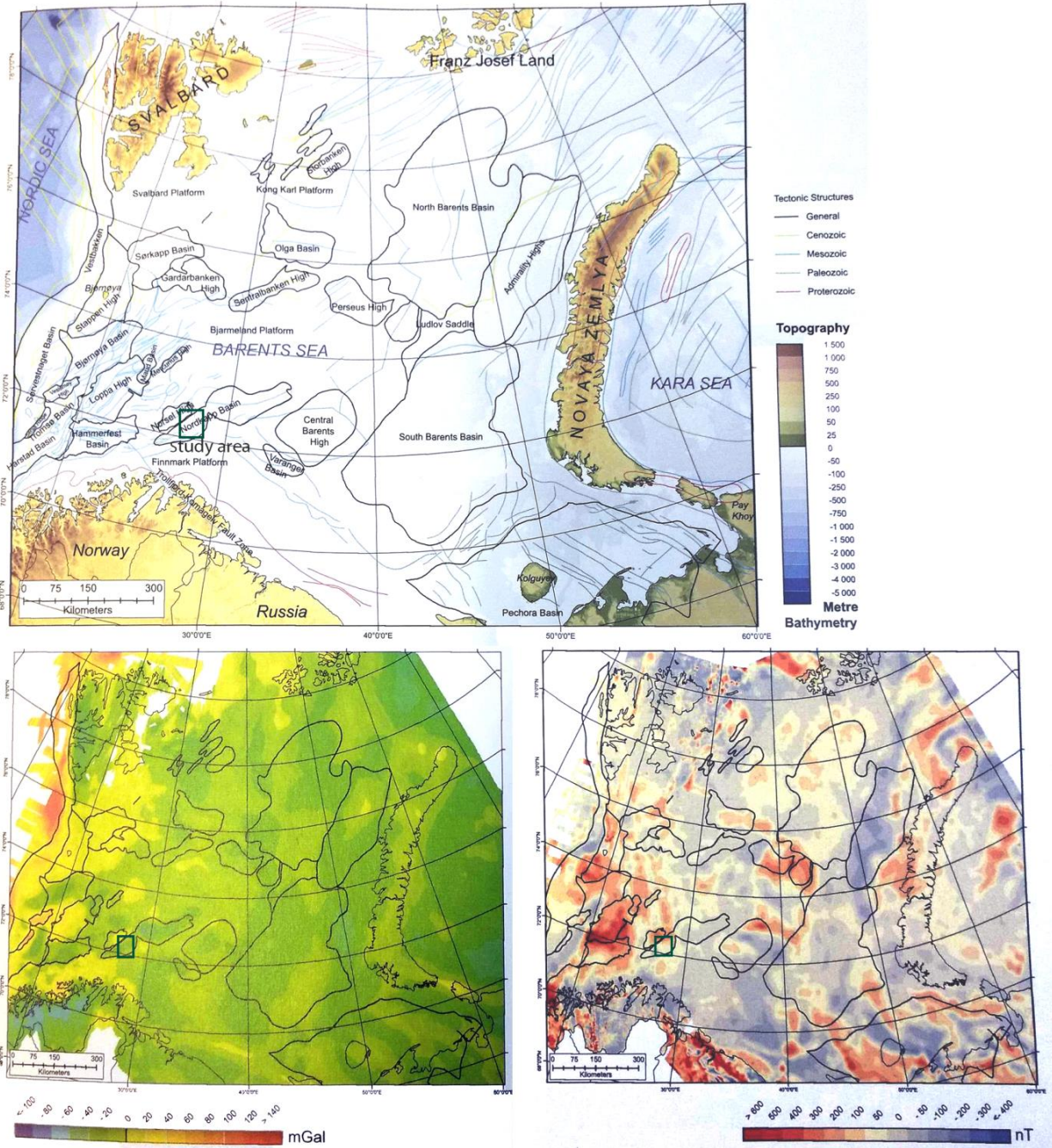


Figure 5. Map over the Barents Sea. Gravity and magnetic anomaly maps, lower left and right respectively. The study area is indicated by a green rectangle.

3.1 The Southwestern Barents Sea

The geology of the southwestern Barents Sea area has developed through a complex evolution of tectonic activity and changing climatic and depositional environment (Smelror et al., 2009). The tectonic and basement history of the area is complex, and still debated (Gabrielsen et al. 1990; Gernigon et al., 2014; Blaich et al., 2017).

The present southwestern Barents Sea consists of an intricate basement structure, and sedimentary strata aging from upper Paleozoic to Quaternary. Upper Paleozoic successions consist primarily of a mix of evaporites and carbonates, while clastic rocks make up the Mesozoic and Cenozoic deposits (Gabrielsen et al, 1990a).

3.1.1 Structural Aspects of the Southwestern Barents Sea

The western Barents Sea is a large Perm-Triassic platform with major graben type basins (Smelror et al. 2009). The largest grabens are interpreted to have initiated during Late Paleozoic extension. The basins contain large evaporite deposits estimated to Carboniferous-Early Perm age and massive Triassic deposits (Gabrielsen et al., 1990). The salt in the basins has undergone several episodes of mobilization (Koyi et al., 1993b; Nilsen et al., 1995; Gabrielsen et al., 1990b). The tectonic features observed today have retrieved their final form by Late-Jurassic early Cretaceous reactivation and lastly strong Cenozoic uplift (Smelror et al., 2009).

The western Barents Sea is bound by passive margins to the north and west. It consists of multiple basins, structural highs and platforms separated by fault complexes (Gabrielsen et al., 1990). The complex structural evolution of the area is illustrated by the many different structural elements and the interaction of these (Faleide et al., 1984). All these structural elements are reflected on the gravity and high-resolution aeromagnetic signatures.

At the western continental margin, reflection seismic show the faults, basins and highs having a general N-S orientation (sørvestsnaget), while in the central part (Hammerfest-Ottar and Nordkapp Basin) a NE-SW trending orientation is observed (See figure 5) (Faleide et al., 2015; Gabrielsen et al., 1990a). Aeromagnetic data as presented by Gernigon and Brönnert (2012), suggest that the diverse nappes and thrust sheets and their associated magnetic anomalies swing anticlockwise from the NE-SW trend observed in the southern part of the Finnmark Platform to NNW-SSE striking across the Nordkapp Basin and into the Bjarmeland Platform.

It has been proposed that the aeromagnetic data reflect an older NNW-SSE Devonian basement grain, and the seismic data reflects later, from Carboniferous onwards, NE-SW oriented structural elements (Blaich et al. 2017; Gernigon and Brönnert, 2012; Gernigon et al., 2014).

3.1.2 Geological History of the Southwestern Barents Sea

The geology of the southwestern Barents Sea area can be explained by a complex combination of large-scale processes; plate movements and changing climatic and depositional conditions. As mentioned, the main tectonic phases, as mentioned, setting the geological framework of the Barents Shelf are the Timanian, Caledonian and Uralian orogenesis, the Proto-Atlantic rifting in the west, and the subsequent Break-up and opening of the northern north Atlantic Ocean along the western margin of the shelf. In addition to these major phases are several minor tectonic events which led to large local variations in depositional regimes and paleogeography. The sedimentary basins of the Barents Sea have developed in response to the multiple post-Caledonian rift phases (Gabrielsen et al., 1990; Smelror et al., 2009).

Paleozoic

The southwestern Barents Sea basement history mainly corresponds to that recorded in the Scandinavian Caledonides (Smelror et al, 2009; Gernigon et al., 2014, Blaich et al. 2017). The Scandinavian Caledonides formed by the collision of the Baltica- and Laurentia plate, forming the Laurasian continent and resulting in the closing of the Iapetus ocean (Ramberg et al., 2008). The Iapetus Ocean was located approximately where the

Atlantic Ocean is located today. After the Caledonian Orogeny, Devonian to Early Carboniferous was dominated by deposition of Old Red Sandstones, originated from the erosion of the hinterlands (Smelror et al., 2009). Post-Caledonian rifting followed, where many of the early rifting basins developed along Caledonian structures (Gernigon et al., 2014). Timing of the early post orogenic phase of extension is unclear, but could have started in late Devonian-Early Permian (Gernigon and Brönnner, 2012; Gernigon et al. 2014; Blaich et al., 2017). This extension is believed to be controlled by the Caledonian structural grain by brittle reactivation or collapse of the Caledonian thrust system expected to underlie the Mesozoic basins, and which correlate with the regional magnetic pattern (Gernigon and Brönnner 2012; Gernigon et al., 2014).

During the Carboniferous, the southwestern Barents Sea was dominated by regional extension (Smelror et al., 2009). The northern Atlantic rift continued to progress north towards the Barents Sea in middle Carboniferous, and a wide rift zone developed in the southern Barents Sea, while strike-slip faults emerged in the north (Faleide et al., 2015). In relation to this rifting, the Barents Sea area developed segmented half-graben basins separated by faulted highs. NE-SW dominated fault trends mostly west dipping developed in the western part (Blaich et al. 2017). Several major rift basins of the Barents Sea, like the Bjørnøya, Fingerdjupet, Maud, Nordkapp, Ottar and Tromsø Basin have been interpreted to the Late Devonian- Carboniferous rift phase (Faleide et al., 2015).

During Late Carboniferous-Early Permian age, an arid climate gave rise to cycles of evaporitic platform build-ups and subsequent evaporitic deposits in the basins (Stemmerik, 2000). Massive successions of carbonate sediments were deposited and gave build ups at basin margins. (Gabrielsen et al., 1990a; Smelror et al., 2009). The sediment infill during Late Carboniferous and Permian resulted in leveling the structural relief of the Barents Sea (Faleide et al., 2015).

In late Permian age, a regional lithological change is observed. Uplift of the Uralian Mountains in the south-east and other landmasses to the south gave influx of clastic sediments (Faleide et al., 1984; Rønnevik et al., 1982). A regional basin developed in the southwestern Barents Sea area, where cherty limestones and shales were deposited.

(Larsen et al., 2013). In Perm to Early Triassic a rift phase resulted in NE-SW oriented half grabens in the western margin of this regional sag basin (Blaich et al., 2017).

Mesozoic

The end of the Paleozoic left the Barents Sea area as a large epicontinental seaway (Glørstad-Clark et al., 2010). The Triassic sediments are continuous over most of the southwestern Barents Sea, and sediment deposition in the Triassic was controlled by basins, highs and platforms developed in the Late Paleozoic (Glørstad-Clark et al., 2010). Several discrete minor tectonic events have been observed, and have influence the sedimentation locally (Blaich et al., 2017). The Early-Middle Triassic sediments consists of multiple cycles of transgression and regression, showing marine, delta and continental environments (Glørstad-Clark et al., 2010). The Middle-Late Triassic is characterized by post-rift thermal subsidence following the major rifting in Permian-Earl Triassic (Blaich et al., 2017).

Triassic deposition in major basins, including the Nordkapp Basin was strongly influenced by salt tectonics (Glørstad-Clark et al., 2010; Gabrielsen et al., 1990) The salt tectonics have been interpreted to be initiated in Early Triassic (Gabrielsen et al., 1990a, b). However, evidence have been found for salt influencing sedimentation as early as Late-Perm, indicating the Late Permian-Early Triassic rifting event as initiating salt mobilization (Bugge et al., 2002; Bugge and Fanavoll, 1995; Faleide et al., 1984; Blaich et al., 2017). In the Nordkapp Basin evidence suggest salt tectonics continued until the Late Triassic (Glørstad-Clark et al., 2010; Blaich et al., 2017). From Mid-Late Triassic, major uplift in the south, north and east Barents Sea resulted in most of the Barents Sea area being set in an alluvial plains and costal and shelf bank setting (Smelror et al, 2009). Evidence of renewed tectonic activity towards end of Triassic and into Early Jurassic has been found in Arctic and North Atlantic (Smelror et al., 2009). A large regression followed by erosion marks the end of the Triassic period (Faleide et al., 2015).

The main reservoir rocks of the Barents Sea area were deposited during the Early to Middle Jurassic (Ramberg et al., 2008). These successions comprise sandstones of very good reservoir properties, due to low clay content (ref. high porosity and permeability)

(Ramberg et al, 2008). The deposits have later been partially eroded, and the Jurassic section is overall thin in the whole Barents Sea area (Faleide et al., 2015; Glørstad-Clark et al., 2010; Gabrielsen et al., 1990).

During Middle Jurassic to Early Cretaceous the Atlantic rifting migrated north and initiated development of marine connections across the Barents shelf (Gernigon et al., 2014). The entire Jurassic-Cretaceous period is characterized by a complex structural evolution including large subsidence rates, inversion and reverse faulting and folding. This because local contraction occurred simultaneously as regional extension (Smelror et al., 2009; Gabrielsen et al., 1990).

At the end of the Jurassic period, transgressions had resulted in the flooding of the entire Barents shelf giving a deep marine setting (Smelror et al., 2009). Uplift and erosions associated with a major volcanic event resulted in the erosion of large amount of sediments, which was deposited in subsidizing basements in the west (Gernigon et al., 2014; Worsley et al. 2008). The Late Cretaceous succession which is elsewhere thin, reach up to 2000-3000 meters in these basins (Faleide et al., 2015). Successive rifting episodes during the Cretaceous resulted in rapid subsidence and development of large basins (Smelror et al., 2009). The formation of Late Mesozoic basins, including the Bjørnøya, Harstad and Tromsø basin, is interpreted to be controlled by preexisting structural features (Faleide et al., 1993). Middle-Early Cretaceous rifting is evident along the southwestern Barents shelf and major thinning of the crust have been observed in the Bjørnøya- and Sørvestsnaget Basin (Gernigon et al., 2014; Blaich et al., 2017).

Cenozoic

During the Early Cenozoic, the Norwegian continental margin formed in response to continental break-up and the opening of the Norwegian-Greenland Sea (Faleide et al., 1993). The rifting between Norway and Greenland was taken up by strike-slip movement and deformation within the De Geer Zone, resulting in pull-apart basins in the western Barents Sea (Smelror et al., 2009). As dextral movements from the shear zone progressed east, the Vestbakken Volcanic province formed south-west of Bjørnøya.

Tectonic activity had weakened the crust, and the Western Barents Sea margin formed along the strike-slip movements of the regional De Geer Zone (Faleide et al., 2015).

The Early Oligocene was dominated by rifting and marine shallowing (Ramberg et al., 2008; Smelror et al., 2009). In the Oligocene, the southwestern Barents Sea margin became stable (Faleide et al., 1993). A major unconformity is observed between Paleogene and Miocene strata (Smelror et al., 2009).

Throughout the Miocene and Late Cenozoic, the whole Barents Sea area was uplifted (Blaich et al., 2017). This uplift and subsequent erosion resulted in the loss of the Cenozoic- and parts of the Cretaceous sedimentary succession. The event marks the Upper Regional Unconformity (Faleide et al., 2015). Uplift was greatest in the north-east, and decrease towards the south and west (Ramberg et al., 2008). This uplift also resulted in tilting of the Barents Sea area in an N-S orientation. Glacial erosion of the Barents shelf, and subsequent deposition of glacial sediments as massive sub-marine fans along the margin took place in the Pliocene-Pleistocene (Smelror et al., 2009).

3.2 Geological Setting of the Nordkapp Basin

The Nordkapp Basin is one of the most characteristic features in the southwestern Barents Sea. It is a fault related intra-continental rift basin of Late Paleozoic age (Doré, 1995; Nilsen et al., 1995; Smelror et al, 2009). The basin is characterized by several salt structures, which has risen through Permian to resent sediments forming dome structures (Gabrielsen et al., 1990b; Koyi et al., 1993). The Nordkapp Basin was formed during late Devonian – Early Carboniferous as a half graben in response to regional extension (Dengo and Røssland, 1992; Gabrielsen et al., 1990b). The basin is thought to have been created by crustal extension between Greenland and Norway (Gabrielsen et al., 1990b; Larsen et al, 2013). The initiation of the basin have been dated to Early-Middle Carboniferous by correlation with regional tectonics, and the structural grain inherited from the Caledonian Orogeny is believed to partially control the deformation of the pre salt unit (Doré 1991; Gudlaugsson et al., 1998; Nilsen, 1995). The basin is about 350 km long and north-east trending (Dengo and Røssland, 1992). The dominant fault vergence of the SNB shifts from NW-facing faults in the south to SE-facing faults in the north (Nilsen et al., 1995).

The first sediments of the basin are believed to be of the Billefjorden group, making up the pre-salt succession (Bugge et al., 2002). During the Carboniferous and Permian, the Nordkapp Basin was a shallow evaporite basin where thick successions of salt were deposited (Bugge et al., 2002; Ramberg et al., 2008). Gudlaugsson at al. (1998) have proposed a different setting, where the whole Barents Sea shelf subsided, and evaporites were deposited in the deepest depocenters, like the Nordkapp Basin. Throughout the Triassic the basin environment alternated between shallow sea and dry land with massive alluvial fans (Glørstad-Clark et al., 2010). In the Middle Triassic, the basin area was marine embayment, and organic rich mudstones with source rock potential were deposited (Ramberg et al., 2008). In Late Triassic, the Nordkapp Basin area was subject to large volumes of sand, deposited from a great river system in an alluvial and coastal plain environment. These sands have reservoir rock potential, and have been shown to obtain good reservoir properties (Bugge et al., 2002; Ramberg et al., 2008).

The Nordkapp Basin is essentially a deep Paleozoic and Triassic depocenter greatly affected by salt tectonics (Smelror et al., 2009). The salt was deposited in late Carboniferous-Early Perm. Upper Paleozoic and Mesozoic sediments fill the basin and have been uplifted by active- and passive salt diapirism. Initiation of salt movement is believed to be in Early Triassic (Smelror et al., 2009). The salt pierced through the overlying successions to form pillows and diapirs. These structures caused the sea floor to bulge and salt walls pierced the sea floor forming ridges that controlled sediment distribution and depositional patterns (Ramberg et al., 2008). Initial salt movement formed local restricted sub-basins which favored deposition of organic rich sediments with source rock potential (Bugge et al., 2002). Regional uplift in the Early Tertiary followed by extensive glacial erosion in Late Pleistocene/Pleistocene removed up to 1000 m of sediments. This uplift and erosion resulted in strongly tilted and truncated strata around the diapirs. This erosion also resulted in the now thin layer of glacial sediments in the basin (Ramberg et al, 2008; Smelror et al, 2009).

The southern part of the Nordkapp Basin is a narrow ENE-WSW oriented 150 km long and 25-50 km wide basin (Gabrielsen et al., 1990a). It is hereafter referred to as the southern Nordkapp Basin, or simply SNB. The SNB contains about 17 salt structures.

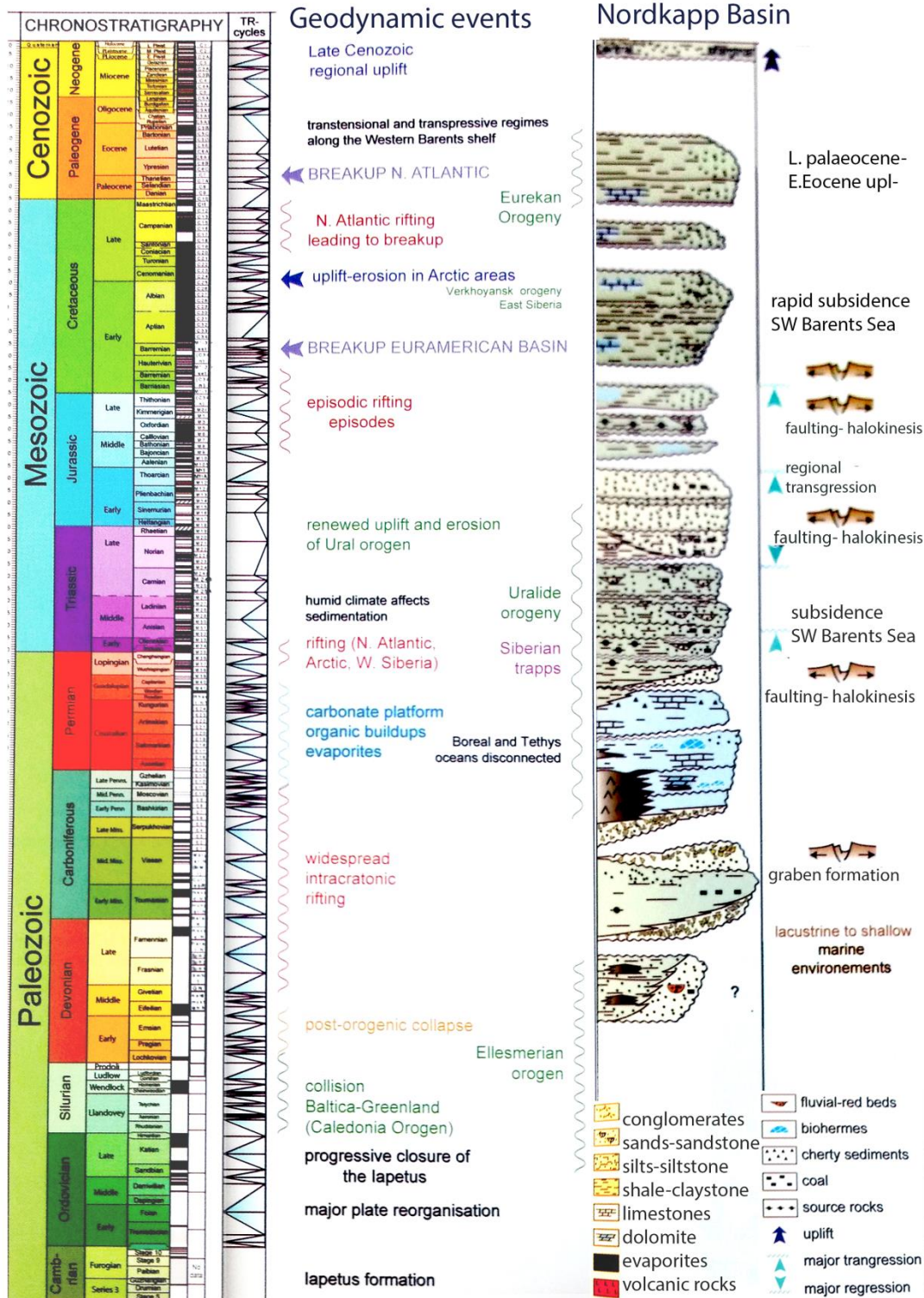


Figure 6. Chronostratigraphy with major events for the Nordkapp Basin. Figure after Smelror et al. (2009).

3.3 Salt Development in the Southern Nordkapp Basin

The salt in the SNB was deposited during the Late Carboniferous – Early Perm and locally overlap onto the basin margins (Nilsen, 1993; Gabrielsen et al., 1990a). The original salt thickness of the SNB has been estimated to 2000-2500 m (Bergendahl, 1989; Larsen et al., 2013). During the Triassic, Middle Jurassic to Early Cretaceous and Tertiary the basin has been reactivated repeatedly and affected by block fault movements which dominated the whole Barents Sea area. The basin has also along with the rest of the Barents Sea been subject to great uplift and erosion. Figure 7 gives a summary of the evolution of the salt structures in the SNB as presented by Nilsen et al. (1995).

The individual diapirs of the SNB vary in size and shape. Most are elliptical in shape in planar view and occur in two en echelon rows parallel to the major basement faults of the basin (Koyi et al., 1993). Analogue models have indicated the presence of overhangs on the salt structures, which would have formed when salt rise exceeded sedimentation during Late Triassic and Early Cretaceous (Koyi et al., 1993; Nilsen et al. 1995; Childs et al., 1993). The models demonstrate that these overhangs are most likely to be asymmetric showing preferred flow towards the center of the basin (Koyi et al., 1993b, 1995; Nilsen et al., 1995). Some authors have also found evidence for an initial pillow stage for some of the salt structures occurring during Early Triassic (Koyi et al., 1993b, 1995).

Although it is generally agreed upon that the salt diapirism was initiated in the Early Triassic, several mechanisms of initiation have been postulated. The general opinion is that the salt structures in the southern Nordkapp Basin formed in response to regional tectonics (Gabrielsen et al., 1990b, Larsen et al., 2013; Smelror et al, 2009). This theory is supported by the works of Nielsen et al. (1995) which indicate several periods of diapir growth separated by long periods of inactivity. Dengo and Røssland (1992) propose differential loading, caused by massive deposits of sediments from the Ural Mountains as a triggering factor. However, this was opposed by Dore (1991) arguing that the Urals could not supply sufficient amounts of sediments, and points to the Norwegian mainland as the source of sediments. Other authors again, Gabrielsen et al. (1990) and Nilsen et al (1995) argue that there was no large-scale differential subsidence in the SNB at this time, and points to faulting and thinning of overburden in relation to basement-involved

regional extension as the triggering mechanism (Jensen and Sørensen, 1992, Koyi et al, 1993; Smelror et al., 2009).

Seismic sections supported by analogue models suggests that the diapirs in the NSB formed in response to regional tectonics during Early Triassic and rose passively and exhausted the source layer (Nilsen et al., 1995; Jensen and Sørensen, 1992). Koyi et al (1993) have suggested that reactivation of basement faults controlled deformation of salt and overburden, and that the salt structures are located in proximity to the reactivated basement faults. Nilsen et al. (1995) however, argue that there are no correlation between the location of the diapirs and basement faults. The low viscosity of the salt would diffuse the fault propagation rather than transforming the fault (Vendeville et al, 1993). The locations of the salt diapirs are dependent on formation of half grabens in the overburden. This was again question by Koyi et al. (1995), arguing that the diffusion ability of the salt would be strongly dependent on the thickness and viscosity of the salt layer, and not necessarily the case for the SNB.

During the Middle Jurassic -Late Cretaceous the diapirs of the SNB was laterally shortened, the salt was expelled out of the stem and the diapir experienced forced growth upwards (Nilsen et al., 1995). Analogue models indicate that the diapirs would close in the narrowest point of the stem, leaving a triangular pedestal of salt at the base (Nilsen et al., 1995). The formation of overhangs would also occur where the diapir growth exceeded the sedimentation rate (Childs et al, 1993). Lateral shortening is described by Nilsen et al. (1995) to be a result of regional extension and gravity gliding from the outer basin. In the Late Cretaceous, the diapirs were again rejuvenated after being buried under +1000 m of late Cretaceous sediments. This rejuvenation has been interpreted to be caused by regional extension and gravity gliding (Nilsen et al., 1995). Extension and gravity gliding would give rise to deformation of the diapir roofs and subsequent lateral growth of the diapirs. From seismic sections, it has been interpreted that the diapir crest was eroded in Late Cretaceous (Nilsen et al., 1995).

The salt structures of the SNB were later buried under 1500 m of tertiary sediments before a new period of diapir rise occurred in the Middle Tertiary (Nilsen et al., 1995). This time interpreted to be in response to an episode of regional compression. These episodes of regional extension and compression is documented all over the Barents Sea area (Bugge et al. 2002; Smelror et al. 2009), and coincide in time with interpreted episodes of diapiric growth in the SNB (Koyi et al., 1993, 1993; Nilsen et al., 1995).

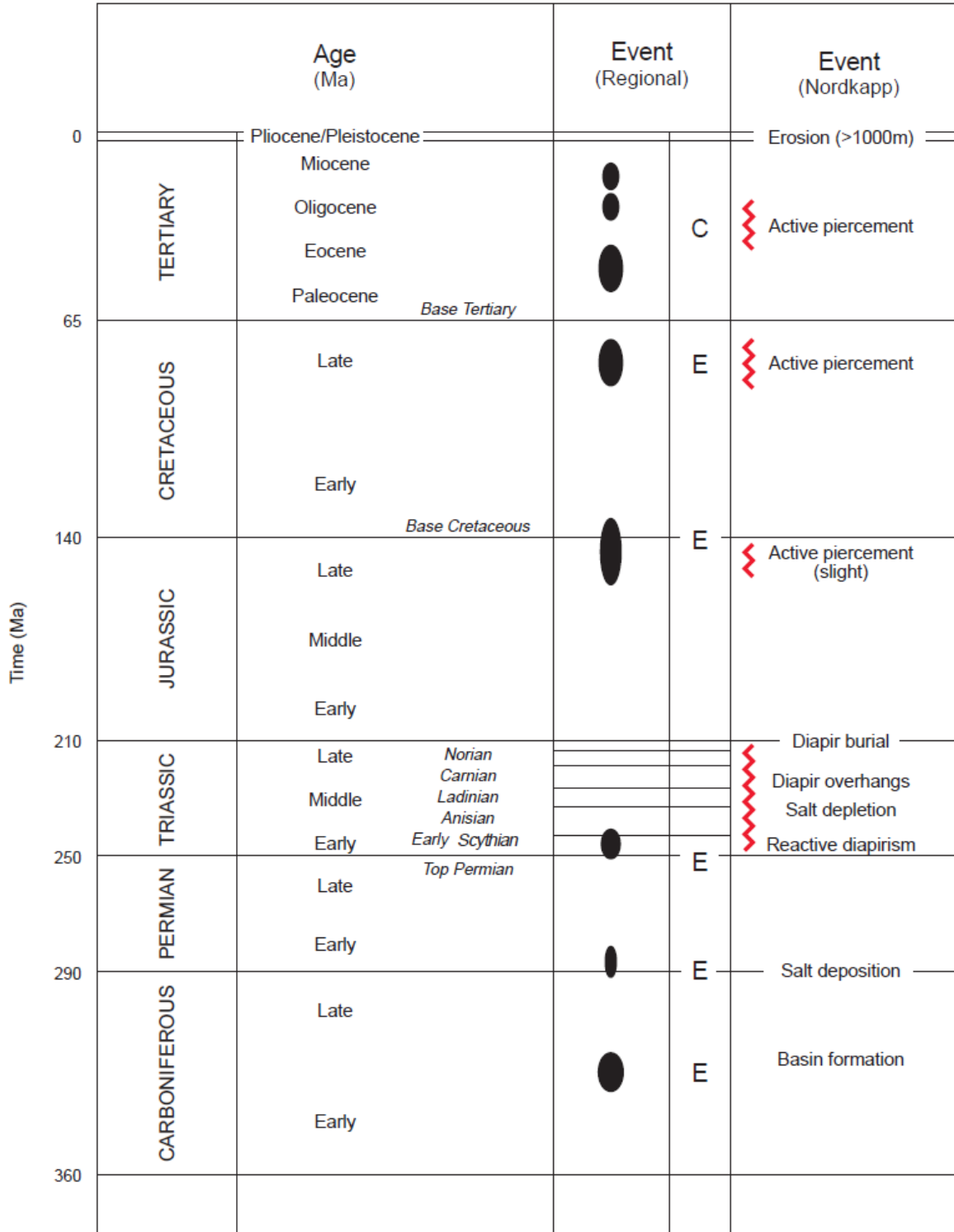


Figure 7. Evolution of the salt structures in the Nordkapp Basin as of Nilsen et al. (1995). E denotes episodes of regional extension and C denotes episodes of regional compression.

4 The Initial Model

In this study, well log data, 3D seismic reflection data and gravity anomaly data, T_z , and the vertical gravity gradient component, T_{zz} , together with the total magnetic field data, TMI has been integrated to create a geological model over a large area of the Southern Nordkapp. Information from well logs, core analyses and reflection seismic is used as conditions for inversion of the salt geometry using potential field data. Stratigraphic horizons are interpreted from seismic reflection data, and provide the geometry of the stratigraphic units. Magnetic susceptibilities derived from cores and densities derived from well logs is used to populate the layers provided by the seismic horizons. This combined interpretation gives a structural framework which is then used as constraint when performing inversions to adjust to observed gravity and magnetic data. Figure 8 shows how reflection seismic, well log data and well cores provide building-blocks of data to the model.

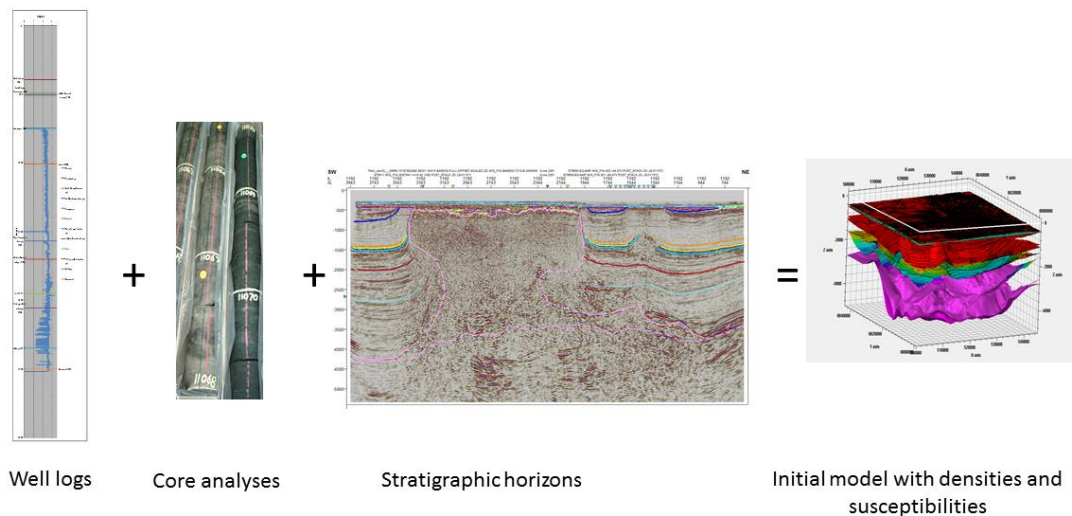


Figure 8. Illustration of how the initial model is created.

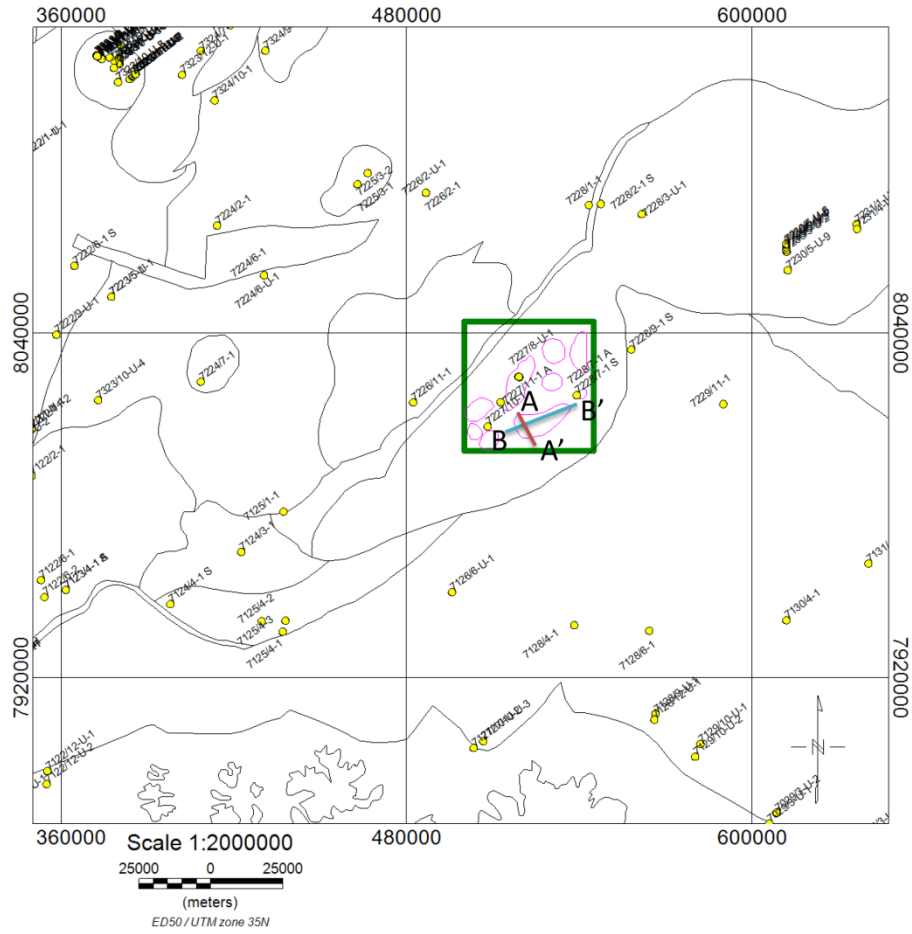


Figure 9. Figure showing the location of wells, study area (green rectangle), and the lateral extent of the diapirs in the study (pink outline).

4.1 Data

Two seismic 3D cubes: ST0369 and ST9403R01, with full-offset, migrated final post-stack data and 20 seismic 2D lines, some of which were regional lines were interpreted. The extent of the seismic data is shown in figure 10. The 2D lines were selected based on quality and coverage of the study area from the available data in the Discos-database. The quality of the data is variable, the 3D seismic is from 2015 and the 2D lines from 2014 and 2017. In general the data was of relatively good quality. Some small error is expected in the correlation between 2D lines, and with the 3D data. Some small shifts between the data could occur, but these are regarded as insignificant for the overall model.

Check shots and logged horizons tops from wells 7227/7-1 and 7227/11-1 were used for well-tie and to aid in the depth conversion, see figure 9 for location.

The full tensor gravity data is the survey ST0621 acquired by Statoil in 2006. Free-air data is utilized, as the data was acquired on ship and the datum of the model is set at sea surface level. The gravity data has been enhanced and the gradient data denoised using a 1 km wavelength filter.

The Magnetic data is the survey SNAS06. It is a high resolution aeromagnetic survey acquired by NGU for Statoil.

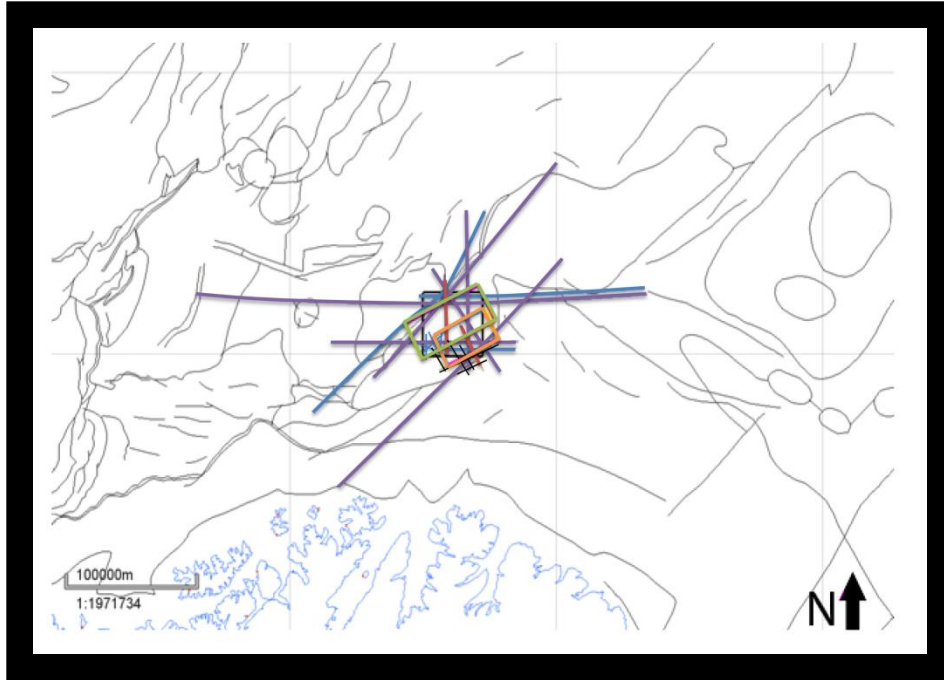


Figure 10. Map showing the location of the seismic data utilized in the study. The two rectangles (orange and green) indicate 3D surveys, and the study area is outlined in black.

4.2 Well Correlation

Wells 7227/7-1 and 7227/11-1 both lay within the study area, see figure 9. The wells contain density logs and check shots, and were made available through the discos database. In addition, the well 7227/10-1 is also within the study area, but this is a more recent well and the data have not been made publicly available. Well-tie is performed using wells 7227/7-1 and 7227/11-1 to correlate reflectors with horizons tops. The well 7227/11-1 provided limited aid, as the majority of the well section is drilled inside a salt diapir, but assisted when correlating the top salt and Knurr horizons. The well 7227/-1 was drilled down to the Klappmyss formation, and aid in picking the horizons from Seabed down to Klappmyss.

4.3 Seismic Interpretation

Horizons were interpreted throughout the data. In total 9 horizons were interpreted. The interpreted stratigraphic horizons were selected because they are major horizons of the

Barents Sea area and give a significant amplitude response. Large amplitude response from seismic data corresponds to a high impedance contrast, and consequentially represents a significant velocity- and hence density change compare to the over- and underlying units. The interpreted horizons are given in table 1. The Horizons where picked on peaks, mainly for simplicity, as the difference between a peak and a trough is regarded to be below the resolution of the gravity and magnetic data. The top mother salt horizon is taken as the top Permian reflector. This is not completely correct, but the small shift so deep in the model is expected to be insignificant for modeling purposes. The upper section units; the supra Klappmyss units, are continuous, give a strong amplitude response, and are relatively easy to interpret. The interpretation of these horizons is therefore associated with little uncertainty and can be used as constraints with good confidence. The top diapir reflector is also relatively easy to identify, but a shift of up to two peaks can occur, where the sedimentary cover over the top of the diapirs is greatly fractured. The Klappmyss and top Permian reflector are more challenging to interpret, particularly close to and underneath the salt. In addition, the top Permian horizon is not well correlated, because it has not been drilled within the study area, and the interpretation of this horizon in the seismic data is therefore subject to some additional uncertainty. The salt itself is difficult to distinguish on the seismic. It appears mainly as a blur in the sections (see figure 11). These imaging problems are due to the large impedance contrast between salt and the surrounding sediments, large velocity contrast, and the general difficulties of reflection seismic to get good imaging of steeply dipping surfaces (like salt flanks). The ST9403R01 3D surveys (green rectangle in figure 9) is of highest quality, but even here, the salt outline is unclear. Therefore, increased uncertainty for all horizons occurs under and in proximity to the salt. The base salt horizon is very difficult to pick. Only a fragmented discontinuous reflector is visible in parts of the data. Major uncertainty is therefore related to this horizon.

Horizons interpreted in Petrel were interpolated to full surfaces and used as stratigraphic units for the geological model. The interpolation of the horizons between gaps in the data can contribute to some uncertainty. Particularly the area above the Norsel High, see figure 5, where only 2D lines were interpreted can be ambiguous (figure 10). Figure 11 shows the B-cross line interpretation of a salt diapir from the seismic data. As can be observed the diapir is asymmetric, and appears to have overhangs.

Formation	Pick	Continuity	Amplitude	Color
Nordlands Group	Peak	Continuous	High	Purple
Kolmule	Peak	Continuous	High	Dark Blue
Knurr	Peak	Continuous	Medium	Orange
Fruholmen	Peak	Continuous	High	Yellow
Snadd	Peak	Continuous	High	Light Blue
Kobbe	Peak	Continuous	High	Red
Klappmyss	Peak	Semi-Continuous	Medium	Green
Top diapir	Peak	Semi-Continuous	High	White
Perm (Top mother salt)	Peak	Semi-Continuous	High	Light blue stippled
Base Salt	Peak	discontinuous	High	Blue stippled

Table 1. Seismic horizons.

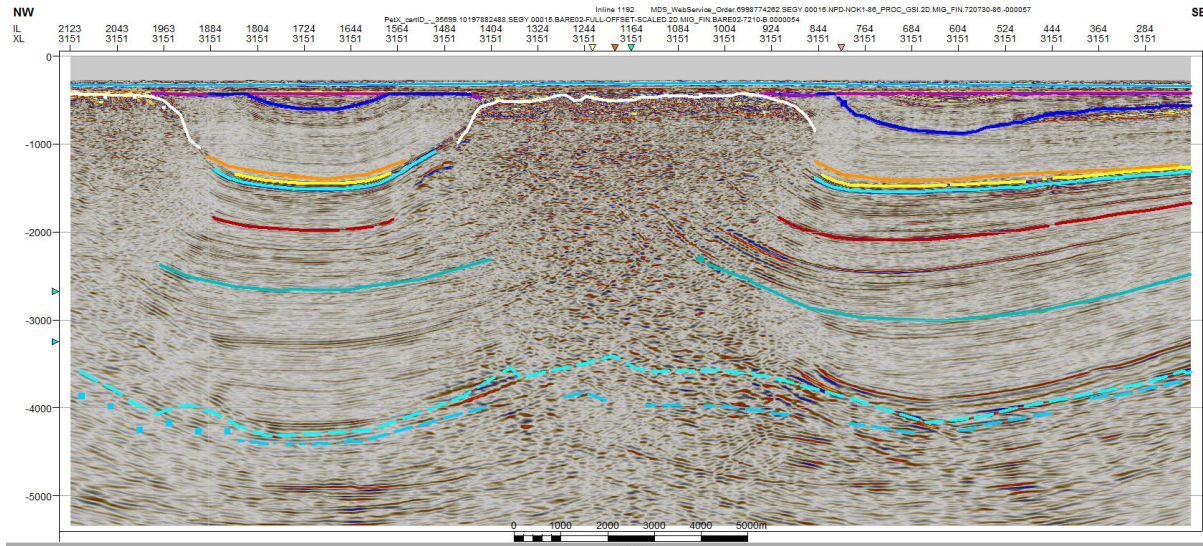


Figure 11. Seismic section. Cross section B, see figure 9 for location. See table 1 for horizons.

4.4 Depth Conversion

The model was depth converted using a simple time-depth inversion scheme based on the derived densities and the Gardner relation for converting densities to interval velocities (Gardner et al., 1974). A single velocity was derived for each stratigraphic unit, and the velocities were compared to check shots from well 7228/7-1 to control that they are within the range of the check shots (see appendix C). The depth converted model is correlated with the well 7228/7-1 and 7227/11-1 to control the depths against drilled horizon tops. A secondary conversion was conducted as some misfit with the wells was observed. The new velocities were still within the range of the check-shot values, as these cover a range of velocity values for the same unit. The main uncertainty in the depth conversion lies within the units not penetrated by the two wells 7228/7-1 and 7227/11-1 and not covered by check shots. This will be the uppermost units: Nordlands Group, top salt and Kolmule, as well as the units which the well did not penetrate: all sub-Klappmyss units. In these units only the Gardner relation is used to derive the unit velocity, and depths are not quality controlled against wells. The error in the depth conversion accumulates downward in the model; the largest errors are expected in the deeper parts.

4.5 Density Well Log Analyses

Density well log analyses for the SNB-area were performed during the specialization project by Malin (2016). Much of the following analysis is taken from this project as it also covers the study area for this paper.

The density database has been compiled from well logs inside and outside the SNB. Well 7128/6-1, 7226/11-1, 7227/10-1, 7227/11-1, 7228/7-1 and 7228/9-1 were included in the study. Well logs from wells 7227/10-1 and 7228/-1 were considered most significant, as they are located inside the study area. These two wells consist of relatively good density logs covering most of the stratigraphic sections. Well 7226/11-1, although not located inside the SNB, proved important since it contains density logs for all stratigraphic units from the Nordland Group all the way down to the basement, and so provides information not available from wells inside the basin. The locations of the wells are shown in figure 9. The densities are given in table 2.

The Knurr-, Hekkingen-, Fuglen-, Stø-, Nordmela- and Tubåen formations were combined into one unit for simplicity. The formations are very thin, and hence are undistinguishable on the gravity- or magnetic data. Other formations were combined due to lack of data. The section between the Klappmyss formation and the top Salt, and the subsalt (Permian) section were defined as two units following this principle.

Density logs were smoothed using a 9 points moving average smoothing. The result is a smoothing over approximately 1 m. Density logs for all wells after smoothing are presented in appendix A. The different stratigraphic horizons as observed in the wells are also indicated in the logs. Density logs from wells 7227/10-1 and 7228/7-1 were used to create density gradients. Where no good fit gradient could be derived from the density logs, an average density value was determined. Formations not present in the well logs from wells 7227/10 or 7228/1-1, were given average density values derived from the surrounding wells.

Only for the Kolmule formation was a gradient found which represented the density variation with depth. The other gradients were rejected due to lack of correlation of the gradients with the variations in the density log data, indicated by the low R^2 -values. A less than 20 % explanation factor is not considered sufficient to support the use of a gradient. The density of the Kolmule formation would be represented by a gradient primarily because of an explanation factor of 57%, which is highly significant. It is likely that also the Nordlands Group would have a significant density gradient, as these gradients are normally more evident in shallower layers, but as there was not sufficient data to create a reasonable robust gradient, an average value was used also for this unit. The cap rock, salt and the sub salt units have some uncertainty in the derived density values, as a result of little to no data from the wells close to the study area and inside the basin. However, all the densities are geologically reasonable and in line with densities derived by other authors for similar modeling (see Stadtler et al., 2014). The derived densities are given in table 1.

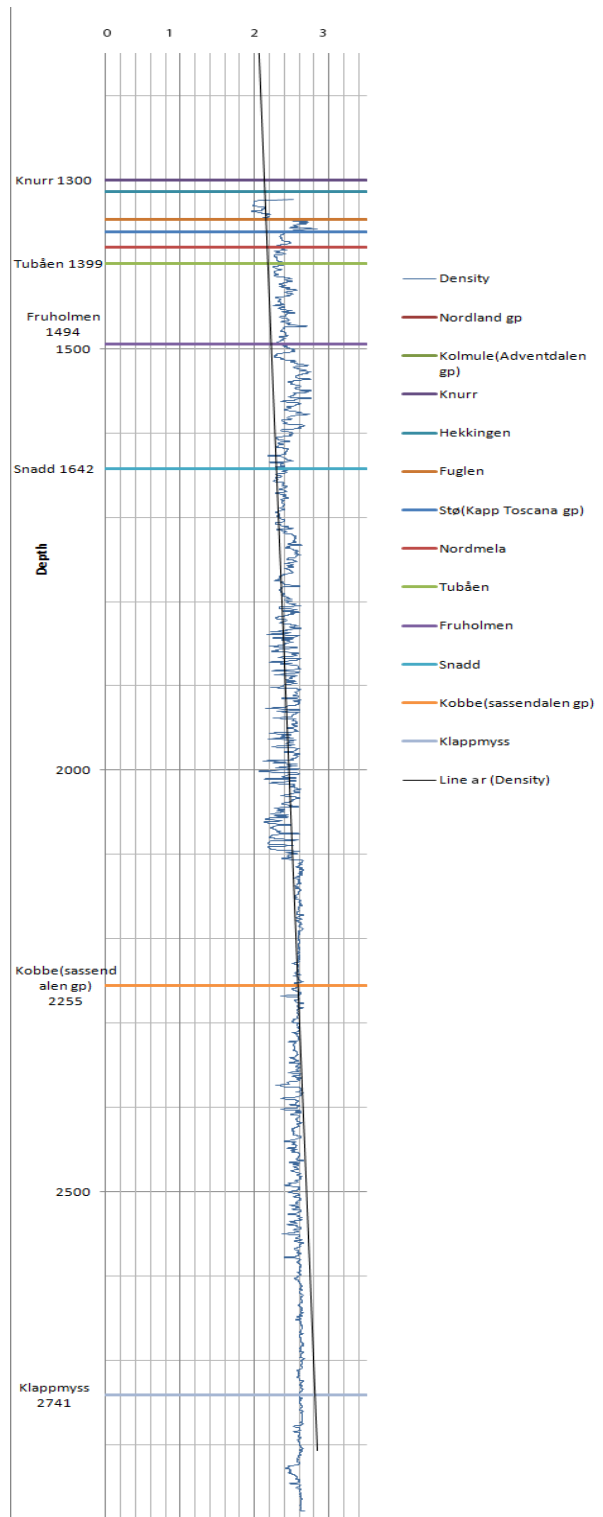


Figure 12. Density well log from well 7228/7-1.

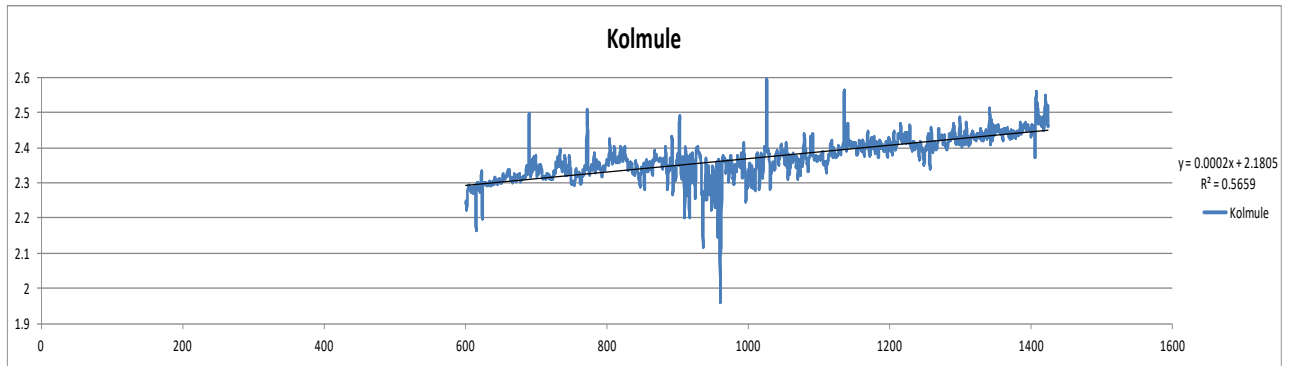


Figure 13. Density gradient derived for the Kolmule formation.

4.6 Magnetic Susceptibilities

Magnetic susceptibilities are also given in table 2. The magnetic data is mostly sensitive to the basement susceptibility, as the sedimentary rocks are assumed to have rather low magnetization. The basement magnetization is derived from a few wells offshore and the correlation with NGUs comprehensive petrophysical database for onshore Norway. The magnetic susceptibilities for the sediments were derived from literature where other authors present measurements taken on core samples, and by comparing to a similar study in the same area (see 2007; Mørk et al., 1996; Stadtler et al., 2014). A magnetic remanence of zero is assumed for the sediments, following the measurements by Mørk et al. (1996) for the mid-Norwegian margin, and some measurements from the Barents Sea.

5 Inversion Modeling Approach

An iterative inversion approach using potential field data is utilized to derive a model for the geometry of multiple salt structures inside the study area in the SNB (see figure 9). Information from well logs, cores and seismic is used as conditions for stratigraphic/structural inversions using gravity and magnetic data. The modeling in this study involves roughly 4 parts: adapting densities and magnetic susceptibility, modeling of basement, modeling salt diapir geometry and modeling mother salt geometry. As all the parts of the model influence one another, updating one part of the model requires also updating the other previously modeled parts to gradually improving the whole model. The modeling flow is outlined in figure 14. Several steps were repeated multiple times to incorporate the gradual improvements of each modeling aspects into the final model.

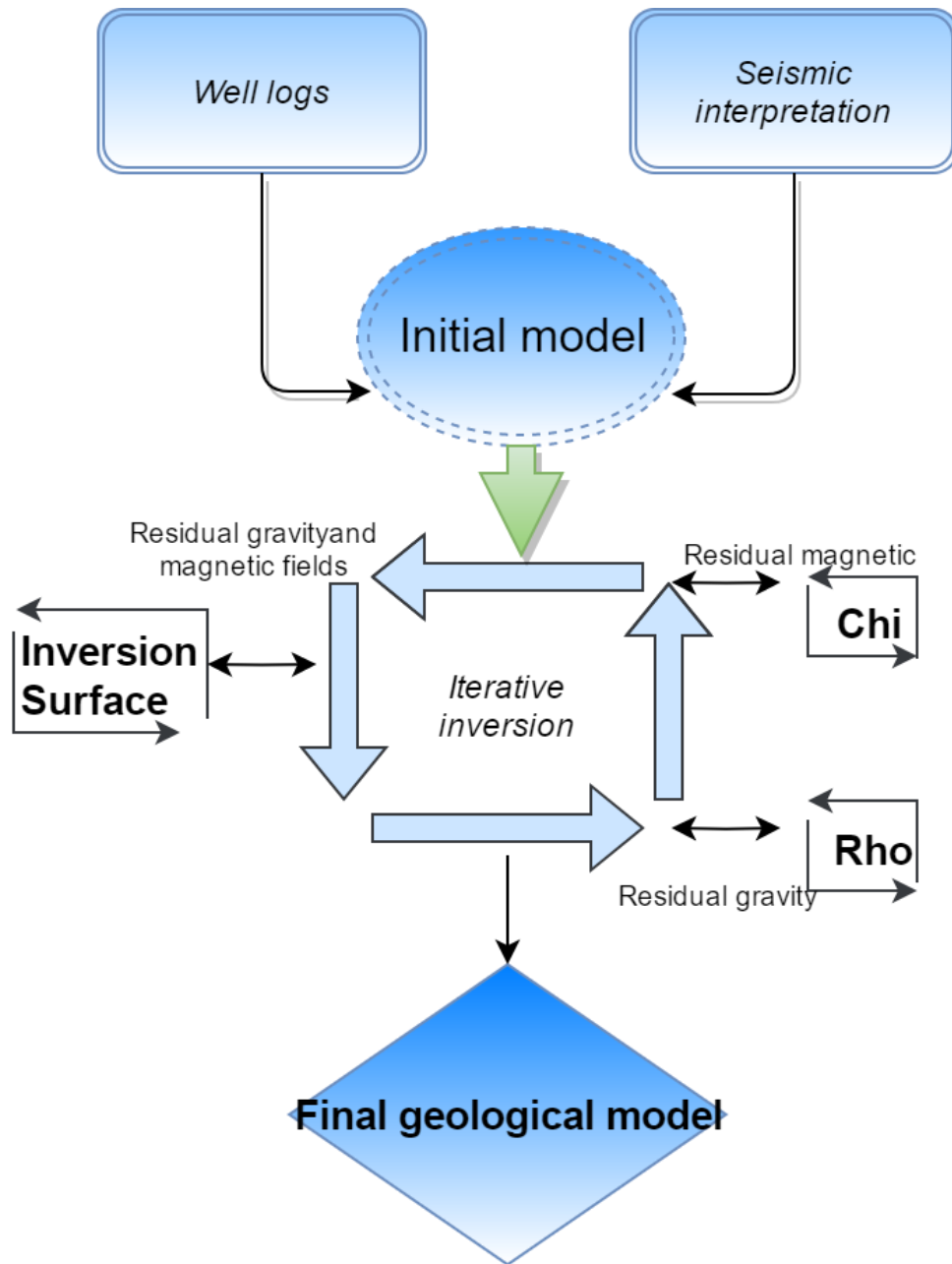


Figure 14. Flow diagram illustrating the iterative approach used to generate the model.

5.1 Software and Algorithm

The modeling was performed using Oasis montaj GM-SYS 3D Modeling, which as described by Oasis montaj, is a gravity and magnetic modeling software for surface-oriented models which provides the ability to model complicated 3D subsurface structures of any size or scale. GM-SYS 3D provides the ability to build layered earth models using gravity and magnetic data, and enables integrating them with seismic data (Oasis montaj, 2016). The 3D modeling involves calculations on the surface grids with density and susceptibility properties defined below each surface. The surface grids correspond to the surfaces interpreted from the seismic data, and all grids are extended to, and constrained by the extent of the study area (figure 9). The inversion and forward calculations are performed in the wave number domain using the algorithm derived by Parker (1972). The inversion can be performed on one grid, corresponding to one surface in a loop. It allows points on the grid to move up and down in order to minimize the misfit between the observed field and the modeled field response.

5.2 Structural Model

A structural model was created using horizons interpreted from seismic, densities derived from well logs, and magnetic susceptibilities derived from core samples. The model cover the study area of 2025 km², from seafloor down to 15 km. Surfaces interpreted from seismic data were imported into Geosoft, generating a stratigraphic framework. Average densities and density gradients derived from the density analysis and susceptibilities from core analysis were incorporated into the model. Table 2 indicated the layers, densities and susceptibilities included in the 3D model.

Because a salt dome is a multi-z body, the representation of such a body in the modeling gives a practical challenge since only single-z surfaces are supported by the modeling algorithm. The solution is to represent the enclosing surface of the diapir by two surfaces: top and base diapir. An additional layer was created 1 meter below top diapir to simulate the base of diapir. This layer would be inverted to the geometry of the base of diapir. The difference between the top and base salt diapir horizon will resemble the thickness of the salt, and be zero outside the diapirs. The salt of the model consists of three units: cap rock, diapir salt and mother salt. The salt units are defined as follows:

The cap rock is defined between the top diapir horizon and the base cap rock. This unit has zero thickness outside the diapirs, and is not included in the start-up model.

Top diapir (or base cap rock) and base diapir horizons constrain the diapir salt unit. The base diapir is the main target for this study. The horizon is treated completely unconstrained. For the start of the modeling, the horizon was set up one meter below top diapir.

Mother salt, the autochthonous salt is constrained by top and base mother salt. The top mother salt horizon is uncertain mainly underneath the diapirs, while the base mother salt horizon is largely ambiguous due to difficult sub salt interpretation. The base salt horizon is treated as unconstrained, and the top salt unconstrained under the diapirs. The initial thickness of the mother salt is set to a minimum of what could be interpreted from the seismic.

A constrain was created to limit the maximum lateral extent of the salt during the inversion. This is represented by a polygon acting as a mask. This polygon was created by analyzing the FTG grids using enhancement techniques and tilt derivative. The masking polygons are indicated in figure 9.

Formation	Density (y)	R ²	Average density (g/cm ²)	Susceptibility (μcgs)
Nordlands Group	-	-	2.20	0
Kolmule	$y = 0.0002x + 2.1805$	0.5659	2.3708	0
Knurr, Hekkingen, Fuglen, Stø, Nordmela and Tubåen	$y = 0.0005x + 1.5707$	0.0766	2.2842	0
Fruholmen	$y = -0.0011x + 4.1423$	0.1368	2.4592	0
Snadd	$y = 0.0002x + 1.9$	0.164	2.5349	0
Kobbe	$y = 0.0002x + 2.1587$	0.1918	2.5771	0
Klappmyss	$y = -0.0003x + 3.3073$	0.0486	2.5979	0
Cap rock	-	-	2.70	-0.796
Salt	-	-	2.20	-0.796
Sub salt unit	-	-	2.60	0
Basement 1	-	-	2.75	2681
Basement 2	-	-	2.75	32

Table 2. Surfaces in the stratigraphic model, correlating density gradients with R²-values and average density values and magnetic susceptibilities.

6 Modeling

This section presents some of the aspects that have been modeled, and how they affect the model in a 3D perspective. Presenting some error grids and discussing some of their implications and significance. Error grids represent the calculated model response subtracted from the observed data and show the fit of the model to the potential field data. Some aspects of the model are discussed in greater detail in 2D in the discussion section. Since the modeling scheme is an iterative approach, the different modeling steps were repeated several times. The previous steps of the model were revised when a new feature was included.

Before starting the modeling process, the initial fit of the structural model is assessed. The model goes down to a depth of 15 km. It will not include any deeper effects; deep crustal and upper mantle, which would affect the long wavelength signal of the observed data. The data is therefore processed using a filter, see section 6.1, to remove trends which are not part of the model. The initial fit of the structural model for the gravity data, without any salt structures is observed in figure 16. Increasing error is observed towards the side of the basin. This can indicate lack of fit of a basement surface. For this model, a temporary basement has been created by moving down the base salt horizons. As expected, this result in a bad fit of the model over the sides of the basin. A more appropriate basement will be modeled and replace this surface. Figure 15 show the observed gravity data. The observed increasing misfit towards the lower left- and upper right corner of the model is believed to come from a regional trend of long wavelength signal that is not included in the model. This trend will be removed from the observed gravity data by high-pass filtering.

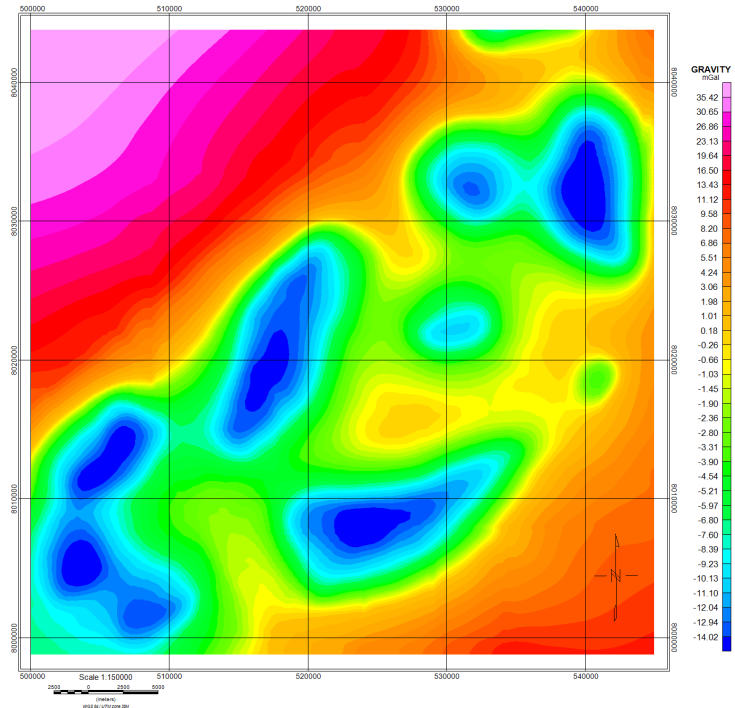


Figure 15. The observed gravity field.

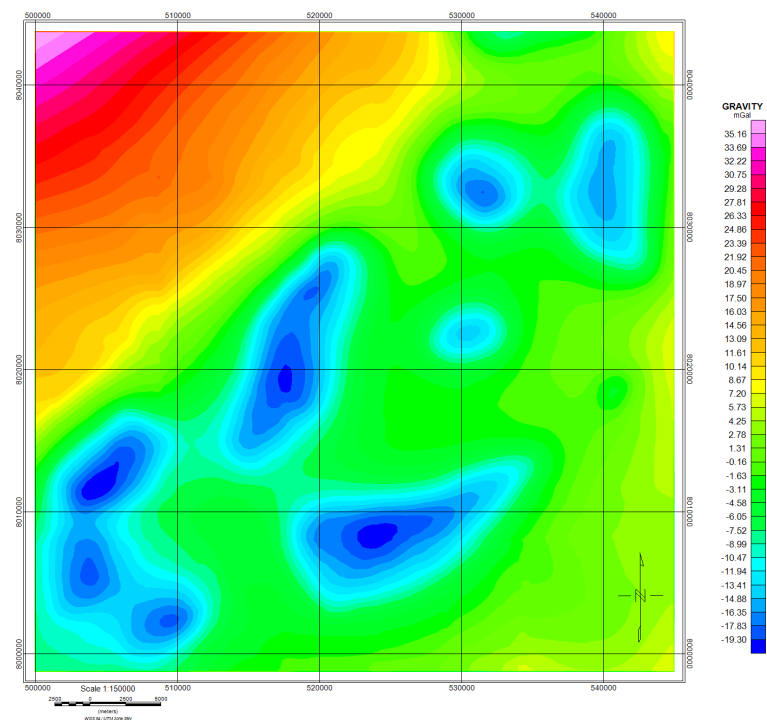


Figure 16. The error grid for the observed field and initial model.

6.1 Removing Regional Trends

Deep crustal and upper-mantle structures, and their associated isostatic effects, produce a broad increase in regional gravity values, which mask the more local anomalies of interest here (Cordell and Keller, 1984). As these are effects produced by elements not part in this model (deeper crust and mantle), the effect should be removed from the data. As proposed by Murray et al. (1989) A short wavelength gravity image emphasizes anomalies and anomaly patterns related to continental crustal structure in comparison with a total-field gravity image. High-pass filtering helps removing the obscuring effect of long wavelength anomalies.

The main objective of the study was to resolve the salt structures and any kind of filtering should ideally only remove effects from more regional geological structures from underneath the salt. To remove regional trends, a high-pass filter is applied to the Tz-data. Figure 17 show different low-pass filters applied to the Tz-data, and indicate which effects will be removed using a high-pass filter of the same cutoff wavelength. The best filter value will remove regional trends without affecting the geological response related to the model (show no response from the basin). From observing the figures, it is decided to use a high-pass filter of 70 000-meters, as there is not observed any influence from the basin, see figure 17. The response from the 80 000-meter filter is very similar to the 70 000-meter filter, while the 65 000-meter low pass appear to be influenced by the geometry of the basin seen by a curvature in the response grid. Figure 18 shows the Tz-data after applying the high-pass filter. It is observed how the anomaly map is more balanced across the basin and how the trend which could be observed from top left corner to lover right before is suppressed.

For the gravity gradient data, a different approach to removing regional trends is utilized. As described by Smith and Wessel (1990), a regional trend can be approximated by fitting a least-square plane to the data. The regional trend is removed from the Tzz-data using a built-in trend-filter in Geosoft. The trend surface is calculated by least squares fitting to all the values in the grid, or to only the values along the edge of the grid. The calculated trend is presented in figure 19. The trend filter using all grid values is used for the modeling as it is considered to be more representative for the entire data. By comparing

the result of using a high-pass filter as presented for the Tz data, or a least-square fitting as for the Tzz data, no significant difference is observed, and it is reasonable that both methods work equally well.

The magnetic data is high-pass filtered using a wavelength twice the length of the study area; 90 km. Figure 20 shows the filtered signal from the magnetic data, and figure 21 show the filtered magnetic data.

For the rest of the study only the high-pass filtered data will be used. The unfiltered data is referred to as observed fields, or unfiltered data. The filtered data is referred to as high-pass data, or simply Tz, Tzz or TMI.

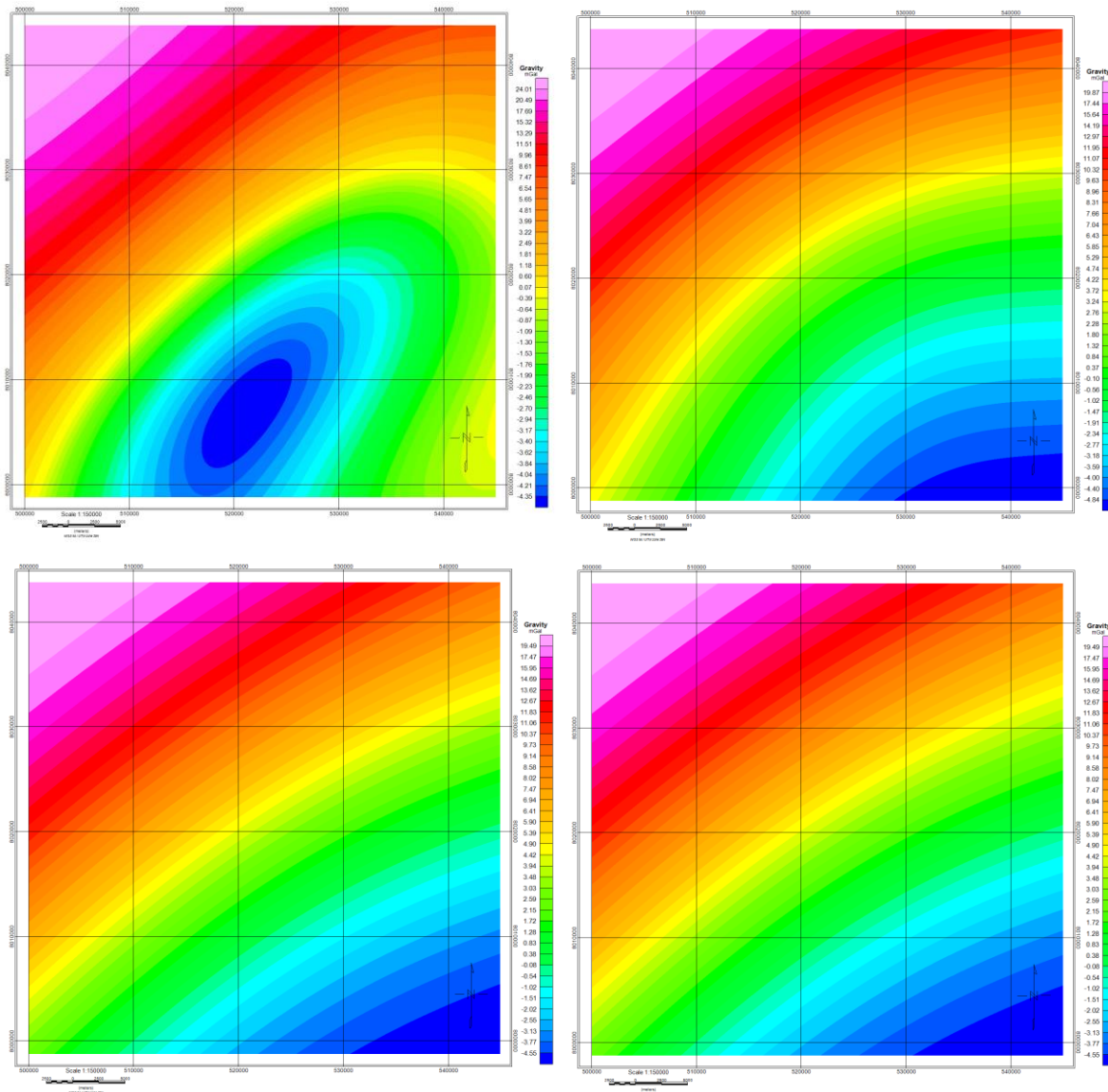


Figure 17. Low pass filtered observed Tz data. Upper left, 60 km wavelength low pass. Upper right: 65 km wavelength low pass. Lower left: 70 km wavelength low pass. Lower right: 80 km wavelength low pass.

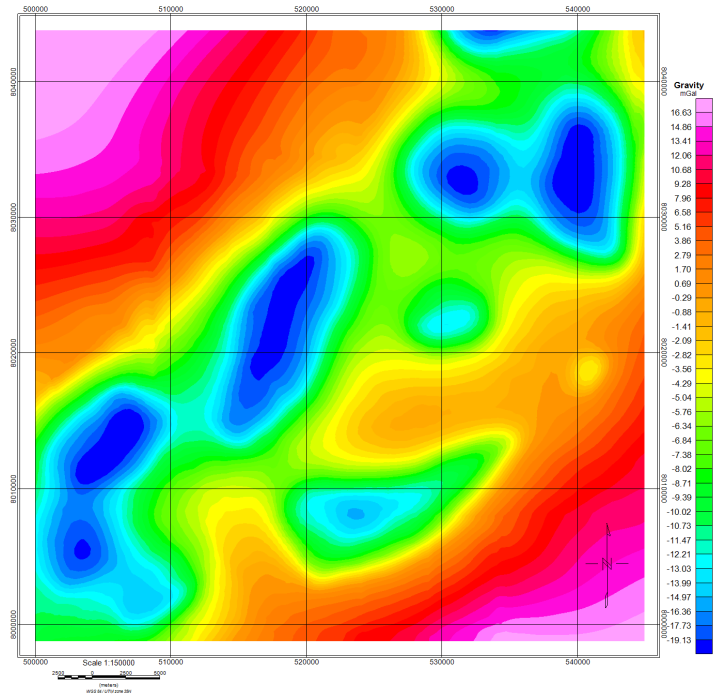


Figure 18. Observed Tz data, filtered using a 70 km wavelength high-pass filter.

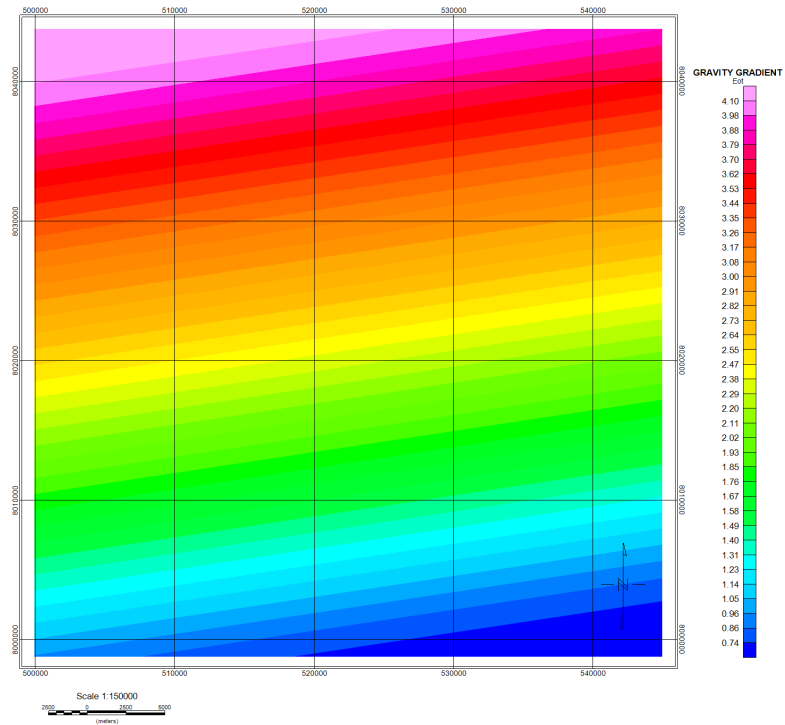


Figure 19. Trend removed from observed Tzz data using a trend filter.

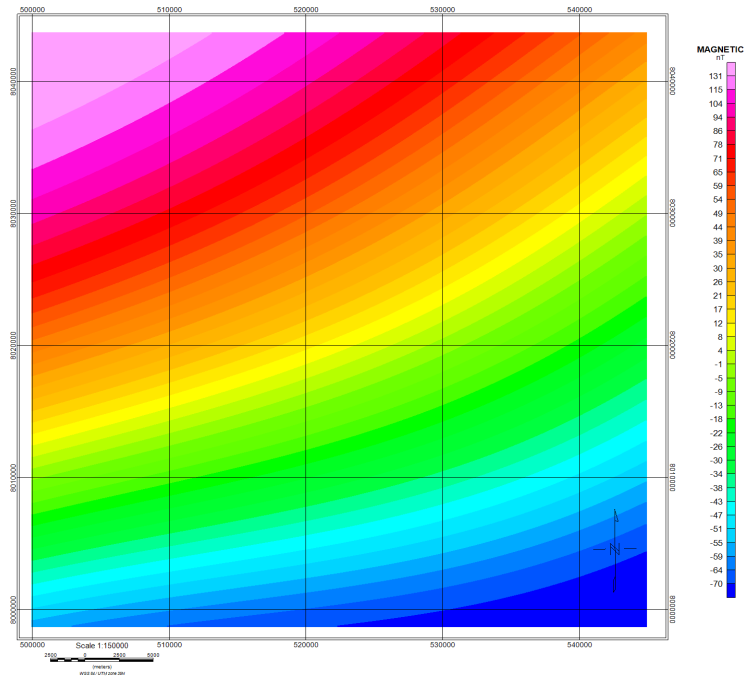


Figure 20. Trend removed from observed TMI data using a 90 km wavelength high-pass filter.

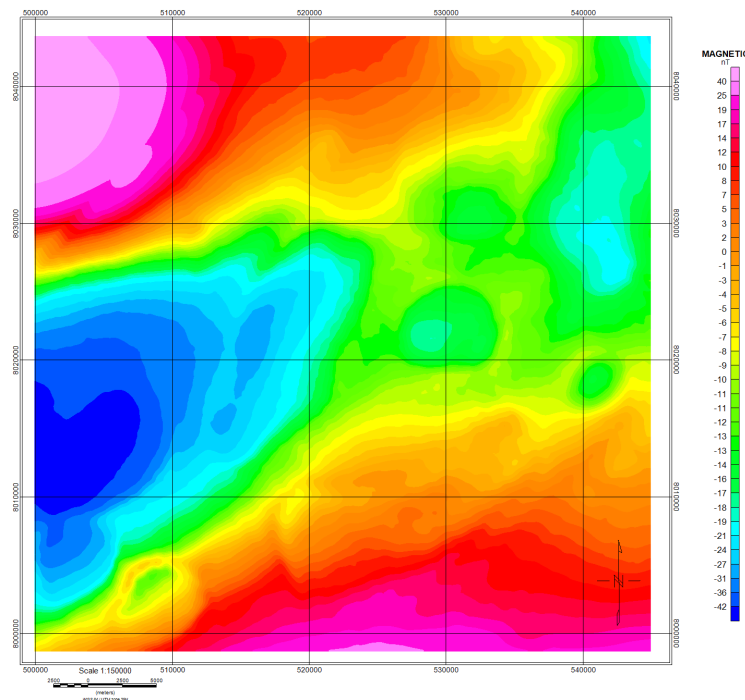


Figure 21. TMI data used for the modeling. The observed field has here been filter using a 90 km wavelength high-pass filter as descried under regional trend filtering.

6.2 Sensitivity Analysis

A sensitivity study to the model response is conducted. The gravity field, the vertical gradient gravity field and the total magnetic intensity have different amplitude decay functions (Bowin et al., 1986; Li, 2001). Tzz and TMI exhibit amplitude decay approximately proportional to $1/z^3$, while Tz decays approximately with $1/z^2$. For the gradients in general and in this study for the vertical gradient, it is expected that Tzz mainly represents the more shallow features of the model, while Tz also include effects from the deeper part. Figure 22 shows the sensitivity of the gravity potential fields to changes of the cap rock, middle diapir, and lower salt; mother salt. The Tz model responses are all distinguishable, and so Tz is sensitive to all aspects of the salt model. For the Tzz, the model response experiences high sensitivity to the cap rock changes but also a noticeable sensitivity to the base of diapir. For the mother salt, however, changes have little effect on the Tzz.

The model has three surfaces of significant magnetic contrast: top diapir-sediments, base diapir-sediments and high-magnetic basement-low-magnetic basement. Figure 24 shows the sensitivity of the magnetic model response to changes in the top and base of the diapir and the high magnetic basements. The TMI model response shows to be sensitive to changes in the top of diapir, while little sensitive to changes in the base diapir. The model response is also highly affected by changes of the high magnetic basement, as would be expected.

The Tz and Tzz model response from changing the densities of the layers by $+0.1 \text{ g/cm}^2$ is shown in figure 23. It is observed that the Tz data show sensitivity to changes in density of all the units, particularly basement density, while Tzz mainly show sensitive to density changes in the Nordlands Group and Klappmyss formations.

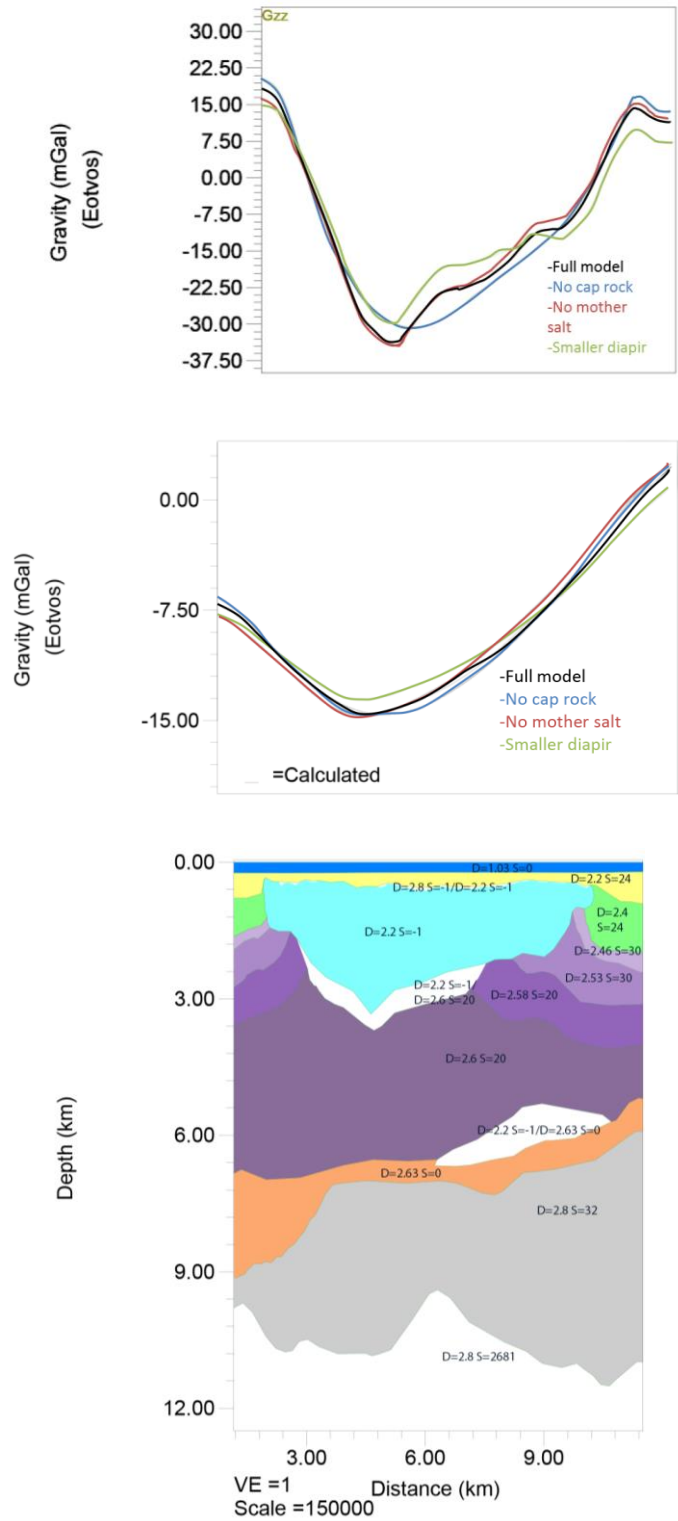


Figure 22. Sensitivity assessment for cap rock, diapir and mother salt for the model response of Tz and Tzz. Upper show Tzz, Middle Tz and lower show the model and how it has been altered for the different cases.

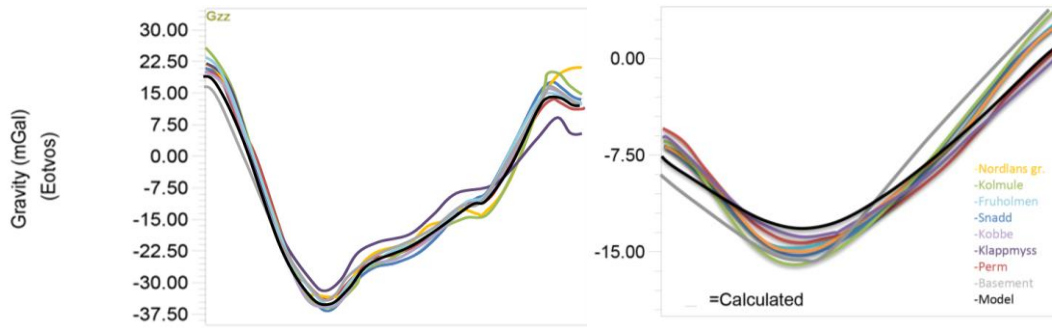


Figure 23. Sensitivity assessment for the densities of the model. The upper figure shows the model response of Tz, the lower show the model response of Tzz.

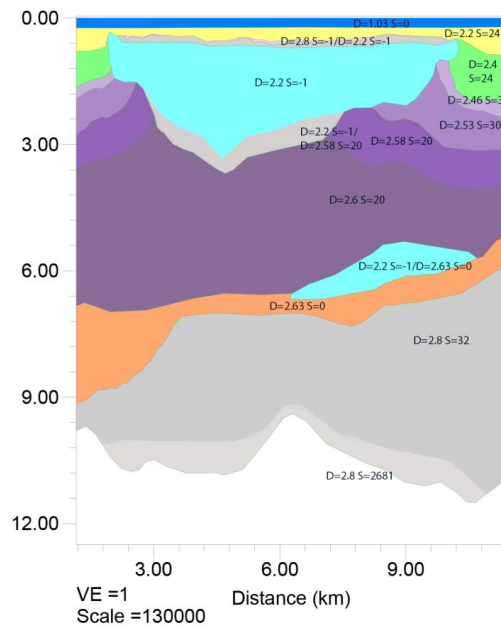
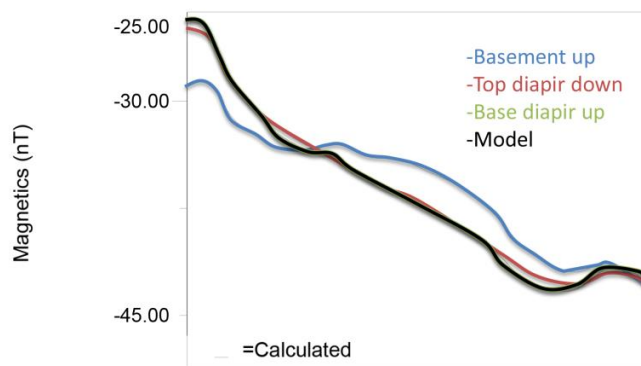


Figure 24. Sensitivity assessment for the TMI model response. Model shows the model and how it has been altered. The graphs show the TMI model response.

6.3 Modeling Basement

As defined by Smelror et al. (2009) the term top basement refers to the horizon that separates sedimentary load from crystalline bedrock, and therefore also represent the base of a basin. As the first assessment of the model indicated some misfit that was likely related to the basement, a new basement is modeled.

6.3.1 Utilizing Tz Data

It is known that the depth of the source affects the anomaly spectrum of potential field data. In some cases, it is possible to use filters to separate anomalies from sources at different depths (Bhattacharyya, 1966). Filtering the anomaly maps serves to improve the understanding of the geological configuration, and a wavelength filtering can help delineate the basement configuration.

This principle is used to try and separate the signal from the basement from that of the sediments and salt in the basin. When the basement anomaly signal is isolated it is used to invert a basement surface. A low pass filter is applied to the Tz-data to remove the effects of the salt and sediments in the basin, and the remaining field is assumed to represent the response of the basement. This will not necessarily produce a basement representative for the true basement setting, but can be considered to represent better the long wavelength response of the deeper part of the model and so aid in isolating the response of the sediments and salt and improve the salt imaging. Figure 25 shows some selected values for the low-pass filter. The key is to choose the lowest possible value to get the basement as representative as possible, while avoiding to include effects from salt and sediments inside the basin. A too long wavelength-low pass filter and the basement surface will not include the effects of margins and the basement surface will end up being too flat. Applying a too short wavelength and the risk is to account for effects of salt in the basement, resulting in basement uplift under the diapirs which is not real and subsequent too little salt in the model. After observing the different filter response, 30 000 m is selected as an appropriate filter value. The grid show no apparent influence by the salt structures, indicated by the lack of correlation between the negative anomalies and location of the salt structures, and no apparent disturbance of contour lines of the negative anomalies in proximity to the diapirs.

By comparing the model responses from using a 25 000 m low-pass over a 30 000 m low-pass filter to model the top basin surface, little difference is observed. There is however much uncertainty related to the modeling procedure used for modeling the basement, and a shallower base of the basin is possible.

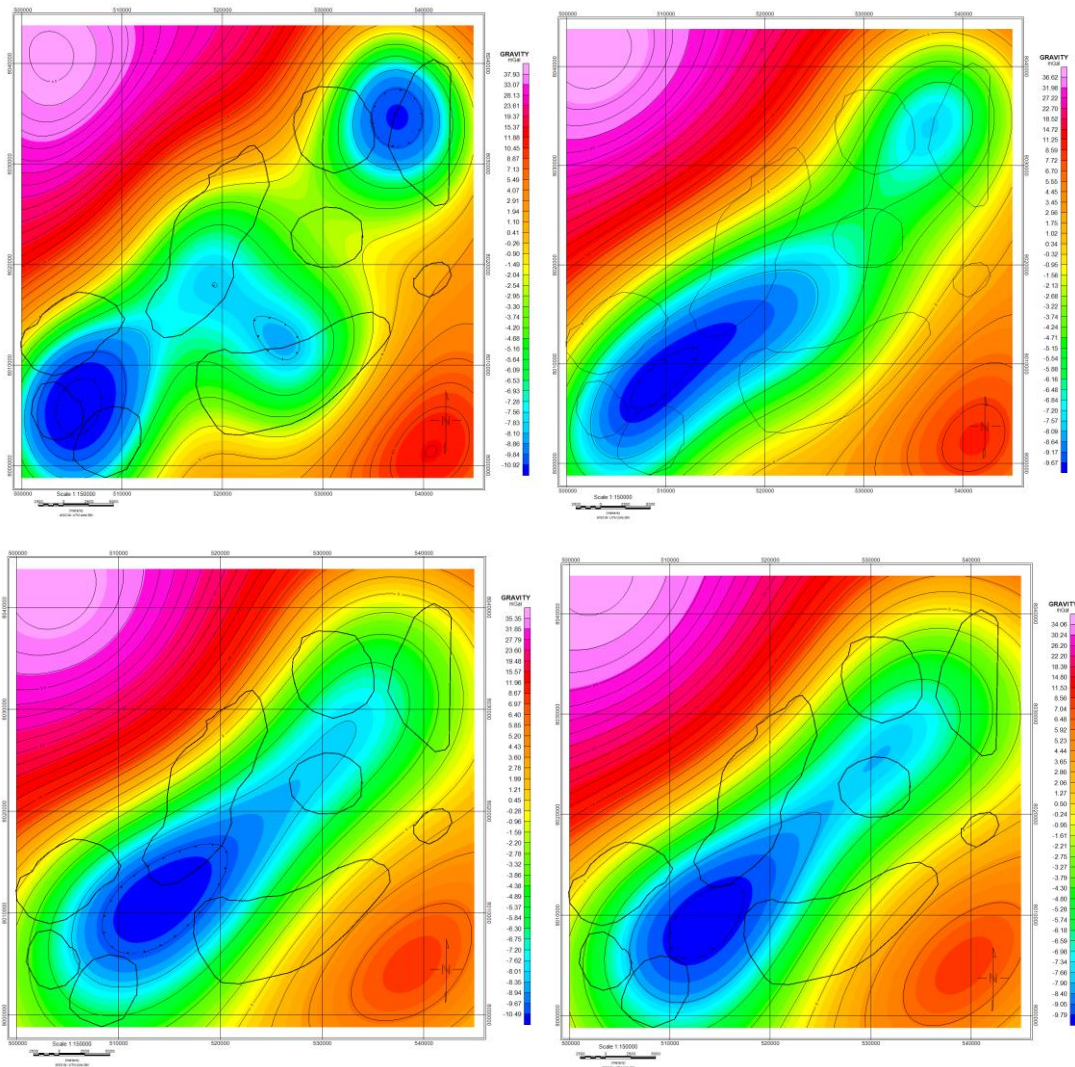


Figure 25. Selected cut of values for the low pass filtering. Upper left: 20 km wavelength low pass filter. Upper right: 25 km wavelength low pass filter. Lower left: 30 km wavelength low pass filter. Lower right: 35 km wavelength low pass filter.

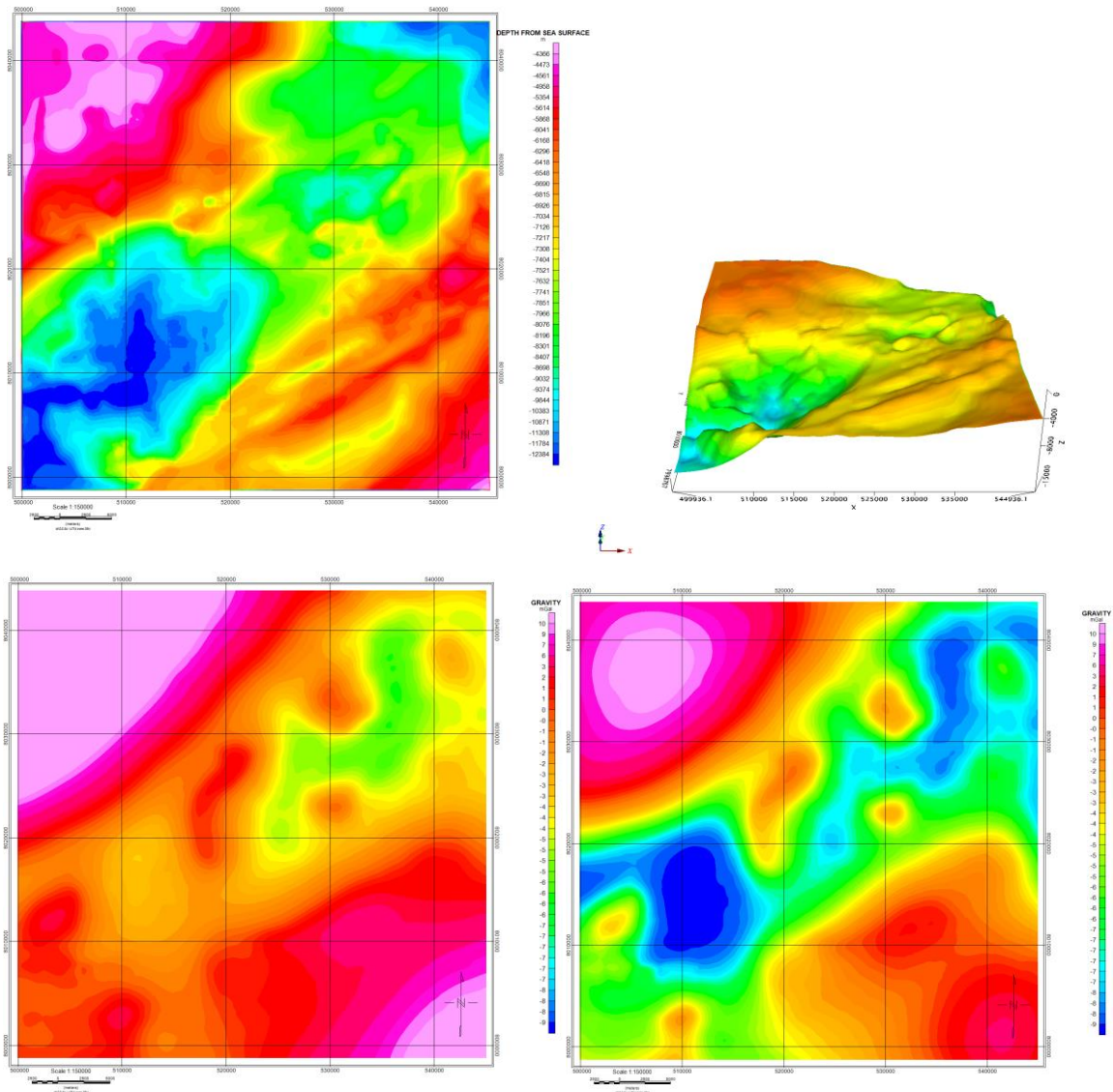


Figure 26. New basement surface. Upper two pictures show the new basement surface. The lower pictures show the model response before and after the basement surface was inverted.

6.3.2 Utilizing Magnetic Data

Typically, sediments have weak magnetization, while the crystalline basement has a stronger magnetization (Hinze et al., 2013). Because of this contrast, the top basement causes distinct magnetic anomalies which can be used to estimate the depth to basement, and basement setting (Olesen et al., 2010).

When comparing figure 18 and 21, there is a lack of correlation between the gravity and magnetic anomaly data over the basin. A poor fit is observed between the basement modeled from gravity data and the magnetic data. This illustrates the complexity of the basin setting of the area. The only area where a fit is observed is over the Norsel High (see figure 5), where both the magnetic data and the gravity show a strong positive anomaly. This might indicate a complex position of different basements in the study area.

The Nordkapp Basin is located over an area with complex basement structure (Blaich et al., 2017; Gabrielsen et al 1990b; Stadtler et al., 2014). To be able to use magnetic data for further modeling of the salt diapirs, the two basins must be accommodated in the model. An additional layer to model the magnetic basement response was included in the model. This layer is placed directly below the top basement and given a low magnetic susceptibility. The susceptibility is selected as that observed in the well 7226/11-1 (Stadtler et al., 2014) (See figure 9 for location, see Appendix A for density well log). Structural inversion is applied to the second basement surface using the magnetic data. This achieved a significant improvement in the model fit. However, there are still large errors in the model fit for the magnetic field. Inversion of the lower high susceptibility basement unit is not sufficient to account for the high susceptibility observed under the center of the basin, where a misfit still can be observed. This high could indicate that the basin susceptibilities vary laterally and a two-split basement model is an insufficient simplification and the real basement setting is much more complex.

6.4 Adapting Model Densities

As observed from the well logs in appendix A, there is some uncertainty in the density logs from the wells. This uncertainty is transferred to the model, and increased further by the possibility of lateral and local density variations. This uncertainty gives some room for refinement and the densities were adjusted during the modeling, within a reasonable range. The uncertainty is increased for the Nordlands Group, as it has only been logged for a short interval in the well 7226/11-1. Because of the uncertainty, the densities in the model can be altered within the range of the well log responses, to find the values which increase the overall fit of the model. To find the best-fit density values, the standard deviation of the error grid, the calculated model response subtracted from the observed field, is minimized.

From the decay functions of the potential field data and as discussed in the sensitivity study, it is shown that the Tzz-data are more sensitive to the shallower sections of the model compared to Tz. This would mean it is more sensitive to the densities of the upper stratigraphic units, i.e. supra Klappmyss. Tzz is therefore used to optimize the densities in these layers, while Tz is used for the deeper stratigraphic units (Klappmyss, Permian, and Basement).

The standard deviation in the error grid of the Tzz-data and model response is minimized to find the densities which gives the best fit of the model. A reduction in the standard deviation of over 20% is observed. Some positive error is still observed over the diapirs on the Tzz error grid. This could be explained by misfit in the salt diapir geometry or a possible high density cap rock.

The same procedure is utilized for the lower units using Tz. The new densities are displayed in table 3. It is observed that these densities are still within the range of the density well logs (Appendix A).

Unit	Old density (g/cm ²)	New density (g/cm ²)
Nordlands Group	2.2	2.2
Kolmule	2.37	2.4
Knurr	2.28	2.42
Fruholmen	2.46	2.46
Snadd	2.53	2.53
Kobbe	2.58	2.58
Klappmyss	2.59	2.6
Permian	2.6	2.63
Basement	2.75	2.8
High susceptibility basement	2.75	2.8

Table 3.

6.5 Salt Diapir Inversion

The base diapir horizon represents the bottom of the diapiric salt. The horizon is one of the main targets of this study, as it largely defines the volume and shape of the salt structures. Stratigraphic inversion is applied to this layer to generate the diapir geometry using Tz-data. A mask is applied outside the diapirs, as shown by the polygons in figure 9, to limit the lateral extent of the diapirs.

6.5.1 Utilizing Tzz Data

By observing the model fit to the vertical gravity gradient data, large misfit is detected. To improve the model fit to the Tzz-data, the densities in the upper section has been altered, but the fit is still not satisfactory. It is possible, as has been discussed in section 2, that the gravity model response do not separate well between salt diapir and mother salt (Hinze et al., 2013). The Gravity gradient should be less sensitive to the mother salt, and hence better represent the upper structure of the salt, the diapirs. This is in accordance with the sensitivity study, where the gradient data showed good sensitivity to the diapir, and insignificant response to a possible mother salt. The Gravity data on the other hand, showed response to changes in both salt units. This advocates the use of Tzz data for inversion of the base of the diapir surface, and the base diapir horizon was inverted using

Tzz-data. Using the vertical gradient to model the diapirs gives more sensitivity to the shape of the diapir, but it also means that the modeled diapir is subject to uncertainties associated with the vertical gradient data. As the data is more sensitive to the shallower part compared to Tz, it is also more sensitive to some errors, giving increased uncertainty. This uncertainty could manifest from mainly four areas: data accuracy, wrong densities or density variations in the uppermost units, erroneous top salt interpretation and errors in the depth conversion.

6.6 Inverting for Cap Rock

Cap rock is here characterized as anhydrite residue after salt has been dissolved, and which accumulates on top of the diapirs. The anhydrite is often moved as a result of tectonic activity in the salt dome, and may not cover the entire salt structure (Walker, 1976). Wells in the Nordkapp Basin have proven the existence of an anhydrite cap rock (well 7227/11-1 and 7228/7-1 in Appendix A). Cap rock has also been suggested by other studies on salt in the Nordkapp Basin, see Koyi et al (1993, 1995), Nilsen et al. (1995) and Stadtler et al. (2014).

From the sensitivity analysis, see figure 22, it is clear that the Tzz data is extremely sensitive to a possible cap rock. However, using Tzz to invert for a cap rock, poses an additional uncertainty in the model; separation between effects of cap rock and thickness of the diapir. For the model, this proved possible as the cap rock produces a distinctive short wavelength high anomaly difficult to achieve from adjusting the base diapir horizon, see difference in sensitivity response for cap rock and base diapir for Tzz figure 22. However, it is possible that there is more cap rock present compared to what is displayed in the model. Figure 27 show the cap rock thickness in the model. By comparing figure 27 to the topography of the top diapir, figure 28, a correlation is observed. The cap rock appears to be thickest in depressions of the top diapir. It is possible that the cap rock has accumulated in the depressions of the top diapir, or that it has been erode from the top during uplift and erosion.

Tzz data was used to invert the base cap rock horizon. The cap rock proves to improve the fit of the Tzz model response. However, the model response of the Tz-data shows an increased misfit.

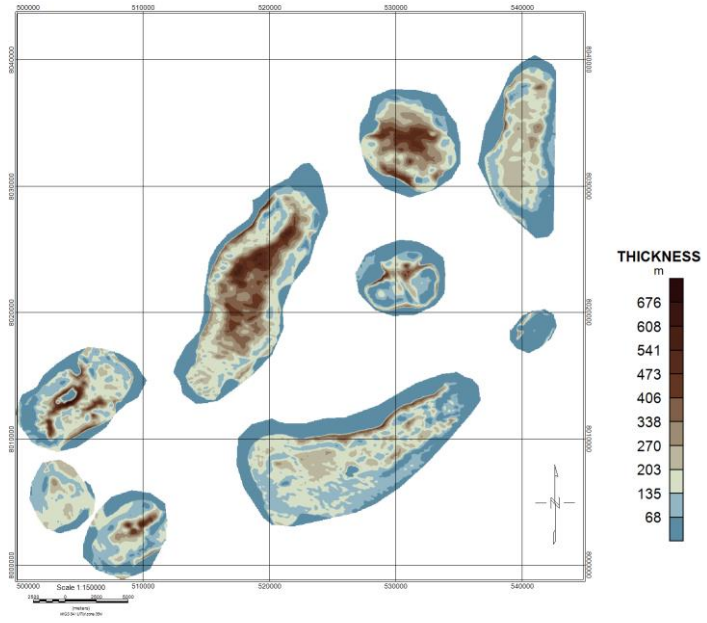


Figure 27. Cap rock thickness.

6.7 Inverting for Mother Salt

Some authors have postulated the existence of mother salt still present in the SNB (Koyi et al., 1993; 1995), although it might be almost depleted and constricted to under the diapirs (Nilsen et al. 1995). The sensitivity analysis shows that a mother salt would have a significant effect on the Tz model response, and the Tz data is therefore used to invert for a possible mother salt. Tz was used to invert for a mother salt after the diapir salt had been adjusted to Tzz. The base salt horizon is first inverted, as this horizon is considered unconstrained. After, the top salt horizon was inverted, using the salt mask as shown in figure 9. The mask will restrict the inversion to the areas of limited seismic interpretation, where the horizon is treated as unconstrained, sub diapirs.

6.8 Correlate Magnetic Data with Diapir

The magnetic data shows good sensitivity to the top of diapir salt surface, but less sensitivity to the base since the magnetic contrast is very little between the salt and the sediments, and the fields decay by $1/z^3$. This sensitivity to the models shallowest part makes it possible to use magnetic data to some extent to evaluate the depth conversion of the top diapir horizon. As mentioned this depth conversion is subject to some uncertainty because the depth well logs and check shots does not cover the entire stratigraphic section covered by the model. In addition, the sediments on top of the diapirs can vary from what is found around the diapirs and be greatly fractured, which both will affect the velocity in this unit. From the sensitivity study, the magnetic data is found to be extremely sensitive to the top diapir surface. Therefore, the magnetic data is used to do a check of the depth conversion of the top diapir surface. By performing integration on the top diapir surface, and comparing this surface to the original top diapir surface and observing the difference some evaluation of the depth of the top diapir can be made. The top diapir surface is seen in figure 28, and the difference between this surface and the top diapir fitted to magnetic data is shown in figure 29. Figure 29 could indicate some error in the depth conversion or errors in the interpreted top diapir surface. This method is extremely dependent on having well defined magnetic susceptibilities for the salt and the sediments over the salt. It is also important to know the extent, and susceptibility of the cap rock. This method becomes possible due the shallow top salt in the Nordkapp Basin. The magnetic data is sensitive to changes in the susceptibility of this shallow part of the model, but also more sensitive to errors in the model susceptibilities. For the southern Nordkapp Basin, wells have been drilled to examine the susceptibilities of the sediments,

salt and cap rock (see Mørk et al., 1996), which makes this approach possible. However, this approach would require further investigation, and for this model the top diapir is treated as constrained and the method used only to examine insecurities in the top diapir surface.

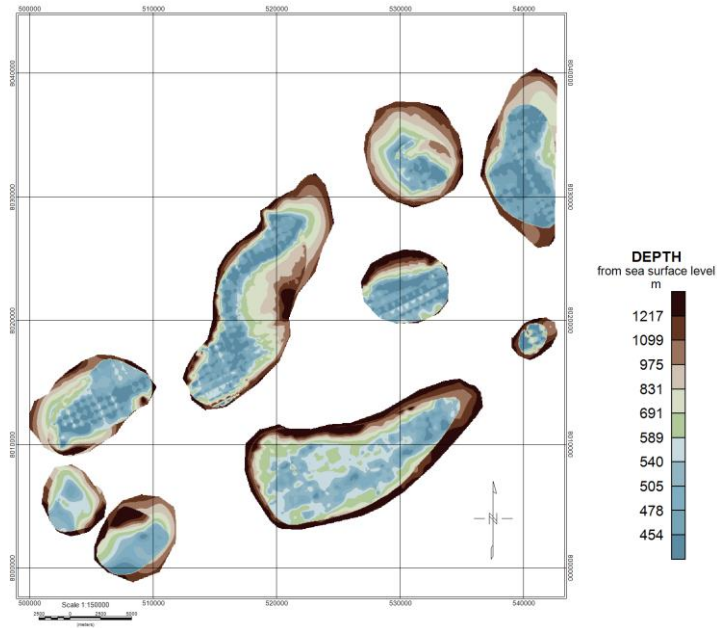


Figure 28. Depth to top of diapirs. From sea surface level.

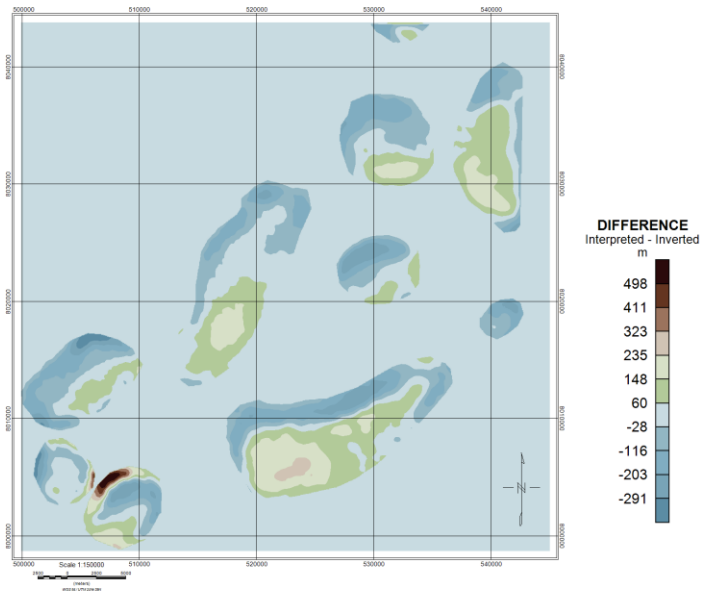


Figure 29. Difference between interpreted and inverted top diapir surface. The inverted surface has been subtracted from the interpreted, so areas showing negative magnitude have moved up, and vice versa.

7 Discussion

In this work, the seismic interpretation of salt structures in the southern Nordkapp basin was tested and modeled using gravity, gravity gradient and aeromagnetic data to derive a more reliable imaging of the sub-salt structures. The use of Tzz data to derive the geometry of the salt diapirs is a new approach compared to using Tz as has been done previously (Stadtler et al. 2014). The sensitivity analysis indicated differentiation from Tz and Tzz between diapiric salt and mother salt, and a good model fit has been achieved using this approach. It was found difficult to get an equally good model fit for the vertical gradient if the diapir had been inverted using Tz data. The final model response is observed in figure 31, 33 and 35. The figures show the calculated model response. The high-pass filtered data is observed in figure 30, 32 and 34. The final salt model is shown in figure 36. The model shows linear salt structures, canopies as defined by Fossen (2010), in rows inside the basin. Most of the salt structures are elongated in directions NE-SW in planar view, the exception is the structure in the northeast corner of the study area, showing N-S elongation. However, all the structures are elongated semi-parallel to the basin margin. The salt is primarily detached; indicating the maturity of the area (Fossen, 2010). The salt model gives improved constraint on the salt geometry and compliments the salt interpretation in areas where the seismic lacks resolution.

The cross sections in figure 38 and 39 can be used to illustrate how the diapirs have evolved. In cross section A and B, it is shown how the shape of the diapir closely follows the Tzz data. This is particularly evident in cross section A, where the base of the diapir follows the anomaly in the ramp shape toward the basin margin (right) and steep dip towards the basin (left). Cross Section A shows a cross section over one salt structure perpendicular to the basin margin (see figure 9 for location). Here it is observed how the base is rounded, asymmetric and shows a ramp structure. This model contrasts with the interpretation from seismic data made by Nilsen et al. (1995), of the same salt structure in almost the same cross section (figure 13 in Nilsen et al. 1995). They have here interpreted salt overhangs. Salt overhangs is not found in the derived salt model, and indicates how the seismic shows poor imaging in the sub salt areas, and how potential field data can constrain and improve the interpretation. The section also shows the mother salt, as a pedestal under the diapir. This type of mother salt can be interpreted as the

result of regional tectonics and gravity gliding pinching of the stem of the diapirs, as in the analogue models by Nilsen et al. (1995). It is a feature that one not would expect from salt rise from differential loading. This interpretation agrees with Gabrielsen et al. (1990b) Koyi et al (1993, 1995) and Nilsen et al. (1995) that the salt structures in the southern Nordkapp basin has been initiated by fractures, and the growth driven by regional tectonics. Differential loading as the driving factor, is discard simply due to the shape of the diapirs. The diapirs occurring from differential loading would be much more symmetric, as is observed in the model by Trushiem (1960) (See section 2.1.2).

As mentioned previously, the base of the diapir show ramp structures towards the outside of the basin. From Koyi (1998) these types of ramps in the base of a diapir can be linked to episodes of diapir growth. If considering the approximate timing of these events from the surrounding sediments, at least two episodes of forced salt growth is observed; an Early- to Middle Triassic, and a Middle-Late Triassic episode. In fact, Gabrielsen et al., (1990a, b) inferred major rifting episodes in the Triassic, supporting the interpretation that growth of the diapirs has been influenced by regional extension (Blaich et al., 2017; Gabrielsen et al., 1990a, b; Larsen et al., 2013, Nilsen et al., 1995).

In Cross Section B, figure 39, it is observed how the salt structure appears to constitute at least three smaller structures along the section. The small salt structures have stretched towards NE (right in the section), and merged together. This stretching can simply be caused by deepening of the basin towards northeast, and the diapirs have consequentially glided toward the basins deeper part because of basin subsidence (Koyi et al.1993b; Koyi 1998). Gravitational gliding, has earlier been proposed by Nilsen et al. (1995). This event would coincide with documented subsidence in the Nordkapp basin; see figure 6 (Smelror et al., 2009; Gerniogon et al., 2014). However, Nilsen et al. proposed gravity gliding in the southern Nordkapp Basin to be towards the center of the basin, perpendicular to the basin margin, as is indicated in cross section A. It is possible that the diapir has experienced gravity gliding in NW direction, and that basin subsidence has caused the diapir to sag towards N-NE.

Koyi et al. (1995) showed on analogue models how salt structures were initiated by faulting of the overburden and developed along strike of these faults. The structures will develop as multiple diapirs along the fault and go over into salt rollers, just as observed in cross section B. If the salt structures develop along strike of initiating fault, they would also show the location and strike of the fault that have initiated the salt tectonic. This agrees with the overall interpretation that diapirs were triggered by thinning and fracturing of the overburden probably during an episode of basement involved regional extension. If considering Koyi et al. (1993b, b, 1995), the salt diapirs would develop in proximity to basement faults, and the salt diapirs would consequentially indicate where basement faults have developed, and as stated in Chapter 3, indicate inherent structural grain.

On the other hand, if one considers the analogue models by Nilsen et al. (1995), the location of the diapirs concurs little with the location of basement faults. The pattern of diapirs would represent weakness zones in the overburden and not the basement. Considering this interpretation little is inferred from the salt model regarding the basement setting of the Nordkapp Basin. This model would explain why it is difficult to find one trend to explain the strike and location of all the diapirs in the basin (figure 37). However, if one observe the base of the diapirs (figure 37), three different trends are observed, a N-S trend for the diapir in the top northeast corner of the study area, a NNE-SSW trend, and a Ne-SW trend, which is the predominant trend. Both the NE-SW- and the NNE-SSW trend is observed in some of the diapirs (figure 37). This would indicate that the orientation and location of the diapirs is not just a result of overburden weaknesses, because it is very unlikely that two different weakness trends in the overburden would occur simultaneously. One could rather speculate that the additional lineation is related to a correlation between diapirs and basement grain.

Considering the three trends observed in the base of the diapirs one can discuss whether and to what extend these trends are inherited from basement faults. Following the interpretation that the salt structures developed along basement initiated faults; these trends are consequently linked to the basement history of the Nordkapp Basin. The coexistence of the three trends would then indicate the complex basement history of the area and the interpretation of these trends could help to reveal the tectonic development of the Nordkapp Basin.

The NE-SW trend observed in the salt structures follows the basin margin. It is interpreted to be related to the Late Paleozoic rifting that resulted in the formation of the half graben structure that is the southern Nordkapp Basin (see section 3.2). This trend reflects the major rifting phases most likely involving the basement, and basement faults following the same grain as the basin. Nilsen et al (1995) have interpreted this orientation in basement fault, (see section 3.2). Consequently, the structure of the salt diapirs is reasonable to interpret as basement fault affected.

The N-S trend observed for the one structure in the upper northeast corner of the study area is interpreted to be related to the structural high between the northern and southern Nordkapp Basin. Here one can assume shear faulting along the border faults of the c. N-S striking late Paleozoic basin east of Norsel High as suggested by Gernigon & Brönnert (2012). It is as such, interpreted to be different from the rest of the structures in the basin, because it would be heavily influenced by the faulting in this high. A fault in the northern end of the SNB, giving some basin subsidence in late Triassic, would explain why the diapirs show signs of sagging towards this end of the basin, as is observed in cross section B.

The NNE-SSW trend observed in some of the salt structures is interpreted to an older inherent structural grain. This structure is the weaker one of the two main trends (excluding the N-S trend), and is observed in structures showing a more dominant NE-SW trend. The lineation is not found in all structures, (see figure 37); supporting the idea that this orientation is an inherent grain from pre-Permian times. These types of grain has been observed in magnetic data over the whole Barents Sea area, (see Chapter 3), and could indicate the presence of an older basement, with a different structural grain than the NE-SW grain previously interpreted in the area. This agrees with the interpretation by Gernigon and Brönnert (2012) and Blaich et al. (2017) of the possibility of old pre-Permian c. N-S striking basins, with a different grain compared to the NE-SW trend observed in basements on seismic data, and which could have caused accommodation faults in this direction within the southern Nordkapp Basin?.

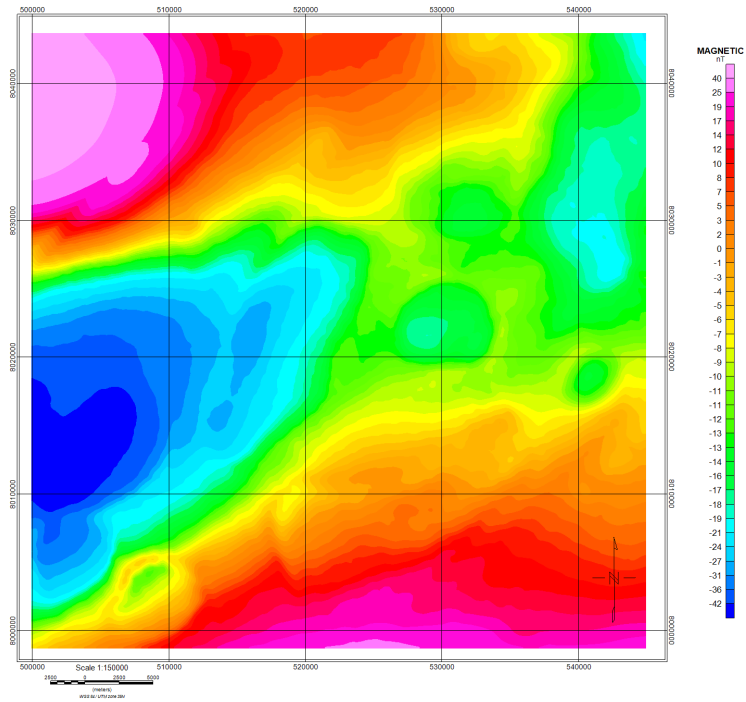


Figure 30. Magnetic field data used for modeling.

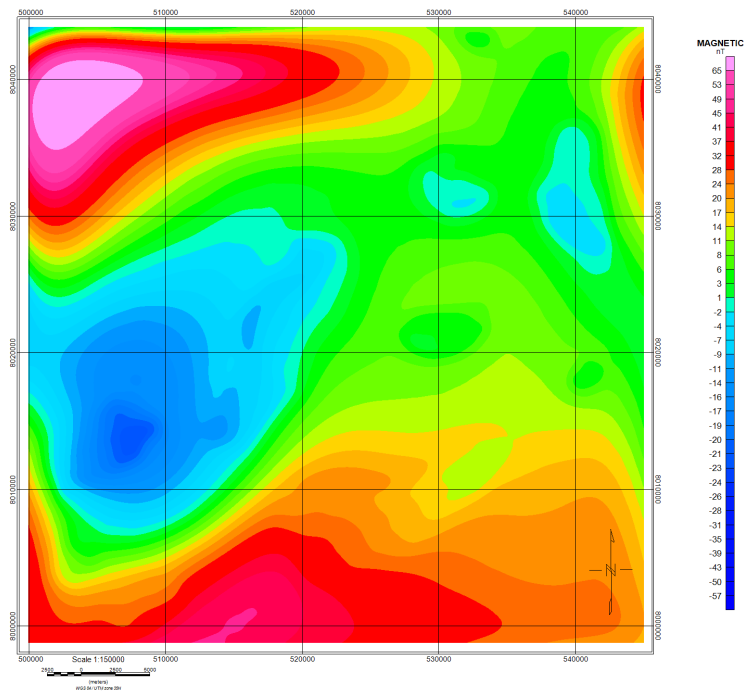


Figure 31. Magnetic field model response.

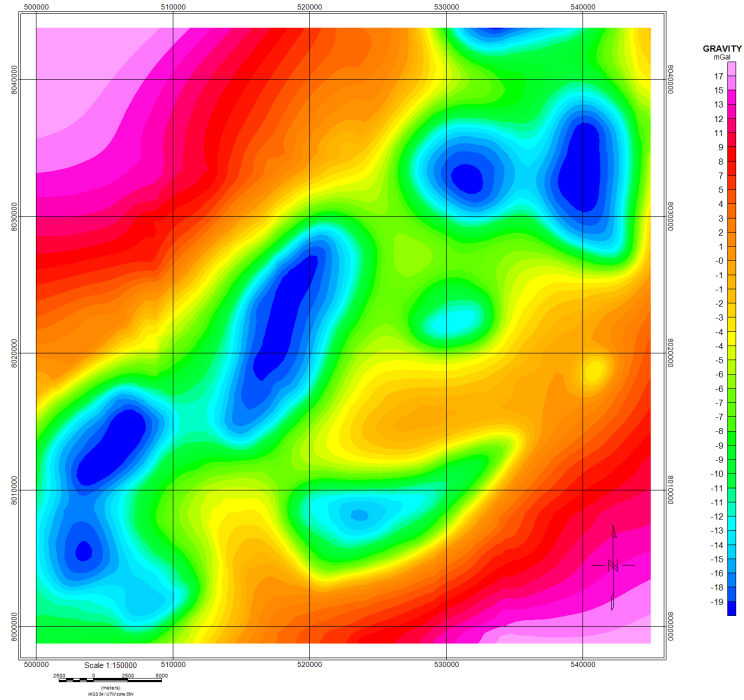


Figure 32. Gravity field data used for modeling.

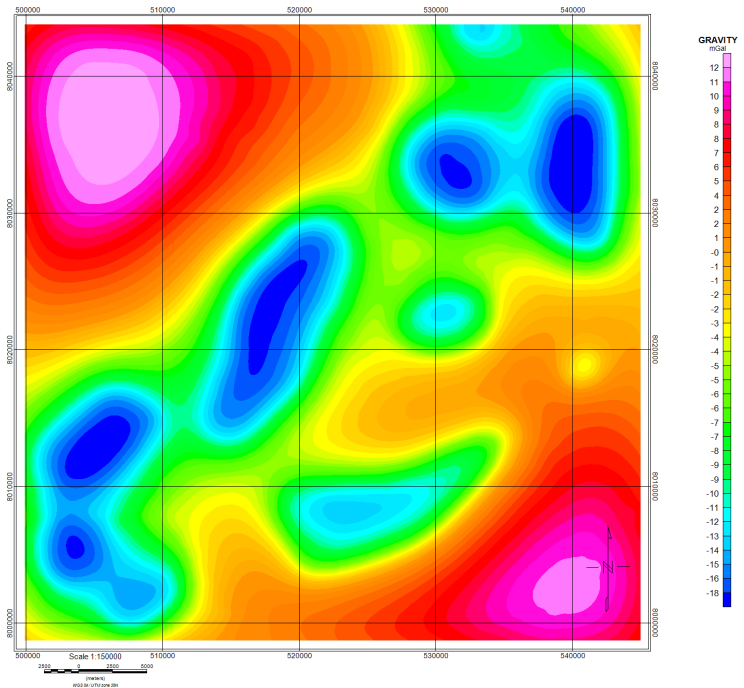


Figure 33. Gravity field model response.

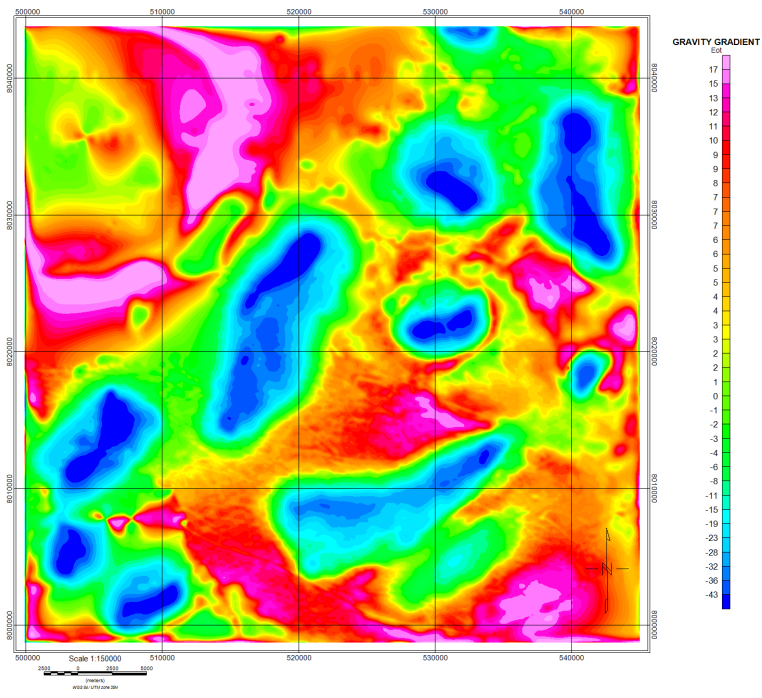


Figure 34. Vertical gravity gradient data used for modeling.

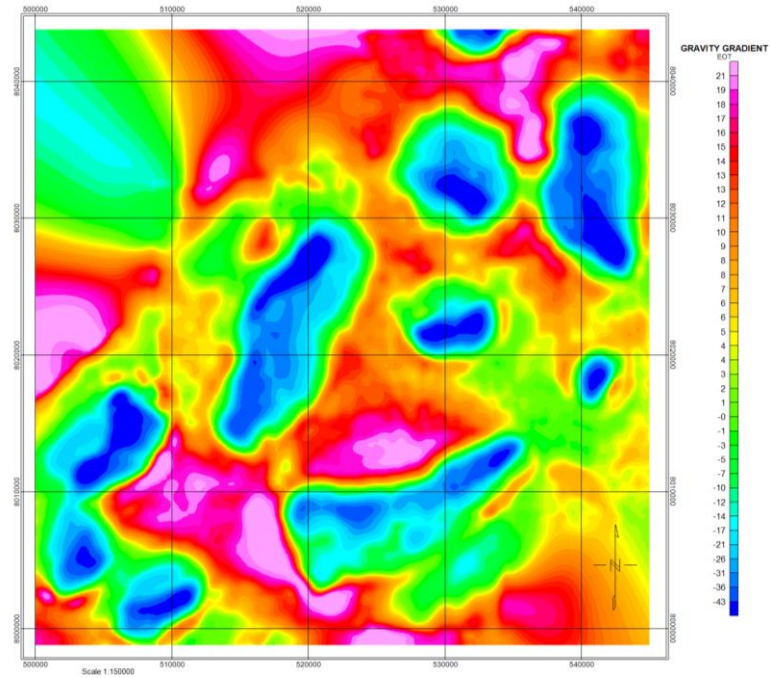


Figure 35. Vertical gravity gradient model response.

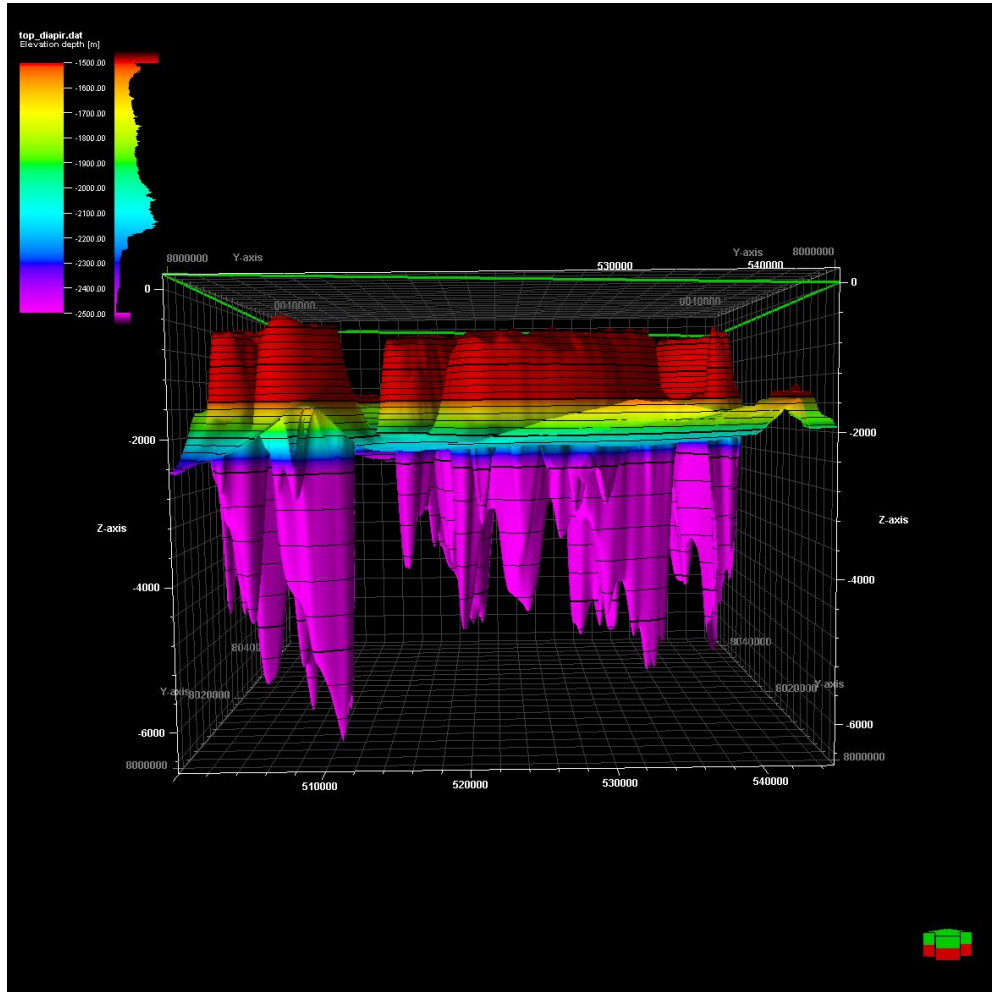


Figure 36. 3D salt model.

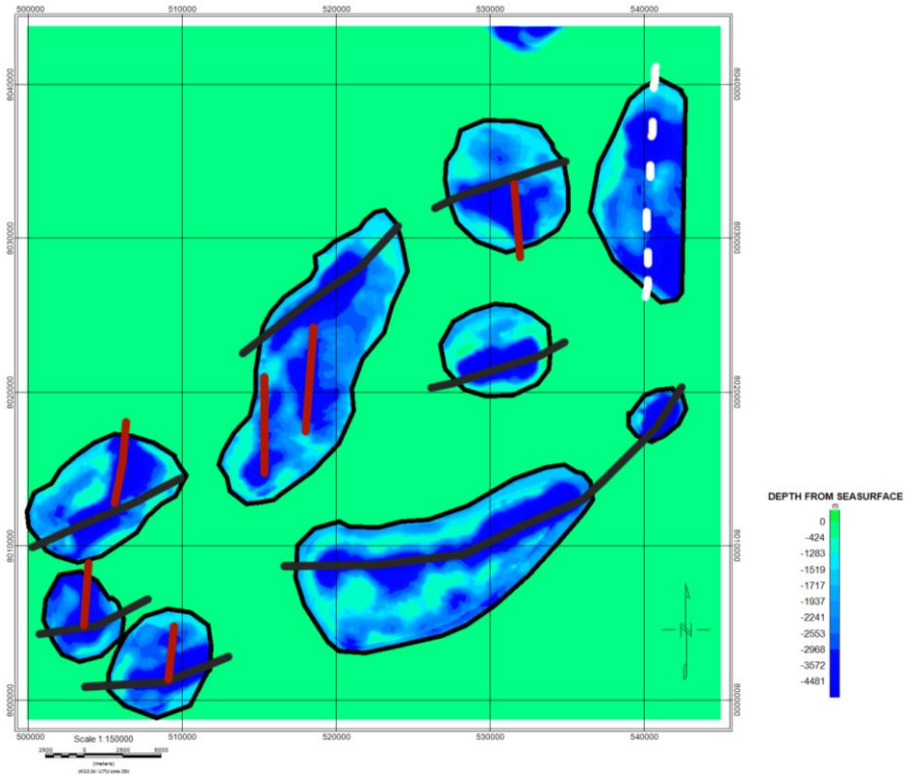


Figure 37. The base of the salt diapirs in planar view and trends in their distribution.

Cross section A-A'

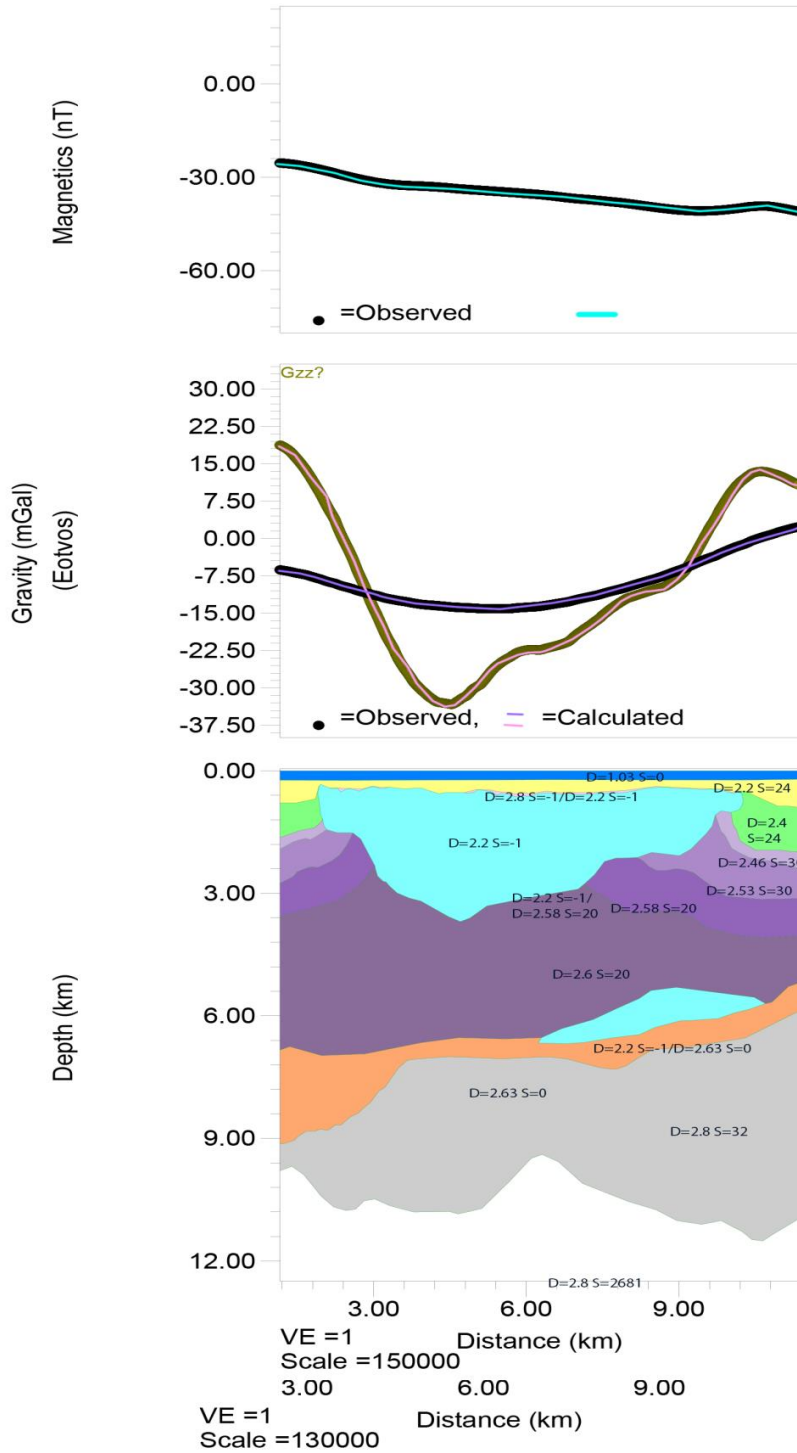


Figure 38. Cross Section A. D is density of layer and S is the magnetic susceptibility. See figure 9 for location.

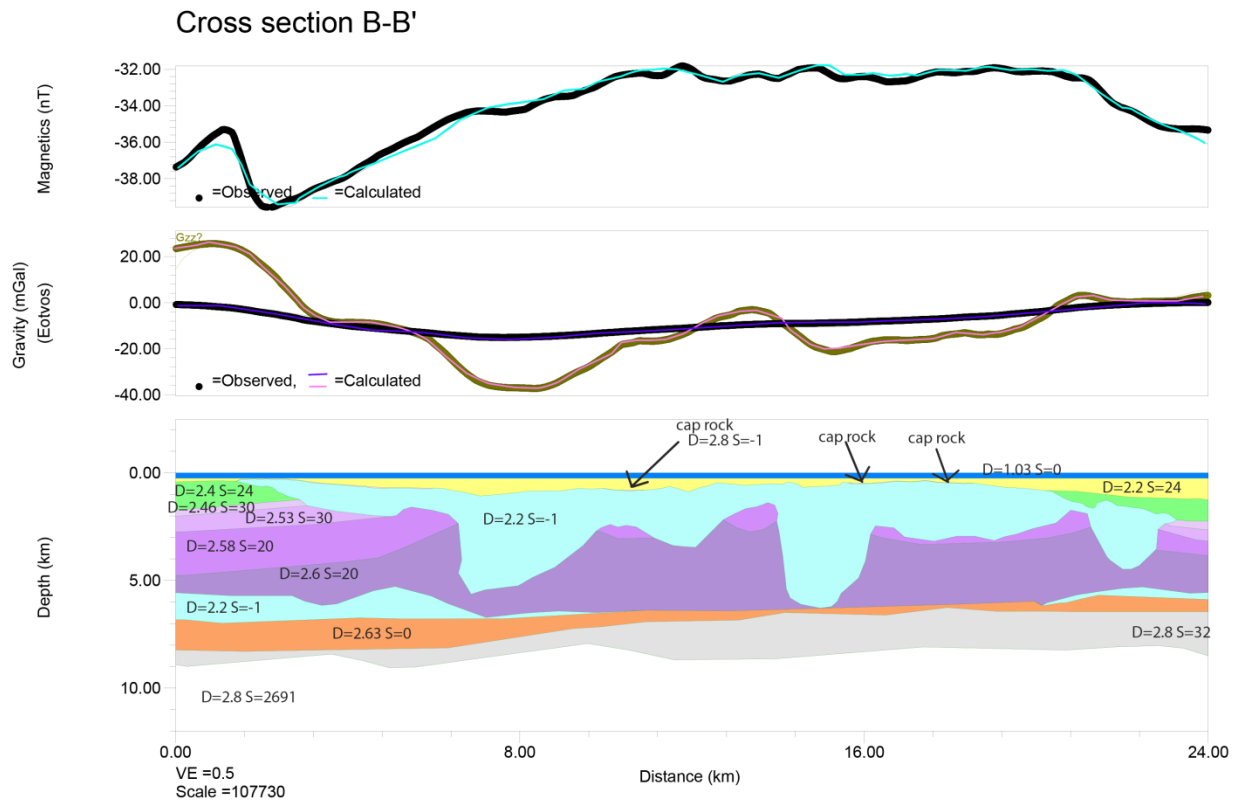


Figure 39. Cross Section B. D is the density of the layer, and S is the magnetic susceptibility. See figure 9 for location.

8 Conclusion

In this study, an integrated model for the salt geometry of a study area in the southern Nordkapp Basin has been created. By integrating data from well logs, core samples, reflection seismic and potential field data, a geological model over a large area of the southern Nordkapp Basin is generated. The modeling scheme is an iterative approach, where multiple steps have been conducted and repeated to stepwise improve the overall fit of the model to the potential field data. The modeled salt geometry gives improved constrain on salt geometry, where seismic interpretation is difficult.

The model gives new information about the initiation and evolution of the salt, as well as infers inherent grains from the tectono-stratigraphic evolution of the basin area. Because of the geological history of the Nordkapp Basin, with multiple episodes of uplift and erosion, the sediments of the basin are strongly compacted, and show high densities even for the upper layers. This provides an excellent setting for inversion modeling using potential field data as presented in this paper. The high sediment densities result in the absence of a Nil- zone and gives a large contrast between the sediments and the salt, which gives increased sensitivity of the gravity and gravity gradient data. The shallow salt also results in excellent sensitivity of the vertical gravity gradient to the base of the salt structures. Low positive magnetization of the sediments, compared to a small negative magnetization of salt and the higher magnetization of the basement, gives high sensitivity for magnetic data on the depth of the top salt horizon and the high magnetic basement.

Multiple theories regarding the initiation, evolution and inherent properties for the salt structures in the southern Nordkapp Basin exists. The model created in this thesis infer a scenario where the geometry and distribution of salt structures in the basin is controlled both by external processes like regional tectonics, and from basement faults and inherent basement weakness grain. The salt model show asymmetrical salt structures which are interpreted to be initiated by basement controlled faults, and the evolution of the diapirs controlled by tectonic activity. The salt model indicates the presence of both cap rock,

concentrated in depressions on the top of the salt structures, and mother salt, located in pedestals under the diapirs. The formation of the salt structures is interpreted to be triggered by basement-involved faults, where salt structures have developed along strike of these faults. Episodes of active growth of the diapirs are recorded in the salt geometry.

The highly unsymmetrical salt structures in the basin show two main structural orientations, a dominant NE-SW trend parallel to the basin margin, and a minor NNE-SSW. An interpretation is suggested where the NNE-SSW lineation represents an old basement wakens grain, which has been abandoned for the more dominant NE-SW trend post-Perm. This interpretation would explain some of the challenges with complex basement setting observed in the southern Nordkapp Basin area.

Further work would be required to support the theory of basement grain controlling lineations in salt structures. New processing of the seismic data using the derived salt model for an improved velocity model, could increase the sub-salt resolution sufficiently to be able to interpret basement faults and determine their lineation and proximity to the salt structures. A full basement study to map the basement faults would be necessary to further confirm or disprove the relation between salt structures, structure trends and basement faults.

The method presented for modeling the geometry of salt structures could be applicable to other salt provinces, provided sufficient sensitivity for the potential field data could be achieved. The method could help improve constrain on the current salt geometry which can be used to interpret the evolution of the salt.

References

- A. Murphy, C., Brewster, J., 2007. Target delineation using Full Tensor Gravity Gradiometry data. ASEG Extended Abstracts 2007, 1. doi:10.1071/ASEG2007ab096
- Alsop, G.I., 2012. Salt Tectonics, Sediments and Prospectivity. Geological Society of London.
- Bain, J.E., Horscroft, T.R., Weyand, J., Saad, A.H., Bulling, D.N., 1993. Complex salt features resolved by integrating seismic, gravity and magnetics. Presented at the 55th EAEG Meeting. doi:10.3997/2214-4609.201411696
- Barrère, C., Ebbing, J., Gernigon, L., 2009. Offshore prolongation of Caledonian structures and basement characterisation in the western Barents Sea from geophysical modelling. *Tectonophysics* 470, 71–88. doi:10.1016/j.tecto.2008.07.012
- Beltrao, J.F., Silva, J.B.C., Costa, J.C., 1991. Robust polynomial fitting method for regional gravity estimation. *Geophysics* 56, 80–89.
- Bergendahl, E., 1989, Halokinetisk utvikling av Nordkappbassengets sørvestre segmentm., Cand scient (candidatus scientiarum) Thesis., University of Oslo, Oslo 120.
- Blaich, O.A., Tsikalas, F., Faleide, J.I., 2017. New insights into the tectono-stratigraphic evolution of the southern Stappen High and its transition to Bjørnøya Basin, SW Barents Sea. *Marine and Petroleum Geology* 85, 89–105. doi:10.1016/j.marpetgeo.2017.04.015
- Bhattacharyya, B., 1966. Continuous spectrum of the total-magnetic-field anomaly due to a rectangular prismatic body. *GEOPHYSICS* 31, 97–121. doi:10.1190/1.1439767
- Bugge, T., Elvebakk, G., Fanavoll, S., Mangerud, G., Smelror, M., Weiss, H.M., Gjelberg, J., Kristensen, S.E., Nilsen, K. are, 2002. Shallow stratigraphic drilling applied in hydrocarbon exploration of the Nordkapp Basin, Barents Sea. *Marine and Petroleum Geology* 19, 13–37.
- Bugge, T., Fanavoll, S., 1995. The Svalis Dome, Barents Sea - a geological playground for shallow stratigraphic drilling. *First Break* 13, 237–251. doi:10.3997/1365-2397.1995012
- Campbell, W.H., 2003. Introduction to geomagnetic fields, 2nd. ed. ed. Cambridge University Press, Cambridge ; New York.
- Childs, C., Easton, S.J., Vendeville, B.C., Jackson, M.P.A., Lin, S.T., Walsh, J.J., Watterson, J., 1993. Kinematic analysis of faults in a physical model of growth faulting above a viscous salt analogue. *Tectonophysics* 228, 313–329. doi:10.1016/0040-1951(93)90346-L

- Chowdhury, A., 2010. Salt geology and hydrocarbon plays in the northeastern Gulf of Mexico. *First Break* 28.
- Colombo, D., McNeice, G., Raterman, N., Zinger, M., Rovetta, D., Curiel, E.S., 2014. Exploration beyond seismic: The role of electromagnetics and gravity gradiometry in deep water subsalt plays of the Red Sea. *Interpretation* 2, SH33-SH53.
doi:10.1190/INT-2013-0149.1
- Cordell, L., Zorin, Y.A., Keller, G.R., 1991. The decompensative gravity anomaly and deep structure of the region of the Rio Grande Rift. *J. Geophys. Res.* 96, 6557–6568.
doi:10.1029/91JB00008
- Courtillot, V., Besse, J., 1987. Magnetic Field Reversals, Polar Wander, and Core-Mantle Coupling. *Science* 237, 1140–1147. doi:10.1126/science.237.4819.1140
- Davis, D.M., Engelder, T., 1985. The role of salt in fold-and-thrust belts. *Tectonophysics, Collision Tectonics: Deformation of Continental Lithosphere* 119, 67–88.
doi:10.1016/0040-1951(85)90033-2
- Dell'Aversana, P., 2014. From rock physics to geophysical data integration: theory, applications and implications. *First Break* 32.
- Dengo, C. A., and K. G. Røssland, 1992, Extensional tectonic history of the western Barents Sea, in R. M. Larsen et al., eds., *Structural and tectonic modelling and its application to petroleum geology: Norwegian Petroleum Society Special Publication*, p. 91–107.
- Doré, A.G., 1995. Barents Sea Geology, Petroleum Resources and Commercial Potential. *Arctic* 48, 207–221.
- Dore, A. G., 1991, The structural foundation and evolution of Mesozoic seaways between Europe and Arctic: *Paleogeography, Paleoclimatology, Paleoecology*, v. 87, p. 441–492.
- Elvebakk, G., Hunt, D.W., Stemmerik, L., 2002. From isolated buildups to buildup mosaics: 3D seismic sheds new light on upper Carboniferous–Permian fault controlled carbonate buildups, Norwegian Barents Sea. *Sedimentary Geology* 152, 7–17.
doi:10.1016/S0037-0738(02)00232-4
- Faleide, J.I., Bjørlykke, K., Gabrielsen, R.H., 2015. Geology of the Norwegian Continental Shelf, in: Bjørlykke, K. (Ed.), *Petroleum Geoscience*. Springer Berlin Heidelberg, pp. 603–637.
- Faleide, J.I., Gudlaugsson, S.T., Jacquart, G., 1984. Evolution of the western Barents Sea. *Marine and Petroleum Geology* 1, 123–150. doi:10.1016/0264-8172(84)90082-5

- Faleide, J.I., Vågnes, E., Gudlaugsson, S.T., 1993. Late Mesozoic-Cenozoic evolution of the southwestern Barents Sea in a regional rift-shear tectonic setting. *Marine and Petroleum Geology* 10, 186–214. doi:10.1016/0264-8172(93)90104-Z
- Fossen, H., 2010. *Structural Geology*, 1 edition. ed. Cambridge University Press, Cambridge ; New York.
- Gabrielsen, R.H., Fæseth, Jensen, 1990a. NPD_BulletinNr6.pdf. NPD buletin.
- Gabrielsen, R.H., Kløvjan, O.S., Rasmussen, A., Støland, T., 1990b. Interaction between halokinesis and faulting: Structuring of the margin of the Nordkapp Basin, Barents Sea Region, in: *Structural and Tectonic Modelling and Its Application to Petroleum Geology*, Norwegian Petroleum Society.
- Garland, G.D., 2016. *The Earth's Shape and Gravity: The Commonwealth and International Library: Geophysics Division*. Elsevier.
- Gee, D.G., Bogolepova, O.K., Lorenz, H., 2006. The Timanide, Caledonide and Uralide orogens in the Eurasian high Arctic, and relationships to the palaeo-continent Laurentia, Baltica and Siberia. *Geological Society, London, Memoirs* 32, 507–520. doi:10.1144/GSL.MEM.2006.032.01.31
- Gernigon, L., Brönnner, M., 2012. Late Palaeozoic architecture and evolution of the southwestern Barents Sea: insights from a new generation of aeromagnetic data. *Journal of the Geological Society* 169, 449–459. doi:10.1144/0016-76492011-131
- Gernigon, L., Brönnner, M., Fichler, C., Løvås, L., Marelllo, L., Olesen, O., 2011. Magnetic expression of salt diapir–related structures in the Nordkapp Basin, western Barents Sea. *Geology* 39, 135–138.
- Gernigon, L., Brönnner, M., Roberts, D., Olesen, O., Nasuti, A., Yamasaki, T., 2014. Crustal and basin evolution of the southwestern Barents Sea: From Caledonian orogeny to continental break-up. *Tectonics* 33, 2013TC003439. doi:10.1002/2013TC003439
- Getting Started #6 - Salt Tectonics: A Compendium of Influential Papers [WWW Document], n.d. . AAPG. URL <http://www.aapg.org/publications/special-publications/cds/details/articleid/3478/getting-started-6-salt-tectonics-a-compendium-of-influential-papers> (accessed 12.15.16).
- Glørstad-Clark, E., Birkeland, E.P., Nystuen, J.P., Faleide, J.I., Midtkandal, I., 2011. Triassic platform-margin deltas in the western Barents Sea. *Marine and Petroleum Geology* 28, 1294–1314. doi:10.1016/j.marpetgeo.2011.03.006
- Glørstad-Clark, E., Faleide, J.I., Lundschieen, B.A., Nystuen, J.P., 2010. Triassic seismic sequence stratigraphy and paleogeography of the western Barents Sea area. *Marine and Petroleum Geology* 27, 1448–1475. doi:10.1016/j.marpetgeo.2010.02.008

- GM-SYS 3D Modelling [WWW Document], n.d. URL <http://www.geosoft.com/products/gm-sys/gm-sys-3d-modelling> (accessed 12.15.16).
- Gudlaugsson, S.T., Faleide, J.I., Johansen, S.E., Breivik, A.J., 1998. Late Palaeozoic structural development of the Southwestern Barents Sea. *Marine and Petroleum Geology* 15, 73–102. doi:10.1016/S0264-8172(97)00048-2
- Hamdi-Nasr, I., Hédi Inoubli, M., Ben Salem, A., Tlig, S., Mansouri, A., 2009. Gravity contributions to the understanding of salt tectonics from the Jebel Cheid area (dome zone, Northern Tunisia). *Geophysical Prospecting* 57, 719–728. doi:10.1111/j.1365-2478.2009.00788.x
- Hinze, W.J., Frese, R.R.B. von, Saad, A.H., 2013. *Gravity and Magnetic Exploration: Principles, Practices, and Applications*. Cambridge University Press.
- Hudec, M.R., Jackson, M.P.A., 2007. Terra infirma: Understanding salt tectonics. *Earth-Science Reviews* 82, 1–28. doi:10.1016/j.earscirev.2007.01.001
- Hudec, M.R., Jackson, M.P.A., 2006. Advance of allochthonous salt sheets in passive margins and orogens. *AAPG Bulletin* 90, 1535–1564. doi:10.1306/05080605143
- Jackson, C.A.-L., Lewis, M.M., 2016. Structural style and evolution of a salt-influenced rift basin margin; the impact of variations in salt composition and the role of polyphase extension. *Basin Research* 28, 81–102. doi:10.1111/bre.12099
- Jackson, M.P.A., 1995. Retrospective Salt Tectonics. *Salt tectonics: a global perspective: AAPG memoir 65* 1–28.
- Jensen and Sørensen, 1992, Extensional tectonic history of the western Barents Sea, in R. M. Larsen et al., eds., *Structural and tectonic modelling and its application to petroleum geology: Norwegian Petroleum Society Special Publication*, p. 91–107.
- Jenyon, M.K., 1986. *Salt Tectonics*, 1986 edition. ed. Springer, London ; New York : New York, NY, USA.
- Koyi, H., 1998. The shaping of salt diapirs. *Journal of Structural Geology* 20, 321–338. doi:10.1016/S0191-8141(97)00092-8
- Koyi, H., Jenyon, M.K., Petersen, K., 1993a. The effect of basement faulting on diapirism. *Journal of Petroleum geology* 16, 285–312.
- Koyi, H., Talbot, C.J., Torudbakken, B.O., 1995. Analogue models of salt diapirs and seismic interpretation in the Nordkapp Basin, Norway. *Petroleum geoscience* 1, 185–192.
- Koyi, H., Talbot, C.J., Tørudbakken, B.O., 1993b. Salt diapirs of the southwest Nordkapp Basin: analogue modelling. *Tectonophysics* 228, 167–187.

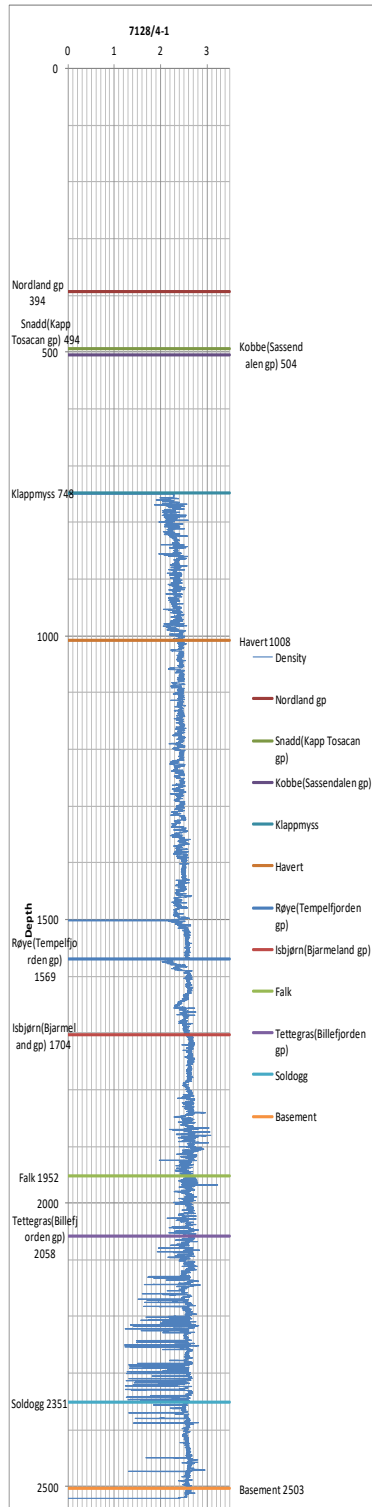
- Larsen, R.M., Brekke, H., Larsen, B.T., Talleraas, E., 2013. Structural and Tectonic Modelling and its Application to Petroleum Geology: Proceedings of Norwegian Petroleum Society Workshop, 18-20 October 1989, Stavanger, Norway. Elsevier.
- Leveille, J.P., Jones, I.F., Zhou, Z.-Z., Wang, B., Liu, F., 2011. Subsalt imaging for exploration, production, and development: A review. *GEOPHYSICS* 76, WB3-WB20. doi:10.1190/geo2011-0156.1
- Libak, A., Mjelde, R., Keers, H., Faleide, J.I., Murai, Y., 2012. An integrated geophysical study of Vestbakken Volcanic Province, western Barents Sea continental margin, and adjacent oceanic crust. *Marine Geophysical Research* 33, 185–207. doi:10.1007/s11001-012-9155-3
- Macmillan, S., Maus, S., 2005. International Geomagnetic Reference Field—the tenth generation. *Earth Planet Sp* 57, 1135–1140. doi:10.1186/BF03351896
- Magnetic North, Geomagnetic and Magnetic Poles [WWW Document], n.d. URL <http://wdc.kugi.kyoto-u.ac.jp/poles/polesexp.html> (accessed 12.19.16).
- Malin, K., 2016. Integrated geophysical models.pdf.
- Mohriak, W.U., Macedo, J.M., Castellani, R.T., Rangel, H.D., Barros, A.Z.N., Latgé, M.A.L., Mizusaki, A.M.P., Szatmari, P., Demercian, L.S., Rizzo, J.G., others, 1995. Salt tectonics and structural styles in the deep-water province of the Cabo Frio region, Rio de Janeiro, Brazil.
- Murray, C.G., Scheibner, E., Walker, R.N., 1989. Regional geological interpretation of a digital coloured residual Bouguer gravity image of eastern Australia with a wavelength cut-off of 250 km. *Australian Journal of Earth Sciences* 36, 423–449. doi:10.1080/08120098908729498
- Murphy, C.A., 2010. Recent developments with Air-FTG®.
- Murphy, C.A., Dickinson, J.L., 2009. Exploring exploration play models with FTG gravity data, in: 11th SAGA Biennial Technical Meeting and Exhibition.
- Murphy, Brewster, Robinson, 2007. Evaluating Air-FTG® survey data: bringing value to the full picture.
- Mørk, McEnroe, Olesen, 1996. OSRAM –Origin of Sediment-related AeroMagnetics.
- Nabighian, M.N., Ander, M.E., Grauch, V.J.S., Hansen, R.O., LaFehr, T.R., Li, Y., Pearson, W.C., Peirce, J.W., Phillips, J.D., Ruder, M.E., 2005a. Historical development of the gravity method in exploration. *GEOPHYSICS* 70, 63ND–89ND. doi:10.1190/1.2133785
- Nabighian, M.N., Grauch, V.J.S., Hansen, R.O., LaFehr, T.R., Li, Y., Peirce, J.W., Phillips, J.D., Ruder, M.E., 2005b. The historical development of the magnetic method in exploration. *GEOPHYSICS* 70, 33ND–61ND. doi:10.1190/1.2133784

- Nettleton, L.L., 1971. *Elementary Gravity and Magnetism for Geologists and Seismologists*.
- Nilsen, K.T., Vendeville, B.C., Johansen, J.-T., 1995. Influence of regional tectonics on halokinesis in the Nordkapp Basin, Barents Sea.
- NPD, 2016. Wellbore exploration history Well 7227/10-1.
- O'Brien, Rodriguez, Sixta, 2015. Resolving the K-2 salt structure in the gulf of Mexico.pdf. *Leading Edge* April.
- Olesen, O., Brønner, M., Ebbing, J., Gellein, J., Gernigon, L., Koziel, J., Lauritsen, T., Myklebust, R., Pascal, C., Sand, M., Solheim, D., Usov, S., 2010. New aeromagnetic and gravity compilations from Norway and adjacent areas: methods and applications, in: *Petroleum Geology: From Mature Basins to New Frontiers—Proceedings of the 7th Petroleum Geology Conference*. Geological Society of London, pp. 559–586.
- Parker R. L. 1972. The rapid calculation of potential anomalies. *Journal of the Royal Astronomical Society* 31, 447-455.
- Ramberg, I.B., 2008. *The Making of a Land: Geology of Norway*. Geological Society of London.
- Rønnevik, H., Jacobsen, H.-P., 1984. Structural highs and basins in the western Barents Sea, in: Spencer, A.M. (Ed.), *Petroleum Geology of the North European Margin*. Springer Netherlands, pp. 19–32.
- Rowan, M.G., Lawton, T.F., Giles, K.A., Ratliff, R.A., 2003. Near-salt deformation in La Popa basin, Mexico, and the northern Gulf of Mexico: A general model for passive diapirism. *AAPG Bulletin* 87, 733–756. doi:10.1306/01150302012
- Rowan, M.G., Peel, F.J., Vendeville, B.C., 2004. Gravity-driven Fold Belts on Passive Margins 157–182.
- Smelror, M., Basov, V.A., *Norges Geologiske Undersøkelse*, 2009. *Atlas: geological history of the Barents Sea*. Geological Survey of Norway, Trondheim.
- Smith, W., Wessel, P., 1990. Gridding with continuous curvature splines in tension. *GEOPHYSICS* 55, 293–305. doi:10.1190/1.1442837
- Snedden, J.W., American Association of Petroleum Geologists, AAPG/Datapages (Firm), 2006. *Getting started in salt tectonics*. AAPG/Datapages, Tulsa, OK.
- Stadtler, C., Fichler, C., Hokstad, K., Myrlund, E.A., Wienecke, S., Fotland, B., 2014. Improved salt imaging in a basin context by high resolution potential field data: Nordkapp Basin, Barents Sea: Salt imaging in Nordkapp Basin. *Geophysical Prospecting* 62, 615–630. doi:10.1111/1365-2478.12101

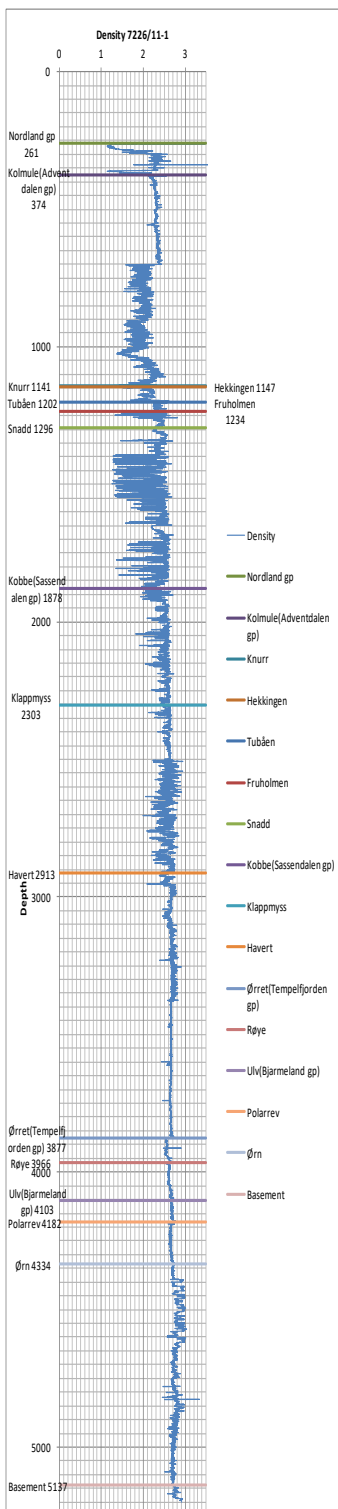
- Stewart, S.A., Clark, J.A., 1999. Impact of salt on the structure of the Central North Sea hydrocarbon fairways. *Petroleum Geology Conference series 5*, 179–200.
doi:10.1144/0050179
- Thébault, E., Finlay, C.C., Beggan, C.D., Alken, P., Aubert, J., Barrois, O., Bertrand, F., Bondar, T., Boness, A., Brocco, L., Canet, E., Chambodut, A., Chulliat, A., Coïsson, P., Civet, F., Du, A., Fournier, A., Fratter, I., Gillet, N., Hamilton, B., Hamoudi, M., Hulot, G., Jager, T., Korte, M., Kuang, W., Lalanne, X., Langlais, B., Léger, J.-M., Lesur, V., Lowes, F.J., Macmillan, S., Mande, M., Manoj, C., Maus, S., Olsen, N., Petrov, V., Ridley, V., Rother, M., Sabaka, T.J., Saturnino, D., Schachtschneider, R., Sirol, O., Tangborn, A., Thomson, A., Tøffner-Clausen, L., Vigneron, P., Wardinski, I., Zvereva, T., 2015. International Geomagnetic Reference Field: the 12th generation. *Earth, Planets and Space* 67. doi:10.1186/s40623-015-0228-9
- Trusheim, F., 1960. Mechanism of salt migration in northern Germany. *AAPG Bulletin* 44, 1519–1540.
- Vendeville, B.C., 2002. Mechanism of Salt Migration in Northern Germany.
- Vendeville, B.C., Jackson, M.P.A., 1992. The rise of diapirs during thin-skinned extension. *Marine and Petroleum Geology* 9, 331–354. doi:10.1016/0264-8172(92)90047-I
- Vendeville, B.C., Nilsen, K.T., 1995. Episodic growth of salt diapirs driven by horizontal shortening., in: ResearchGate. Presented at the 16th Annual Research Conference, pp. 285–295.
- Walker, C.W., 1976. Origin of Gulf Coast Salt-Dome Cap Rock: GEOLOGIC NOTES. *AAPG Bulletin* 60, 2162–2166.
- WDC for Geomagnetism, Kyoto [WWW Document], n.d. URL <http://wdc.kugi.kyoto-u.ac.jp/index.html> (accessed 12.19.16).
- Worsley, D., 2008. The post-Caledonian development of Svalbard and the western Barents Sea. *Polar Research* 27, 298–317. doi:10.1111/j.1751-8369.2008.00085.x

Appendix A: Well logs and density gradients

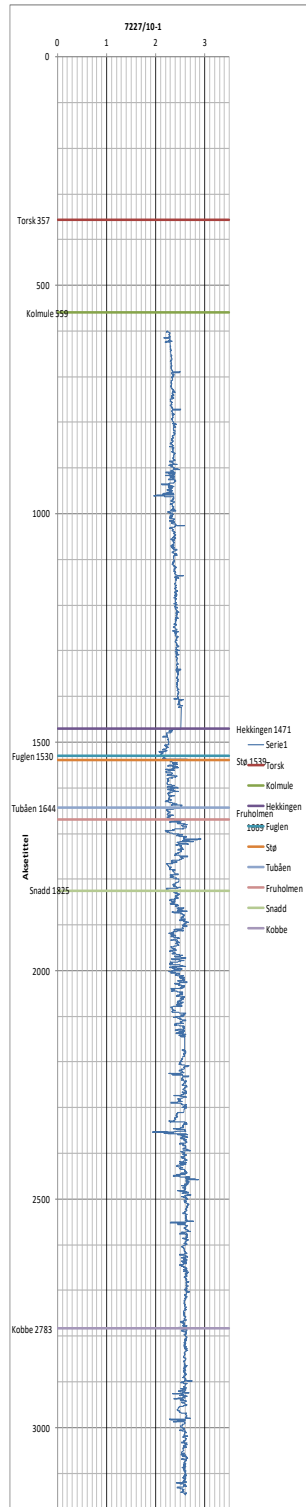
Well 7128/4-1



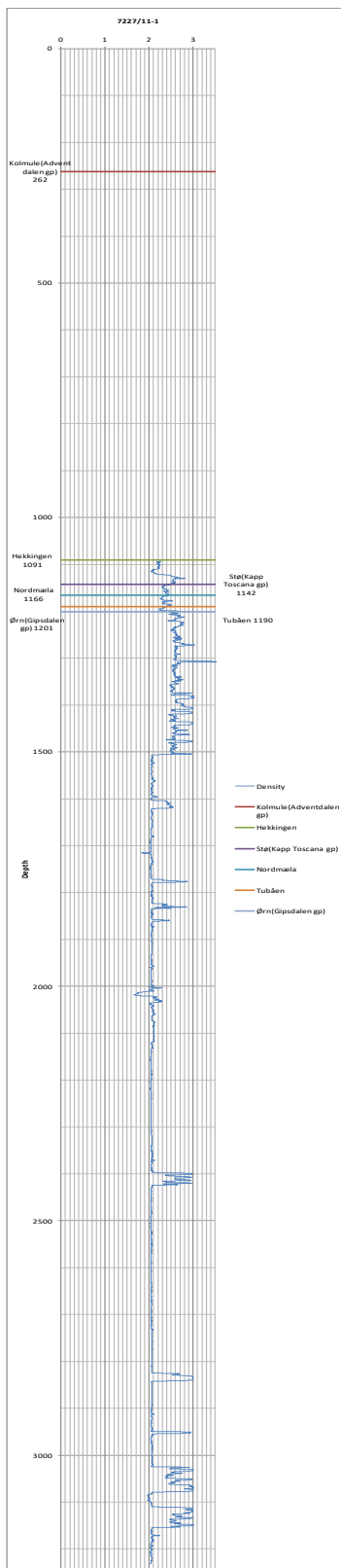
Well 7226/11-1



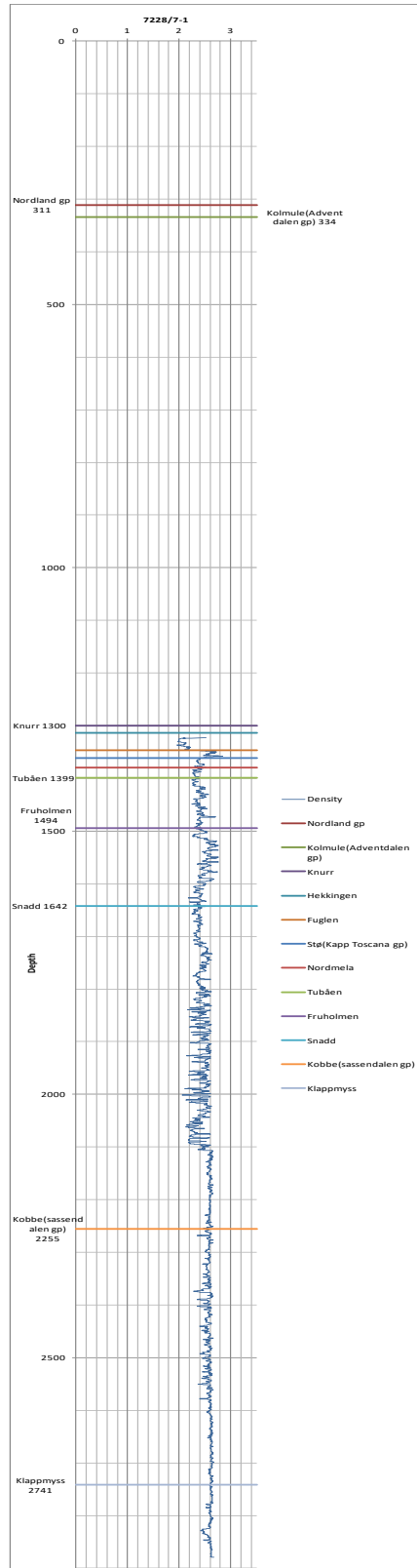
Well 7227/10-1



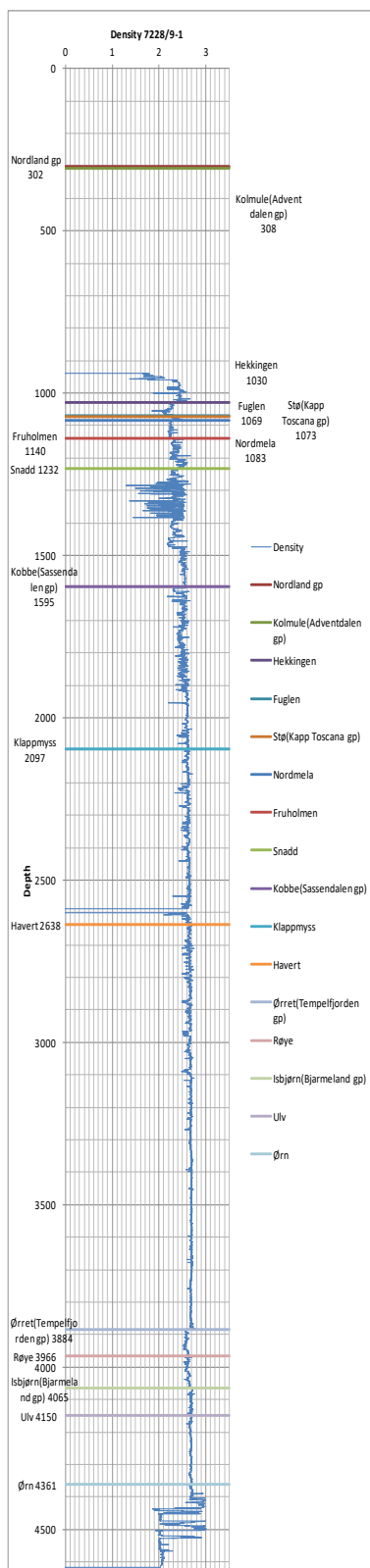
Well 7227/11-1



Well 7228/7-1



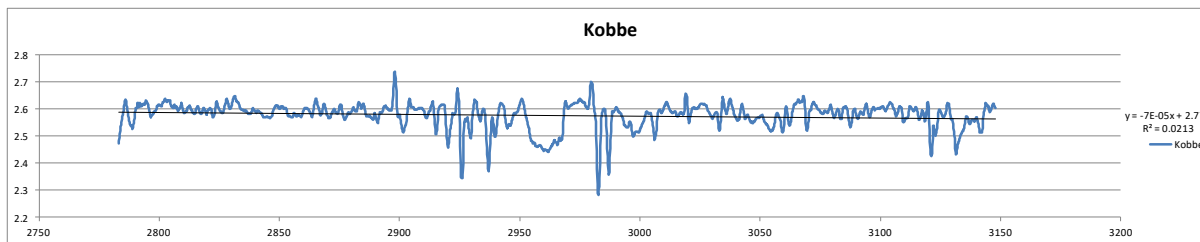
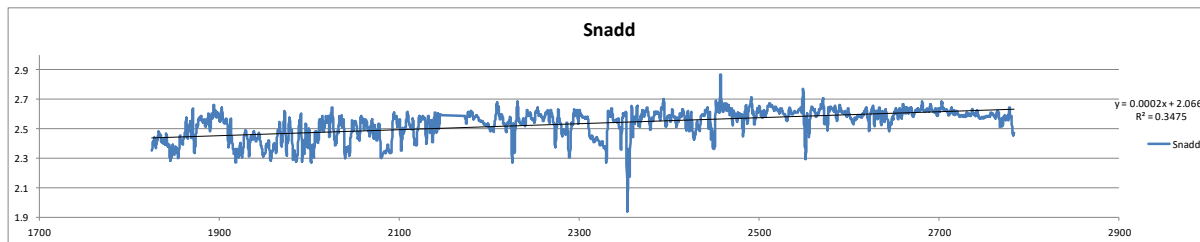
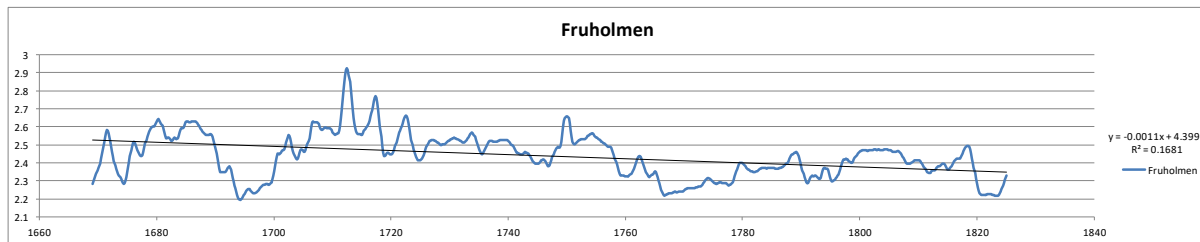
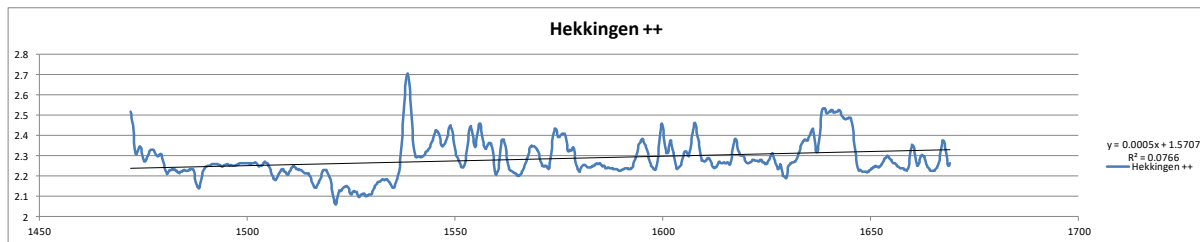
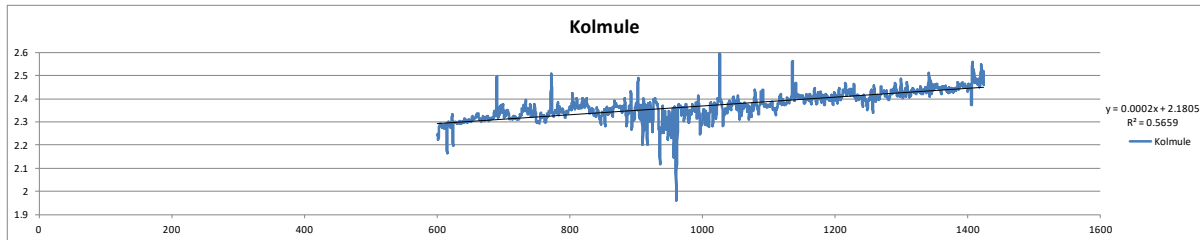
Well 7228/9-1



Appendix B: Density trends.

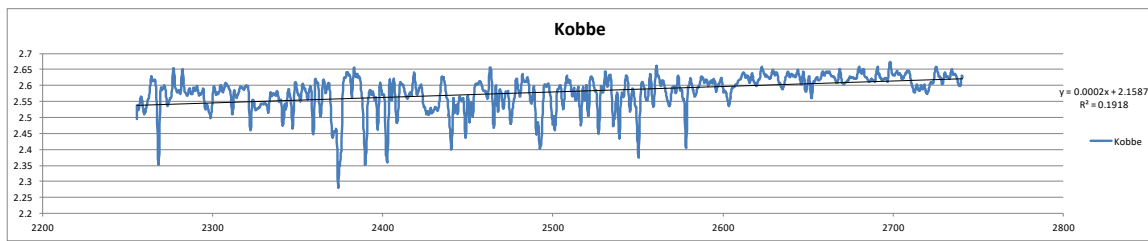
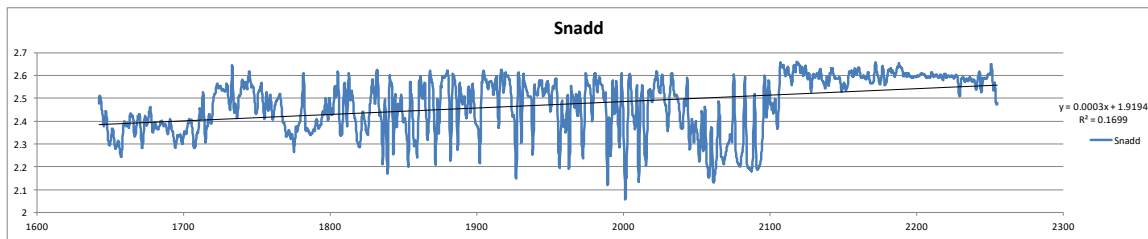
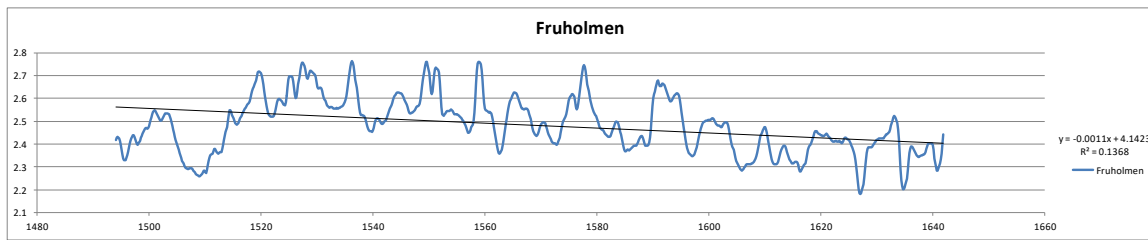
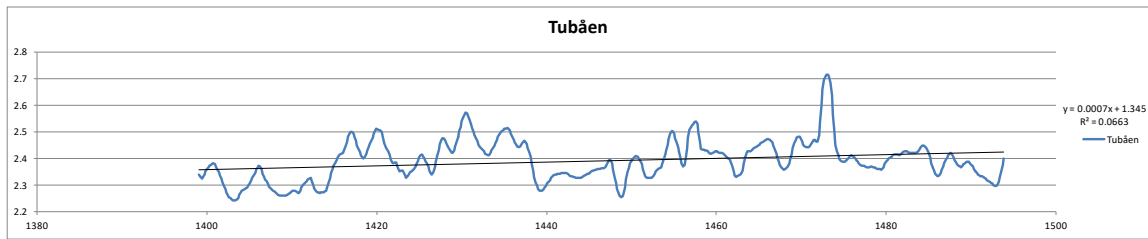
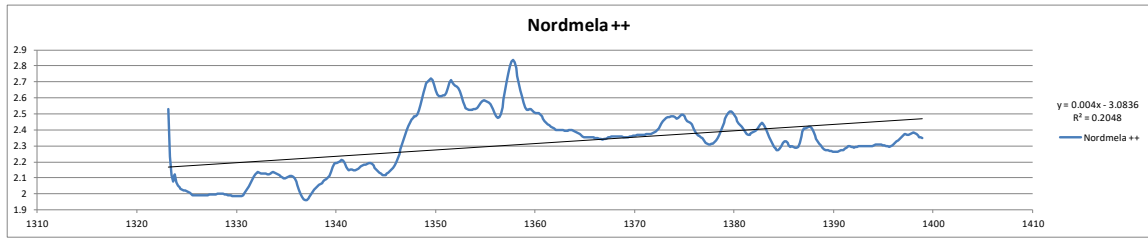
Density gradients calculated from well 7227/10-1.

Black line indicates gradient. Gradient and R²-value indicated to the right of each plot.



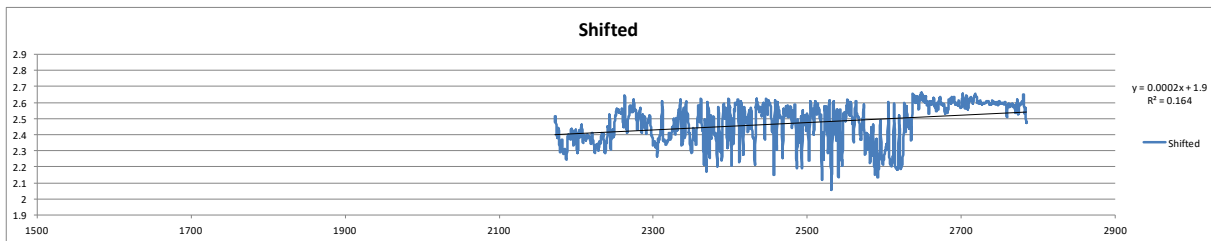
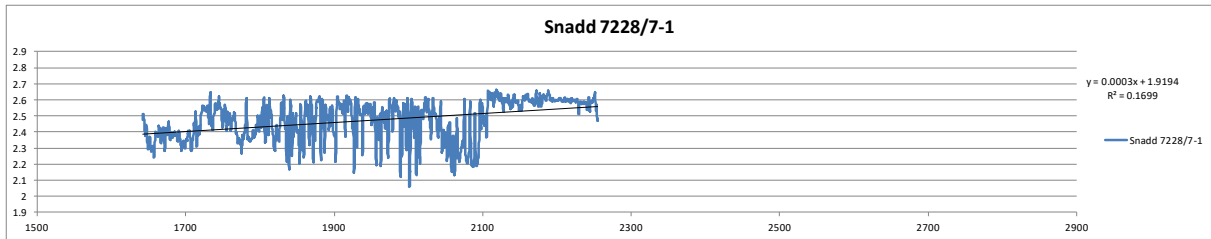
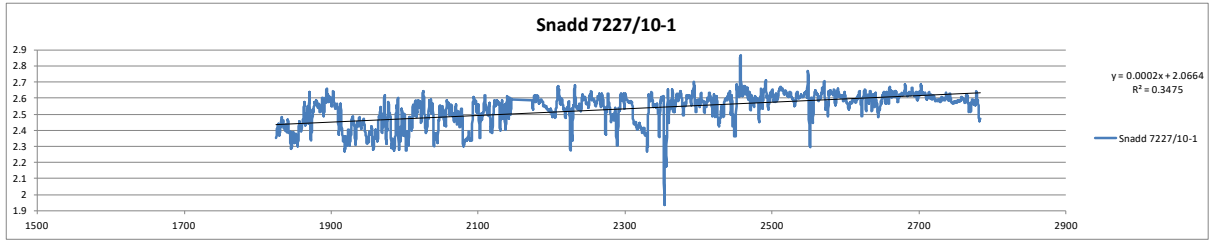
Density gradients calculated from well 7228/7-1.

Black line indicates gradient. Gradient and R2-value indicated to the right of each plot.



Density gradients for the Snadd formation indicating best-fit gradients.

The lower plot shows the fit of the gradient if the data is shifted down by 500m.



Appendix C: Check shot from well 7228/7-1

MD	TWT	Average velocity	Interval velocity
871.00	851.60	1980.74	2880.00
882.00	859.10	1988.59	2918.92
893.00	866.50	1996.54	2906.67
904.00	874.00	2004.35	2602.41
915.00	882.30	2009.97	2511.63
926.00	890.90	2014.82	2658.54
937.00	899.10	2020.69	2805.19
948.00	906.80	2027.35	2634.15
959.00	915.00	2032.79	2511.63
970.00	923.60	2037.25	2400.00
981.00	932.60	2040.75	2842.11
992.00	940.20	2047.22	2842.11
1003.00	947.80	2053.60	2517.65
1014.00	956.30	2057.72	2805.19
1025.00	964.00	2063.69	2842.11
1036.00	971.60	2069.78	2891.89
1047.00	979.00	2076.00	2891.89
1058.00	986.40	2082.12	2891.89
1069.00	993.80	2088.15	2931.51

1080.00	1001.10	2094.30	3057.14
1091.00	1008.10	2100.98	3101.45
1102.00	1015.00	2107.78	3117.65
1113.00	1021.80	2114.50	3194.03
1124.00	1028.50	2121.54	3164.18
1135.00	1035.20	2128.28	3164.18
1146.00	1041.90	2134.95	3134.33
1157.00	1048.60	2141.33	3230.77
1168.00	1055.10	2148.04	3164.18
1179.00	1061.80	2154.45	3134.33
1190.00	1068.50	2160.60	3043.48
1201.00	1075.40	2166.26	3230.77
1212.00	1081.90	2172.66	3230.77
1223.00	1088.40	2178.98	3212.12
1234.00	1095.00	2185.21	3134.33
1245.00	1101.70	2190.98	3181.82
1256.00	1108.30	2196.88	3088.24
1267.00	1115.10	2202.31	3212.12
1278.00	1121.70	2208.26	2876.71
1289.00	1129.00	2212.58	2625.00
1300.00	1137.00	2215.48	2607.59
1311.00	1144.90	2218.18	2632.91
1322.00	1152.80	2221.03	2625.00

1333.00	1160.80	2223.81	2810.81
1344.00	1168.20	2227.53	2916.67
1355.00	1175.40	2231.75	3164.18
1366.00	1182.10	2237.04	3627.12
1377.00	1188.00	2243.94	3323.08
1388.00	1194.50	2249.81	3627.12
1399.00	1200.40	2256.58	3758.62
1410.00	1206.20	2263.80	3573.77
1421.00	1212.30	2270.40	3460.32
1432.00	1218.60	2276.55	3694.92
1443.00	1224.50	2283.38	3824.56
1454.00	1230.20	2290.52	4313.73
1465.00	1235.30	2298.87	3694.92
1476.00	1241.20	2305.51	3928.57
1487.00	1246.80	2312.80	3824.56
1498.00	1252.50	2319.68	4037.04
1509.00	1257.90	2327.05	3666.67
1520.00	1263.90	2333.41	3573.77
1531.00	1270.00	2339.37	3606.56
1542.00	1276.10	2345.43	4000.00
1553.00	1281.60	2352.53	3694.92
1564.00	1287.50	2358.68	3492.06
1575.00	1293.80	2364.20	3406.25

1586.00	1300.20	2369.33	3283.58
1597.00	1306.90	2374.01	3114.29
1608.00	1313.90	2377.96	3384.62
1619.00	1320.40	2382.91	3492.06
1630.00	1326.70	2388.18	3758.62
1641.00	1332.50	2394.15	3666.67
1652.00	1338.50	2399.85	3892.86
1663.00	1344.10	2406.07	4150.94
1674.00	1349.40	2412.92	4074.07
1685.00	1354.80	2419.55	3516.13
1696.00	1361.00	2424.54	3283.58
1707.00	1367.70	2428.75	3283.58
1718.00	1374.40	2432.92	3606.56
1729.00	1380.50	2438.10	3283.58
1740.00	1387.20	2442.19	3235.29
1751.00	1394.00	2446.05	3606.56
1762.00	1400.10	2451.11	3928.57
1773.00	1405.70	2457.00	3928.57
1784.00	1411.30	2462.84	3728.81
1795.00	1417.20	2468.11	3606.56
1806.00	1423.30	2472.99	3728.81
1817.00	1429.20	2478.17	3548.39
1828.00	1435.40	2482.79	3384.62

1839.00	1441.90	2486.86	3188.41
1850.00	1448.80	2490.20	3098.59
1861.00	1455.90	2493.17	3235.29
1872.00	1462.70	2496.62	3492.06
1883.00	1469.00	2500.88	3492.06
1894.00	1475.30	2505.12	3492.06
1905.00	1481.60	2509.31	3606.56
1916.00	1487.70	2513.81	3606.56
1927.00	1493.80	2518.28	3666.67
1938.00	1499.80	2522.87	3928.57
1949.00	1505.40	2528.10	3384.62
1960.00	1511.90	2531.78	3606.56
1971.00	1518.00	2536.10	3728.81
1982.00	1523.90	2540.72	3437.50
1993.00	1530.30	2544.47	4000.00
2004.00	1535.80	2549.68	3606.56
2015.00	1541.90	2553.86	3492.06
2026.00	1548.20	2557.68	3606.56
2037.00	1554.30	2561.80	3333.33
2048.00	1560.90	2565.06	3437.50
2059.00	1567.30	2568.62	3437.50
2070.00	1573.70	2572.15	3098.59
2081.00	1580.80	2574.52	3728.81

2092.00	1586.70	2578.81	3384.62
2103.00	1593.20	2582.10	3793.10
2114.00	1599.00	2586.49	3793.10
2125.00	1604.80	2590.85	4000.00
2136.00	1610.30	2595.67	3928.57
2147.00	1615.90	2600.28	4000.00
2158.00	1621.40	2605.03	3793.10
2169.00	1627.20	2609.27	4000.00
2180.00	1632.70	2613.95	3606.56
2191.00	1638.80	2617.65	3606.56
2202.00	1644.90	2621.31	3384.62
2213.00	1651.40	2624.32	3548.39
2224.00	1657.60	2627.78	3460.32
2235.00	1663.90	2630.93	3333.33
2246.00	1670.50	2633.70	3333.33
2257.00	1677.10	2636.46	3333.33
2268.00	1683.70	2639.19	3303.03
2279.00	1690.30	2641.78	3384.62
2290.00	1696.80	2644.63	3606.56
2301.00	1702.90	2648.07	3728.81
2312.00	1708.80	2651.80	3573.77
2323.00	1714.90	2655.08	3793.10
2334.00	1720.70	2658.92	3758.62

2345.00	1726.50	2662.61	3928.57
2356.00	1732.10	2666.71	3694.92
2367.00	1738.00	2670.20	3666.67
2378.00	1744.00	2673.62	3516.13
2389.00	1750.20	2676.61	3666.67
2400.00	1756.20	2679.99	3516.13
2411.00	1762.40	2682.93	3406.25
2422.00	1768.80	2685.55	3492.06
2433.00	1775.10	2688.41	3758.62
2444.00	1780.90	2691.90	3633.33
2455.00	1786.90	2695.06	3758.62
2466.00	1792.70	2698.50	3928.57
2477.00	1798.30	2702.33	3963.64
2488.00	1803.80	2706.18	3892.86
2499.00	1809.40	2709.85	3758.62
2510.00	1815.20	2713.20	3633.33
2521.00	1821.20	2716.23	3857.14
2532.00	1826.80	2719.73	3824.56
2543.00	1832.50	2723.17	3573.77
2554.00	1838.60	2725.99	3824.56
2565.00	1844.30	2729.38	4000.00
2576.00	1849.70	2733.09	3927.27
2587.00	1855.20	2736.63	3963.64

2598.00	1860.70	2740.26	3600.00
2609.00	1866.70	2743.02	3724.14
2620.00	1872.50	2746.06	3857.14
2631.00	1878.10	2749.37	3724.14
2642.00	1883.90	2752.38	3754.39
2653.00	1889.60	2755.40	4075.47
2664.00	1894.90	2759.09	4037.74
2675.00	1900.20	2762.66	4000.00
2686.00	1905.60	2766.16	4115.38
2697.00	1910.80	2769.83	4037.74
2708.00	1916.10	2773.34	4115.38
2719.00	1921.30	2776.97	3785.71
2730.00	1926.90	2779.91	3821.43
2741.00	1932.50	2782.92	3754.39
2752.00	1938.20	2785.78	3854.55
2763.00	1943.70	2788.80	3593.22
2774.00	1949.60	2791.24	3689.66
2785.00	1955.40	2793.90	3719.30
2796.00	1961.10	2796.59	3785.71
2807.00	1966.70	2799.41	3818.18
2818.00	1972.20	2802.25	3925.93
2829.00	1977.60	2805.32	3925.93
2840.00	1983.00	2808.37	4117.65

2851.00	1988.10	2811.73	4076.92
2862.00	1993.30	2815.03	4117.65
2873.00	1998.40	2818.35	